IN SITU EXPERIMENTATION AND NUMERICAL MODEL VALIDATION OF THERMAL FLOW IN SHALLOW CRYSTALLINE ROCK

OTANIEMI CASE

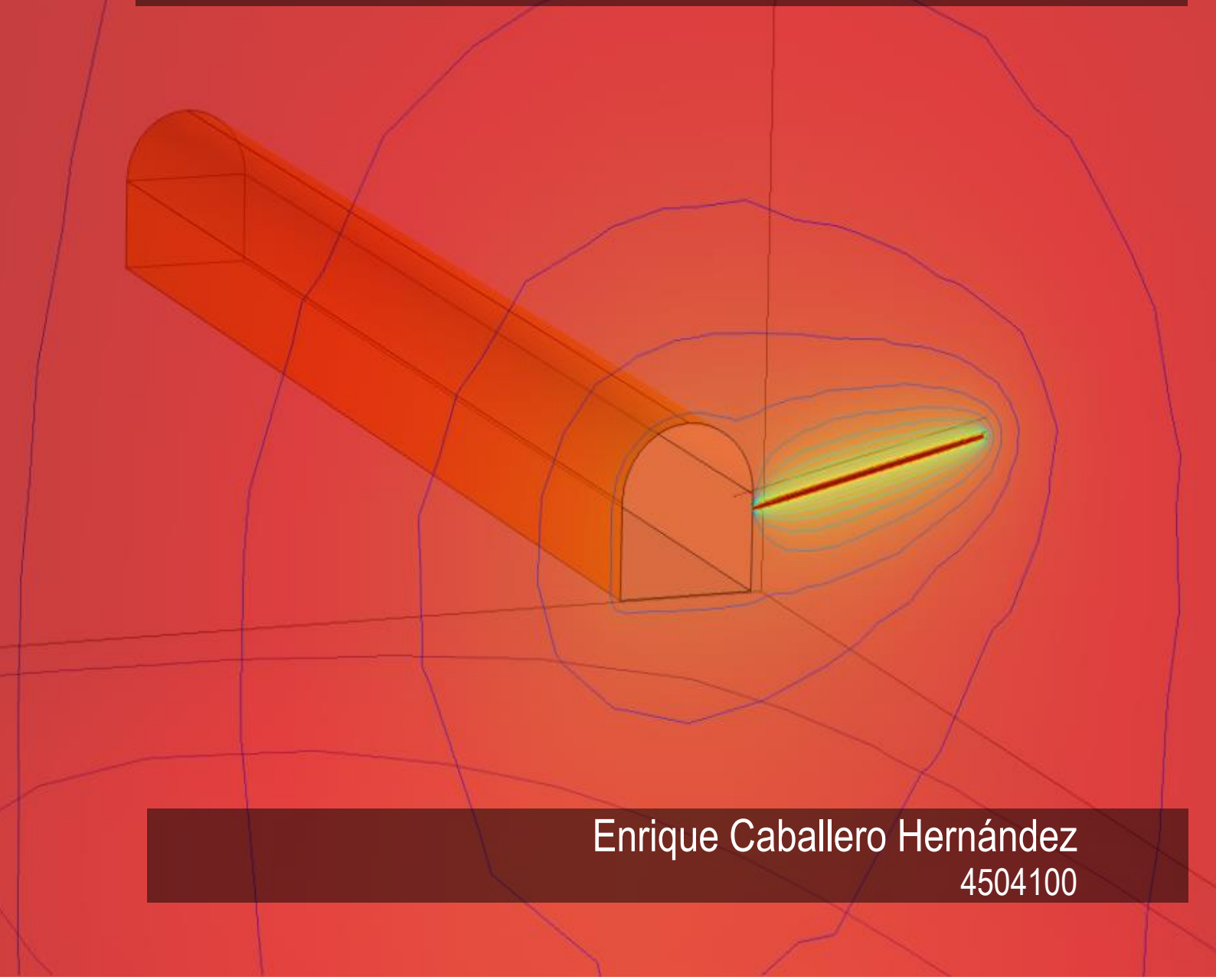

Enrique Caballero Hernández
4504100

TU Delft

Aalto University
School of Engineering

In situ experimentation and numerical model validation of thermal flow in shallow crystalline rock, Otaniemi case.

By

Enrique Caballero Hernández

in partial fulfilment of the requirements for the degree of

Master of Science

in Applied Earth Sciences

at the Delft University of Technology
Faculty of Civil Engineering and Geosciences,
to be defended publicly on Tuesday November 14th, 2017.

Date:	Tuesday, November 14th 2017	
Student number:	4504100	
Graduation committee:	Profr. dr. Ir. T.J. Heimovaara	TU Delft
	Dr. Anne-Catherine Dieudonné	TU Delft
	Dr. Mikael Rinne	Aalto University
	Dr. Ferenc Mádai	Miskolc University
	Dr. Gabriela Paszkowska	Wrocław University of Sicence & Technology

Author Enrique Caballero Hernández

Title of thesis *In situ* experimentation and numerical model validation of thermal flow in shallow crystalline rock, Otaniemi case.

Degree program European Mining, Mineral and Environmental Program (EMMEP)

Major/minor European Geotechnical and Environmental Course **Code** AES-EGEC

Thesis supervisor(s) Prof. dr. Timo Heimovaara (TU Delft), Prof. dr. Mikael Rinne (Aalto University)

Thesis co-supervisor(s) Dr. Anikó Tóth (Miskolci Egyetem), Prof. dr. Herbert Wirth (Politechnika Wrocławska)

Thesis advisor(s) Ph.D. Topias Siren, M.Sc. Mateusz Janiszewski (Aalto University)

Date 14.11.2017 **Number of pages** 103+33 **Language** English

Abstract

Nowadays more attention to environmental-friendly sources of energy has been given, aiming to slow down and counteract the damage to the ecosystem product of the abuse of fossil fuels. Different technologies on energy production, solar, wind, tidal, geothermic, etc., have been researched with the additional challenge of how to store it.
From the different types of energy, heat represents a basic need in countries where the climate conditions lead to long and cold periods, namely countries at high latitudes where a big part of the produced energy is destined to household and district heating.
The Academy of Finland implemented the New Solar Community Concept project to research the development and application of alternative technologies for production and storage of energy. The use of the local geological domains has been considered as a possible solution for seasonal and long-term energy storage, specifically heat. Aalto University participates in Tackling the challenges of a Solar-Community Concept in High Latitudes by researching the seasonal storage of thermal energy in the ground simulating and assessing thermal flow for different borehole heat exchangers arrays.
To do this, numerical models have been implemented, special attention to the Weak Form Equations (WFE) and the Heat Transfer in Pipes (HTiP) models. These models are evaluated using the COSMOL® Multiphysics software, each of them with advantages and disadvantages over the other.
An *in situ* experiment has been performed in Aalto's research tunnel to validate the results of the numerical models. The aim of the experiment was to assess the performance of the models based on the result comparison between the simulated and the observed data under controlled conditions.
The experiment consisted of a single U-pipe borehole heat exchanger operating under seasonal conditions. Two phases were defined, heating and cooling. In the first phase, a constant heat flux is provided to the rock by circulating a heated carrier fluid in the BHE. In the second phase, the circulation is stopped allowing the rock to cool down under normal conditions. The heat field in the rock was tracked with a monitoring borehole one meter away from the heat source. Several digital temperature sensors were installed at the monitoring point in customized equipment referred in this work as Thermal Multisensor Probes for this purpose.
The comparison made between model and observed results returned an acceptable accuracy of the predicted models values for the heat flow in the rock mass. Additionally, it was identified the WFE model can be improved by calibrating the borehole thermal resistance parameter in the equations, parameter that must come from experimental data. Finally, it was seen that the few discontinuities present across the boreholes had a low impact on the flow of heat through the rock for this experiment.
Currently, the tuning of the numerical models is being performed at Aalto University by increasing the weight of different parameters in the models matching the results of the experimentation process.

Keywords *Borehole Heat Exchanger (BHE), model validation, numerical modelling, in situ experiment, heat flow, seasonal storage,*

Foreword

I would like to thank in first instance to Aalto University, especially to the *Computational Modelling of Rock and Soil Structures – Rock and Mining Engineering* group for their trust and support in the development of this project.

To my supervisor, Mikael Rinne, who was supportive in every step given during the project. To my instructors, Topias Siren and Mateusz Janiszewski for their guidance through the application of the models and the development of the experiment. To Lauri Uotinen for helping with ideas and guidance for the development of the BoreScan Camera (AKA. Burrito) used for the video survey of the boreholes was done. To Henri Munukka for building the thermal sensors probes and set up the Pi boards to operate them, necessary equipment for the tracking and evaluation of this project. Finally, to Tuomo Hänninen, whose experience and ability in the hand-held drilling allowed to set in motion the practical part of this work after the faced downtimes with the bigger equipment.

Special thanks to Otto Hedström, Rock Mechanics Laboratory Manager, who was always willing to aid in every topic related to the preparations for the experiment, from drilling to the installation of the piping system for the BHE.

I would also like to thank the *gezelligs*, Suus Oudwater and Roel van Toorenenburg for their constant cheering and support, but especially for making the time in the office very entertaining with very *gezellig* coffee breaks, and even more for being the best grouting crew I could ask for.

To my EGEC group and honorary members; Timi, Paula, Balász and Wojciech, for making me feel surrounded by friends these past 2 years being so far away from home.

To my old friend Omar Velazquez, for advising and reminding me constantly the need of setting priorities and help me during my arrival to this new country.

Last, but not least, to my parents who have always believed in me and who have been supportive in every single step I have taken in my life leading me to the place I find myself now. They have taught me that hard work and a positive attitude open the doors of a bright future in every single aspect of life.

The funding and support of the Academy of Finland for the realization of the entire Solar Community Concept is acknowledged.

Enrique Caballero Hernández

Table of Contents

Notations

Greek letters

α	Thermal diffusivity	m^2/s
β	Thermal expansion coefficient	-
λ	Thermal conductivity	W/(m·K)
λ_{eff}	Effective thermal conductivity	W/(m·K)
λ_g	Thermal conductivity (grout)	W/(m·K)
λ_p	Thermal conductivity (pipe)	W/(m·K)
λ_s	Thermal conductivity (soil/ground/rock)	W/(m·K)
μ	Dynamic viscosity	Ns/m^2
ν	Kinematic viscosity	m^2/s
π	Pi number	-
ρ	Mass density	kg/m^3
A	cross-sectional area	m^2
C_p	Heat capacity	J/(kg·K)
d	Borehole diameter	m
D_h	Hydraulic diameter	m
D_i	Outer pipe diameter	m
D_o	Inner pipe diameter	m
L	Characteristic length	m
Nu	Nusslet Number	-
P	Power Heating rate	W/m
Pe	Peclet Number	-
Pr	Prandtl number	-
Q	Heat flow	W
$q(t)$	Thermal flux	W/m
R_b	Borehole thermal resistance	m·K/W
r_b	Borehole radius	M
Re	Reynolds number	-
R_g	Thermal resistance (grout)	m·K/W
R_p	Thermal resistance (pipe)	m·K/W
R_s	Thermal resistance (soil/ground/rock)	m·K/W
S_{VC}	Volumetric heat capacity	$MJ/(m^3·K)$
t	Time	s
T_f	Fluid temperature	°C
T_{s0}	Undisturbed ground temperature	°C
T_s	Ground temperature	°C
T_i	Fluid temperature (inflow)	°C
T_o	Fluid temperature (outflow)	°C
u	Fluid mean velocity	m/s

Abbreviations

1D	One-dimensional
2D	Two-dimensional
3D	Three-dimensional
ACRE	Aalto University Real State
BH	Borehole
BHE	Borehole Heat Exchanger
BTES	Borehole Thermal Energy Storage
EXBH	Experiment Borehole
GTK	Finnish Geological Service
GW	Groundwater
HTiP	Heat Transfer in Pipes
MOBH	Monitoring Borehole
MTD	Mean temperature displacement
P3	Probe 3
P4	Probe 4
S1-12	Sensor 1 – 12
SCC	Solar Community Concept
TCS	Thermal Conductivity Scan
TRT	Thermal Response Test
UTES	Underground Thermal Energy Storage
WFE	Weak Form Equations

List of Tables

List of Figures

1 Introduction

With the constant influx of energy coming from the sun, especially during the summer months, the earth's surface and subsurface are warmed on a regular basis over the years. This energy is in great part reflected to space; however, a considerable amount of it is trapped inside the atmosphere, with part of it being stored in the earth subsurface. Based on this fact, the earth's shallow subsurface can be regarded as an immense heat storage, with the mineralogy, porosity, and water content of the rocks playing an important role to determine the thermal conductivity and the storage capacity of the ground.

Most of soils and rocks on the surface and subsurface in the earth are silicate-base, presenting a modest thermal conductivity such to avoid the immediate dissipation of heat, but at the same time, permitting its retrieval through uncomplicated methods. From the rock forming minerals, quartz has the highest thermal conductivity, followed by water and finally air filling the pores. Low porosity and dense interlocking crystal structure with high quartz content rocks, such as granite, would then be the most suitable combo to conduct and storage heat. This represents a great potential to store heat at shallow depths for its posterior use considering its availability.

1.1 Motivation

The constantly raising prices of the fossil fuels, as well as the quick progressive increment in the global temperature, has been a topic of concern for many national agencies and scientists around the world since the middle of the 1980's. This concern has led to an increasing pressure to reduce the fraction of energy that comes from fossil fuels and increase the participation of the green energies on the global scale, situation that has led to the research and development of renewable technologies to produce and storage energy from sources like the sun, wind, the earth core, and the ocean.

Currently, the main issue with the alternative energies is the capacity to storage of energy for its posterior use when the demand peaks in comparison with the average production, which can vary from depending on the time of the day and the season of the year. Following this late statement and referring to heat production, the advantage of the solar

energy is higher when the sunlight availability is the greatest and the solar radiation the strongest, namely, during the summer. Is during this season that most of the heat energy from solar technologies can be produced; however, is also when it is needed the less as the weather conditions are not as rough as in winter when the sunlight is less available. This situation becomes of greater importance to those countries where the availability of sunlight is highly imbalanced through the year, i.e. high latitude countries.

In the Nordic countries, this is a topic of research since the winters are longer than in more tropical regions and with much fewer hours of sunlight, what makes the conditions extremely cold, which can be translated into a higher demand of energy for household and district heating. High latitude countries such as Denmark and Sweden have several Solar-district-heating (SDH) plants that provide heating to entire communities, counting 76 and 21, respectively. Contrastingly, in Finland, the number of projects is limited to a single digit (2) with quite out of date cases, Kerava in 1985 and Ekoviikki in 2000, according to the European SDH platform database (2016) and the European Urban Knowledge Network (2010).

Different factors; natural, industrial and sociological, have influence in why the development of such systems in Finland have been in delay. Tougher weather conditions than in neighboring countries, conservative ideology and practices in the construction industry, an undeveloped energy business concept, and the lack of concern from the population about the source of the energy, can be considered inside such factors.

As part of the efforts to develop these technologies, their performance, application, and reliability, the Academy of Finland has set in motion the *New Energy Solar Community Concept (SCC)* project aiming to research and develop the required technologies for production and storage of energy in the Finnish conditions. Part of this project is the feasibility research of long-term storage solutions in different geological domains found in Finnish territory.

The seasonal temperature variation at the ground surface is reduced to a nearly constant temperature of around 14°C at 10 – 15 m below the surface. Under this depth, the temperature is known to increase with an average gradient of 3°C per 100 m depth (effect of the Earth's core heat, i.e. geothermal gradient). The continuous thermal interaction between the air and the earth makes the first 100 m sustainable and, therefore, suitable

for supply and storage of thermal energy, though at a relatively low temperature. Two common energy systems based on this principle are the ground source heat pumps, and the Underground Thermal Energy Storage (UTES) (R. Al-Khoury 2012).

Presently, Aalto University has created numerical models to describe the behavior of UTES through the back-calculation of data from the Kerava Solar Village project, calibrating the numerical models to be used in an optimization by quantifying the thermal properties of the underlying and surrounding granite and soil as presented in Oosterbaan (2016) and Oosterbaan, *et* al. (2017).

Two fully functional 3D computational models have been developed in *COMSOL® Multiphysics* by applying the finite element method (FEM) to analyze data obtained from a previous Master Thesis. The models have been used to simulate the Borehole Thermal Energy Storage (BTES) concept in hard rock under different scenarios by alternating parameters, like borehole length, spacing between boreholes and amount of heating elements.

The present work is a step forward in the project titled "Tackling the challenges of a Solar-Community Concept in High Latitudes"; a continuation to the previous work done by Oosterban in 2016 and the work the department of Rock Mechanics of Aalto University has developed in the last year in the field of seasonal heat storage at high latitudes.

The purpose of this thesis is to assess and validate the developed numerical models, confronting the results of the simulations against the data obtained from observation and measurement under a controlled environment.

To achieve this purpose, an *in situ* experiment was performed in the bedrock under Otaniemi campus. The experiment consists on a Borehole Heat Exchanger (BHE) installed in shallow rock mass to. The variations in the results of the simulated and observed data is to be used for the upgrade and update of the numerical models. Different scenarios involving arrays of more than one BHE are performed constantly, therefore the importance of validating the actual models with observed data.

1.2 Research questions

The questions intended to be answered by the experiment and this work are:

- How precise are the computational models in comparison to the results of the experiment?
- Which model describes better the performance of the experiment?
- Which are the *in situ* factor not taken into consideration by the numerical models?
- Which changes are necessary to implement for a more realistic model results?
- How can they be implemented?
- Is it possible to determine the *in situ* rock thermal conductivity and capacity?

This thesis introduces first the basic concepts in heat transfer, the parameters and the mechanisms involved, followed by the heat transfer process in the borehole heat exchangers. The theoretical part continues with the description of the thermal response test, necessary test to assess the local thermal parameters of the ground and the installed BHE configuration.

The description of the experiment; stages and steps to be taken, location, materials and components installed, and description of the numerical models used for simulation are presented after the theoretical background.

Under the results section, the results of the different scenarios are compared against the measured data of the *in situ* experiment. For this purpose, the local ground properties and parameters are fed into the model. The properties that could not be tested are taken from the literature.

A discussion about the obtained results from the modelling, the experiment, and the comparison between both is followed by the conclusions about the performance of the models, compared against the experiment's data. Some recommendations about how to improve the experimental part and how to aim for better results from the models finalize the thesis report.

At the end of the document, a set of appendixes are attached with the data obtained from the monitoring, and laboratory tests, as well as the layout of the experiment's installation and the data of the equipment used.

2 Theoretical Background

2.1 Heat transfer

Al-Khoury (2012) expresses the term *heat transfer* as the thermodynamic process dealing with the rate of thermal energy in motion between the system source and the media that surrounds it and the transfer mechanisms involved.

To determine the heat transfer, the temperature and the heat flow are measured and computed. *Temperature* refers to the amount of thermal energy in the system, whilst *heat flow* defines the movement of thermal energy as result of the thermal gradient.

The energy gained or lost by a body in a continuous media or between bodies in thermal contact and subjected to certain boundaries, is constrained by different parameters describing the material properties. Additionally, the heat transfer process is affected by the geometrical configuration and physical properties of the involved elements in the system.

2.1.1 Parameters

Special attention is given to the *thermal conductivity*, the *specific heat or heat capacity*, the *mass density*, and the *thermal diffusivity*, among different material parameters, to explain and measure heat transfer.

Thermal conductivity $\boldsymbol{\lambda}$ [W/m·K] is the ability of a material to transmit certain quantity of heat q, through a unit of thickness L, in the normal direction of a unitary surface A, under the effects of temperature gradient ΔT.

$$\lambda = \frac{qL}{A\Delta T} \tag{1}$$

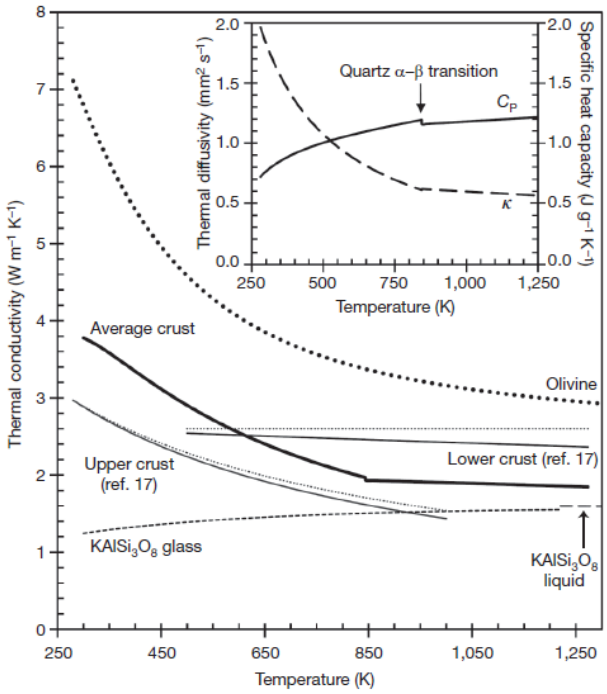

Figure 1. Example of calculated thermal conductivity as a function of temperature for average crust. Inset, contrasting temperature dependence of thermal diffusivity and specific heat capacity, calculated for average crust. After Whittington et al. (2009).

Al-Khoury (2012) states, for both, solids and liquids, thermal conductivity is thermal dependent, increasing as the temperature does in case of solids (Figure 1), and vice versa when referring to liquids, with exception of water that presents a similar behavior to solids until 130°C~150°C (Figure 2).

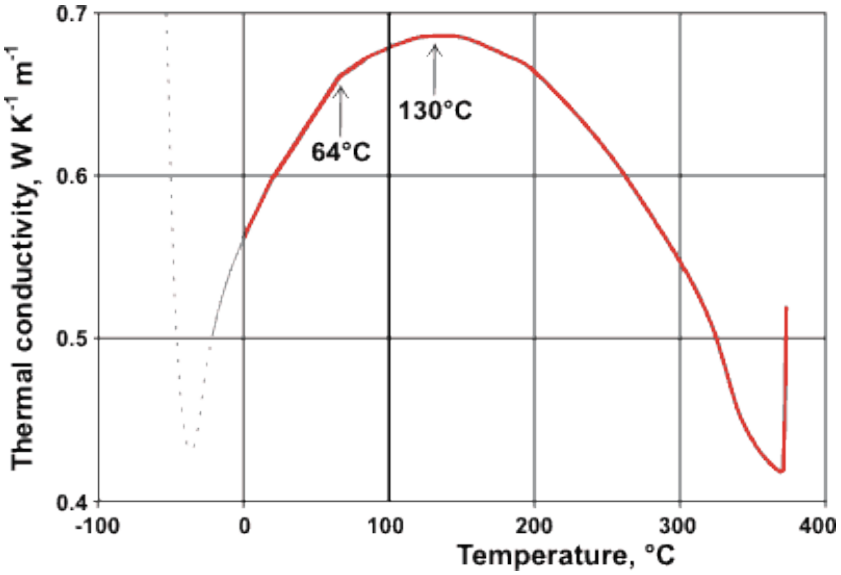

Figure 2. Thermal conductivity along the saturation line (liquid-vapor equilibrium line). Note: pressure increases with temperature. After Chaplin (2006).

Thermal capacity $\boldsymbol{C_p}$ [J/kg·K] is the amount of heat required to raise the temperature of a substance's unit of mass by one-degree. It can be defined in terms of constant volume (C_V) or pressure (C_p). If analyzed based on the volume of rock instead of mass, the term is usually labeled *volumetric heat capacity* S_{VC} *(J/ m*^{3}*·K).*

In the case of an incompressible material, the terms are equal between each other $C(T) = C_V(T) = C_p(T)$; being $C(T)$ a weak form function of the temperature and for a wide interval can be approximated by the linear Eq. (2) (Eppelbaum *et* al. (2014)).

$$c(T) = c(T_i) + \beta(T - T_i) \tag{2}$$

with T_i being initial temperature and β the thermal expansion coefficient.

When the term is used to indicate the capacity of a body to store certain amount of heat for every degree of temperature it is referred as *Specific heat*. In shallow geothermal applications, the specific heat can be considered constant as they normally operate under a small temperature variation range.

Thermal diffusivity $\boldsymbol{\alpha}$ [m^2/s] determines how fast a solid's temperature field changes with time under transient conditions expressed as the ratio of the thermal conductivity to the volumetric heat capacity.

$$\alpha = \frac{\lambda}{\rho C_p} = \frac{\lambda}{S_{VC}} \tag{3}$$

Thermal properties of rocks and soils can be found in different literature sources as result of several investigations all around the world (e.g, Carmichael (1982), Rohsenow *et* al. (1998), The Engineering Toolbox (2017), etc.); nevertheless, the *in situ* determination is advisable depending on the importance and size of the project.

The geometrical array of the system has also influence in the heat transferred. This influence is represented by the fluid and thermal flow numbers, the *Nusselt number* Nu, the *Peclet number* Pe, the *Reynolds number* Re, and the *Prandtl number* Pr, as well as the fluid flow rate $q(t)$.

The *Reynolds Number* $\boldsymbol{Re}$ is a dimensionless quantity utilized in fluid mechanics to classify the flow patterns of a fluid. Depending on the value of Re, the flow is classified

as laminar, transient, or turbulent, explaining the behavior of the flow lines in the transport media. The flow regime has influence in the rate of heat transferred from a fluid in movement to the surrounding material, being the laminar and turbulent cases the ones with the lowest heat transfer. The flow regimes are classified as

$Re < 2300$	Laminar
$2300 < Re < 4000$	Transient
$Re > 4000$	Turbulent

The flow regime can be calculated with Eq. (4).

$$Re = \frac{inertial\ force}{viscous\ force} = \frac{\frac{\rho u^2}{L}}{\frac{\mu u}{L^2}} = \frac{\rho u L}{\mu} = \frac{QL}{\nu A} \tag{4}$$

where u is the fluid's mean velocity [m/s], μ and ν are the dynamic [Ns/m^2] and kinematic [m^2/s] viscosity, respectively; ρ is the fluid's density [kg/m^3], Q is the volumetric flow rate [m^3/s]; L is the characteristic length [m], and A is the cross-sectional area of the pipe [m^2]. In case of tubes, L is the pipe diameter, with D_h as the hydraulic diameter.

$$Re = \frac{\rho u D_h}{\mu} \tag{5}$$

Banks (2012) recommends for geothermal applications, a transient flow mode is desirable as reasonably efficient heat transfer is achieved in the range $2500 < Re \leq 3000$.

The *Prandtl number* Pr is defined as the ratio between the material's kinematic viscosity ν and thermal diffusivity α, expressed as

$$Pr = \frac{\nu}{\alpha} = \frac{C_p \mu}{\lambda} \tag{6}$$

The *Peclet number* Pe characterizes the heat flow mode defined as the ratio of the advection rate to the diffusion rate, i.e. the product of the Reynolds and Prandtl numbers.

$$Pe = \frac{uL}{\alpha} = Re \cdot Pr \tag{7}$$

where u is the velocity of the fluid and L is the characteristic length of the element.

Finally, the Nusselt number Nu is defined as the ratio of convective to conductive heat transferred across the boundary,

$$Nu = \frac{hL}{\lambda} \tag{8}$$

where h is the convective heat transfer coefficient and λ_f is the fluid's thermal conductivity.

When Nu is closer to the unity, the laminar flow is dominant. On the other hand, a Nu ranging between 100 and 1000 is characteristic of turbulent flow. The characteristic length is the thickness of the boundary, in case of BHE pipes, is the outer diameter.

$$Nu = \frac{hD_h}{\lambda_f} \tag{9}$$

2.1.2 Transport mechanisms

Three mechanisms describe heat transfer phenomena, *conduction, convection, and radiation*. Only conduction and convection are used to assess the heat flow process in geothermal systems as radiation does not take place in the underground continues medium.

Conduction (or heat diffusion). When in thermal contact, and under a difference in temperatures, energy flows from a higher temperature zone or object to a lower one until thermal equilibrium is reached. The heat transfer rate per unit area normal to the direction of heat flow (or heat flux) is described by the *Fourier's law* of thermal conductivity.

$$q''_x = -\lambda_x \frac{dT}{dx} \tag{10}$$

Eq. (10) is a one-dimensional equation, where dT/dx is the temperature gradient in the *x*-axis, and λ_x is the thermal conductivity of the material in the *x*-direction. The minus sign determines the direction of the heat flow, from the higher to the lower temperature zone.

When multiplying Eq. (10) by constant cross-sectional area A, the expression becomes,

$$q_x = -\lambda_x A \frac{dT}{dx} \tag{11.a}$$

$$Q = -\lambda A \frac{dT}{dz} \tag{11.b}$$

Eq. (11.a) is the representation of Fourier's law by Banks (2012) referring to the geothermal gradient, where Q is the heat flow, and z the depth coordinate.

With $q_x = q_x'' A$, Fourier's law in three-dimensions is written as

$$\boldsymbol{q}'' = -\lambda \nabla T \tag{12}$$

where ∇ is the gradient operator and λ is a tensor representing three-dimensional thermal conductivity of the material.

Convection is an important heat transfer mode identified as the heat transfer of a solid body in contact with a moving fluid. Related to flow rate, is the result of the bulk motion of a fluid transporting heat from one point to another in the flow direction.

In this mechanism, diffusion and advection take place simultaneously and can be describe as the the heat flow rate per unit area normal to the heat flow. The simultaneity of the processes is represented in Eq. (13). The first term of the equation represents the heat diffusion and the second the heat advection, with u_x as the fluid velocity along the *x*-axis.

$$q_x'' = -\lambda_x \frac{dT}{dx} + \rho C_p u_x T \tag{13}$$

The full solution of the differential equations for both mechanisms for heat transfer process can be found under Al-Khoury (2012).

2.2 Heat transfer in BHE

When referring to geothermal projects, usually the borehole's depth is more than 250 m, using the Earth's thermal gradient to collect heat. Shallow applications, on the contrary, are drilled before this mark, where the increment in the ground surface temperature is product of the solar radiation, and controlled by the air temperature in contact with it.

During summer, the earth's surface is heated up due to intense solar radiation and elevated air temperatures. The heat is propagated few meters down into the subsurface, with a temperature profile in funnel shape. The temperature in the surface will be higher or lower than in the subsurface depending on the time of the year, and stabilizing exponentially with depth, independently of the season (Figure 3). Temperature in the subsurface becomes remarkably stable after 10 m of depth according to Banks (2012), and 10-15 m for higher latitudes according to Kukkonen (2016), depth at which the air temperature has almost no more influence in the ground temperature.

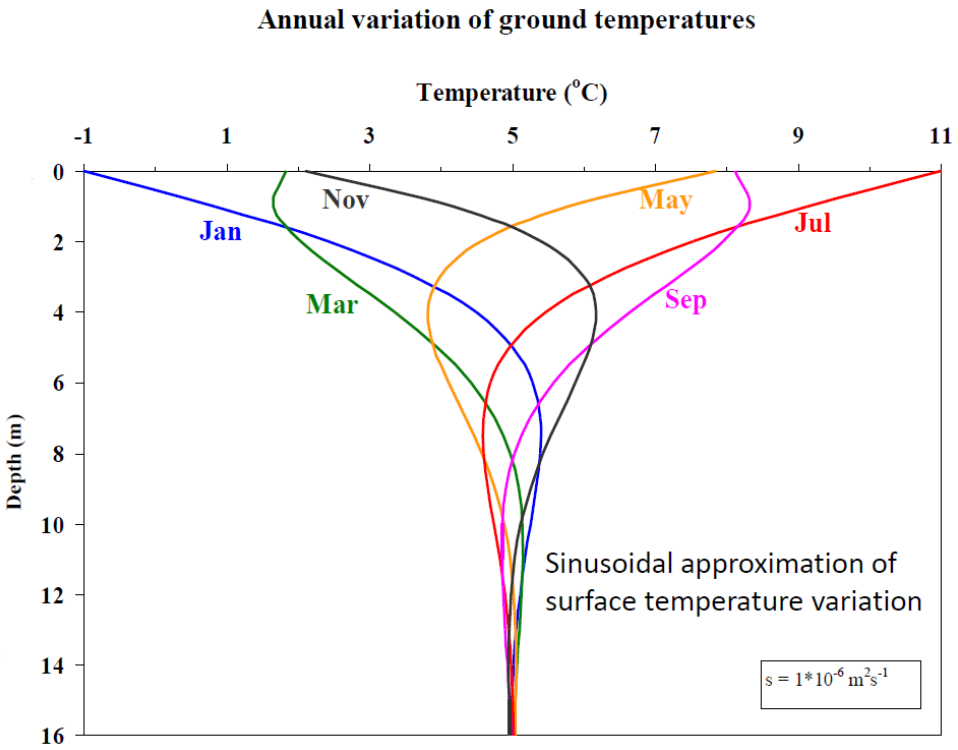

Figure 3. Annual variation of ground temperatures in Finland after Kukkonen (2016).

The variation on the ground surface temperature is the basic concept for the thermal seasonal storage, collecting enough thermal energy from the sun during the summer, its storage in the subsurface, and retrieval during the cold months. To transfer thermal energy in and out of the subsurface, a borehole heat exchanger is required.

A borehole heat exchanger consists on an array of pipes through which a fluid or refrigerant, the carrier fluid, is circulated to transfer thermal energy. The pipes are placed inside a borehole usually driven vertically into the ground; or horizontally, habitually in shallow trenches in soil, but deep enough to avoid the freezing of the carrier fluid during winter.

For shallow BHE is possible to use two types of system, open-loop and closed-loop. In an open-loop system, the heat transfer occurs most of the times in an aquifer where the heat can migrate by being injected or subtracted via groundwater (GW). This kind of systems can represent an environmental threat as the groundwater is taken out from the formation, put through heat pumps, and eventually returned into the ground, carrying possible pollutants that might been found into the pipelines, besides the possible biochemical reactions that might occur due to contact with oxygen.

On the other hand, closed-loop systems consist on an array of pipes through which a carrier fluid is circulated transferring heat from the surface into the ground or vice versa. In this system, the fluid never holds physical contact with the host formation, eliminating part of the risks the open-loop systems represent; however, the amount of heat that is effectively transferred is less, as more elements are present between the heat source and the heat reservoir, increasing the resistance to thermal flow.

Closed loops are commonly made of plastic pipes (typically Polyethylene) placed in a borehole and embedded in a filling material, either groundwater or some grout (e.g. bentonite, cement), which acts as thermal link between the pipe elements and the ground. The selection of the filling material depends mostly on the country of application and its environmental regulations.

While groundwater-filled boreholes are cheaper in construction, the borehole is kept open which represents an environmental threat. Nevertheless, if grout material reacts with the groundwater or mineral components in the ground, it can also become a threat.

In case of groundwater-filled boreholes, heat transport due to convection inside the borehole takes place and must be taken into consideration while designing the BHE, as a higher heat exchange and lower thermal resistance may be found (Oberdorfer (2014)). In the case of grouted boreholes, conduction is the accounted mechanism. Convection is not considered to take place inside the borehole, but only inside the pipes where the fluid is in movement (Al-Khoury (2012)).

Inside the BHE, heat transfer involves conductive and convective processes taking place in a multiple component medium. The most basic and common configuration of a BHE consists on a single U-shape pipe creating a closed loop with one inlet and one outlet for the fluid transporting heat.

Four elements must be considered in a BHE array,

- the refrigerant or carrier fluid,
- the pipe, in and out,
- the filling material or grout and,
- the host media.

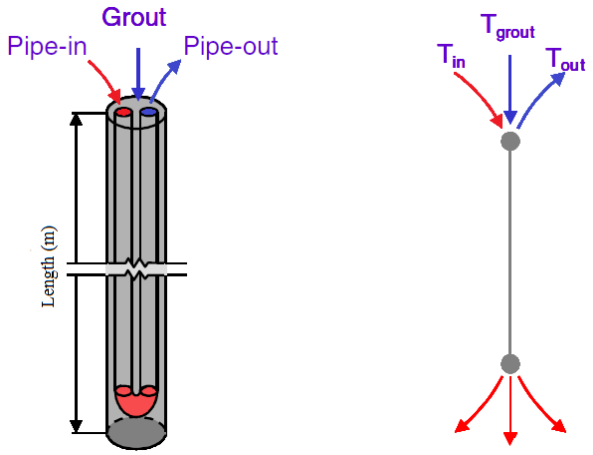

Figure 4. Schematic and finite element representation of a vertical single U-pipe BHE. Modified from Al-Khoury et al. (2005).

Heat transfer between the carrier fluid in the pipes and the ground occurs through the filling material inside the borehole. This environment represents a complicated interaction as it is composed by different elements with different thermal properties, altering the equation to determine the total heat transferred in the system.

The amount of heat transferred into the ground then, will depend mainly in the resistance opposed by the elements in between, namely the resistances provided by the pipe R_p, the grout R_g, the soil/ground R_s, and the interaction between them.

Figure 5 illustrates the elements resistance interaction analogically to the Fourier's law and the Ohm's law.

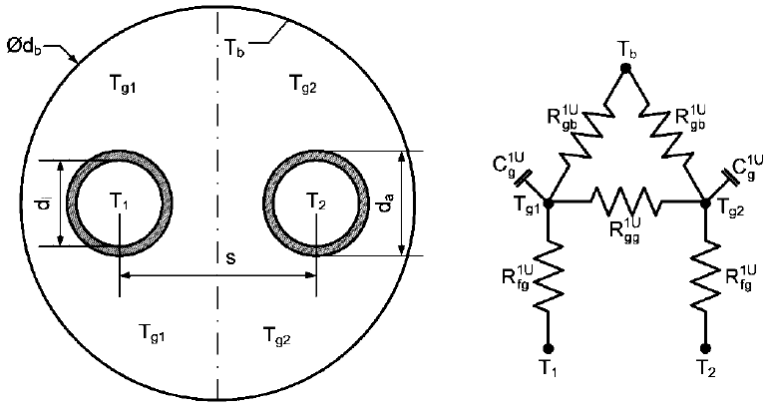

Figure 5. Thermal resistance and capacity model for single U-tube BHE. T_i fluid temperatures, T_{gi} grout temperatures, T_b temperature of the borehole wall, C_g thermal capacities, R_{ii} thermal resistances between elements, after Bauer et al. (2011).

Here, the thermal energy flows from the source to the ground through the resistant elements which in the end will cut down some part of the heat transferred, i.e. the thermal energy decreases from the heat source (carrier fluid) to the repository (ground/soil/rock) by going through the diverse resistive elements (pipes, grout, ground).

Consequently, the overall borehole thermal resistance R_b is the sum of the system's involved elements resistances. The temperature between the heat source and the final storage destination decreases accordingly to the number of elements in between and the resistance these oppose to the heat flow as schematized in Figure 6.

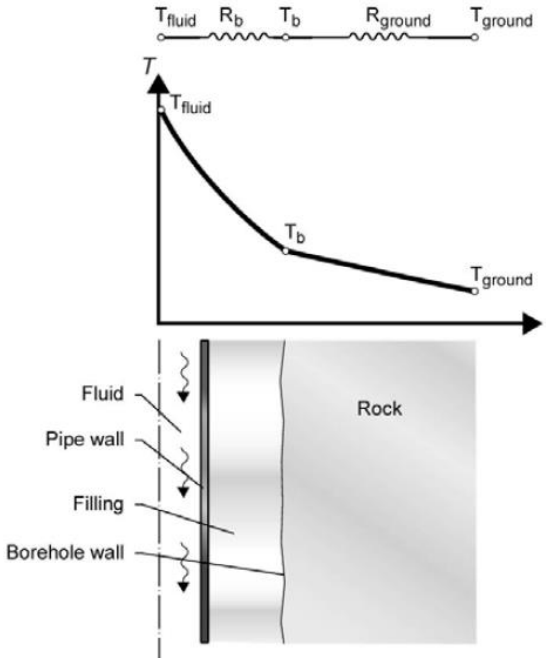

Figure 6. Interaction of elements temperatures and resistances in the borehole thermal resistance after Gehlin (2002).

Considering a single U-pipe array, the most influential parameters per element are

- Pipes
    - Diameter, thickness, material (thermal conductivity),
    - Number of pipes, position of the pipes (spacing of shanks)
- Filling material
    - Thermal conductivity

The values in borehole thermal resistance are entirely dependent on the configuration of the borehole and the surrounding geology, therefore is complicated to establish idealistic values for it. Nevertheless, previous TRTs performed in Germany by Sanner *et* al. (2000)

have shown the difference grout makes when referring to borehole thermal resistance. Boreholes with thermal enhanced grouts present a lower R_b value (0.6-0.8 m·K/W) compared to those filled with normal grout. With basis on these results, it can be said that a *good* thermal resistance value would be R_b<0.11 m·K/W, while a value of R_b>0.14 m·K/W is considered as *poor*.

Table 1. Borehole thermal resistance of single U-pipes, after Hellström (2011).

Site	**Filling material**	**Borehole R_b [m·K/W]**
USA, several	bentonite	0.13 - 0.15
USA, several	thermal grout	0.09 - 0.10
Luleå	water, heating	0.05 - 0.06
Norway	water, heating	0.05 - 0.07
Lund (laboratory)	water, heating	0.05 - 0.07
Lund (laboratory)	(copper),water, heating	0.03 - 0.05
Studsvik	Ice	0.09

2.2.1 Pipes

Pipes are the first domain in contact with the heat source, representing the first resistive barrier and playing an important role on the amount of heat transferred into the ground.

The thermal resistance opposed by the pipe will be a function of its material, which also determines the roughness in the inner surface of the walls, and its thickness. The wall thickness influences the thermal conductivity of the pipe due to the length component *L* of Eq.(1).

In addition, the diameter of the pipes and wall thickness determine the hydraulic diameter component D_h, dictating the cross-sectional area of the pipe and the possible flow rate inside the pipe, hence the flow mode (R_e).

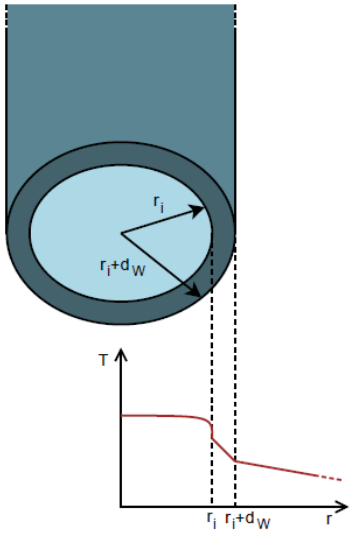

Figure 7. Temperature profile (qualitative) of a pipe fluid in heat exchange with the subsurface ambience (heat injection). After Oberdorfer (2014).

Table 2. Properties of plastic pipes used for ground loops. Hellström (2011).

Type	Material	Outer diameter (mm)	Wall thickness (mm)	Thermal cond. (W/(m,K))	Thermal resistance (K/(W/m))
PE DN25 PN8	Polyethylene	25,0	2,0	0,42	0,066
PE DN32 PN8	Polyethylene	32,0	2,0	0,42	0,051
PE DN40 PN8	Polyethylene	40,0	2,3	0,42	0,046
PE DN50 PN8	Polyethylene	50,0	2,9	0,42	0,047
PE DN20 PN12	Polyethylene	20,0	2,0	0,42	0,085
PE DN25 PN12	Polyethylene	25,0	2,3	0,42	0,077
PE DN32 PN12	Polyethylene	32,0	3,0	0,42	0,079
PE DN40 PN12	Polyethylene	40,0	3,7	0,42	0,078
PE DN50 PN12	Polyethylene	50,0	4,6	0,42	0,077
SDR-11 3/4"	Polyethylene	26,7	2,5	0,42	0,079
SDR-11 1"	Polyethylene	33,4	3,0	0,42	0,075
SDR-11 1-1/4"	Polyethylene	42,2	3,9	0,42	0,077
SDR-11 1-1/2"	Polyethylene	48,3	4,4	0,42	0,076
SDR-11 2"	Polyethylene	60,3	5,5	0,42	0,076
SDR-13.5 1"	Polybutylene	28,6	2,2	0,22	0,121
SDR-13.5 1-1/4"	Polybutylene	34,9	2,6	0,22	0,117
SDR-13.5 1-1/2"	Polybutylene	41,3	3,1	0,22	0,118
SDR-13.5 2"	Polybutylene	54,0	4,0	0,22	0,116

The position of the pipes inside the borehole is also of importance for the heat transfer to the ground. To reduce the resistance between carrier fluid and ground, the smallest spacing in between is advisable, the closer the pipe to the borehole wall, the better, as illustrated in Figure 8.

The previous statement can be a little complicated though. A bigger spacing between pipes will mean that more heat is transferred on one-half of the borehole due the pipe-in,

while part of this heat will be taken out by the pipe-out. On the other hand, too small spacing will increase the thermal resistance provided by the filling material. Furthermore, big amount of heat will flow directly between pipes if the spacing is too small or if they are in direct contact. Therefore, it is advisable to select a filling material with similar thermal properties to the surrounding ground, as well as to select the correct spacing based on borehole and pipes size.

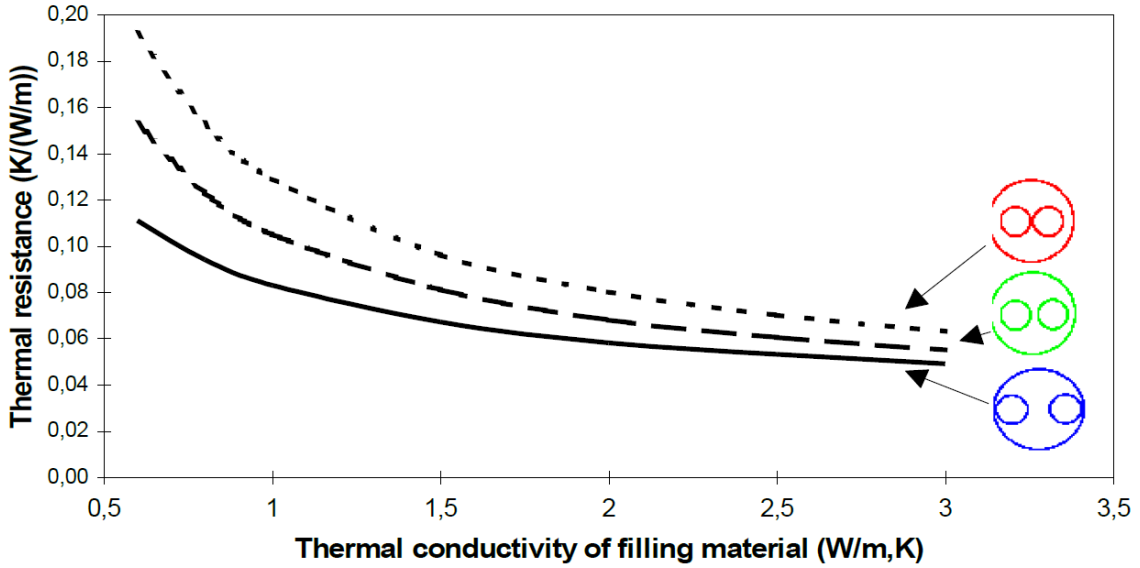

Figure 8. Borehole thermal resistance [m·K/W] for a single U-pipe as a function of filling material thermal conductivity (1.5 – 2-.0 [W/m·K]) for three different positions of the U-pipe shanks, non-laminar flow conditions (Re≈3000). After Hellström (2011).

2.2.2 Filling material

Different materials can be used to fill the BHE to ensure the heat transference between the pipes and the ground, as mentioned by Göran (2011) in his chapter 6 of the *Geotrainet Manual for Designers of Shallow Geothermal Systems*.

The selection of the grouting or filling material depends mostly on the local conditions where the UTES takes place. In Sweden and Norway, for example, BHEs in hard rock are left un-grouted and filled with groundwater, and some occasions with ice, which has an acceptable thermal conductivity ($\lambda = 2.3$ [W/m·K]) compared to other mineral sources (see Table 3), besides it availability in high latitude countries.

Contrastingly, stagnant water has a low λ value. Nonetheless, thermal gradients will occur due to natural convection, thus enhancing the heat transfer between the heat exchanger and the surrounding ground (Gehlin 2002).

In the case of North America and Central Europe, different backfilling materials are used to grout the borehole and ensure the proper thermal contact. Bentonite and some types of cement are employed for this purpose; they can be placed as pure bentonite/cement or mixed with different kind of aggregates to enhance the thermal conductivity of the filling material. Each type of grout has advantages and disadvantages. Bentonite-based grouts swell easily, have high viscosity, and are hard to mix, making difficult their handling. In the latter case, there is a tendency to shrinkage; the curing times are long and they may affect the groundwater quality (Marcucci 2014).

The correct selection of filling material is crucial for the success of the shallow geothermal systems, grout with a high or competent thermal conductivity aids to reduce the overall borehole thermal resistance, meaning a more efficient heat transfer between source and ground. Best-case scenario is achieved when the filling material and the host medium have a similar λ value; reducing the resistance to heat flow since filling material and ground act as one domain. For such case, the diameter of the borehole become less of a critical factor for the BHE performance.

Table 3. Thermal conductivity (W/m·K) of borehole-filling material, extracted from Hellström (2011).

Material	**Thermal conductivity [W/m·K]**
Sand, gravel – dry	0.4
Water (stagnant)	0.6
Bentonite 10 %, water	0.7
Bentonite/cement/sand, 9/9/20 %, water	0.7-0.8
Sand, moist	1.0
Bentonite 10 %, frozen	1.4
Bentonite/quartz-sand, 12/50 %, water	1.5
Gravel, water-saturated	1.8
Ice	2.3
Cement/sand, 27 %/58 %, water	2.4
Quartzsand, water-saturated	2.4-2.7
ThermoCem (cement/graphite)	2.0

2.3 Thermal Response Test

The correct estimation of the local medium thermal properties is necessary when designing any sort of BHE for any kind UTES Application or Ground Source Heat Pump (GSHP). The most important parameter is the thermal conductivity λ. This parameter is entirely site-specific and cannot be influenced by engineering unless the complete modification and construction of the site (e.g. water tank storages and water-gravel-pit storages).

For small-scale purposes (residential houses), the *in situ* thermal parameters are estimated according to the prevailing geology, and based on available literature values and previous tests considering the final use and the depth of installation. Notwithstanding, for large-scale projects the value of λ must be measured on site through testing due to the project size and economical resources. The local thermal parameters can be obtained by conducting a Thermal Response Test (TRT).

A TRT consists of a continuous heat injection or extraction imposed on a test BHE. The power applied, and the input/output temperatures in the BHE pipes are measured. The resulting temperature readings are used to determine the thermal conductivity of the ground λ_s, and to test the borehole's performance (Gehlin and Spitler 2003). Besides λ_s, the borehole thermal resistance R_b can be determined for the current BHE configuration.

Different methods are used to evaluate the temperature curve obtained from the readings. The resulting value of the total heat flux underground is noted as the thermal conductivity. As different local effects are automatically included in the reading (convective heat transport, local disturbances, etc.) the term is better defined as "effective" thermal conductivity λ_{eff} (Sanner *et* al. (2005)). Due to the nature of λ_{eff}, R_b also includes all borehole specific issues in one quantity, which in the end are hardly identified with the conventional TRT method.

Mogensen (1983) made the first demonstration to determine both parameters (λ_{eff}, R_b) of the TRT concept in a borehole, previous analysis methods were based on the works of Carlsaw & Jaeger (1959), and Ingersoll & Plass (1948).

Mogensen's response test took place in a small house in Sweden on a ground heat pump by applying a constant heat extraction rate to a borehole and measuring the temperature development over time. The main purpose was to determine R_b of a particular BHE (double coaxial, 62 mm BH, crystalline rock) (Spitler and Gehlin 2015).

After this first test and during the 90's, several other experiments took place around the world, improving practices and equipment to perform the tests, and the study of the interaction occurring between BHEs and the surrounding media.

Diverse test rigs have been developed and used when conducting TRTs; however, all of them follow the same principle and have the basic elements:

- A thermally equilibrated closed-loop borehole,
- A circulation pump and a flow meter for the carrier fluid,
- A constant heat source,
- Temperature sensors in the inlet and outlet of the system,
- Data collection equipment.

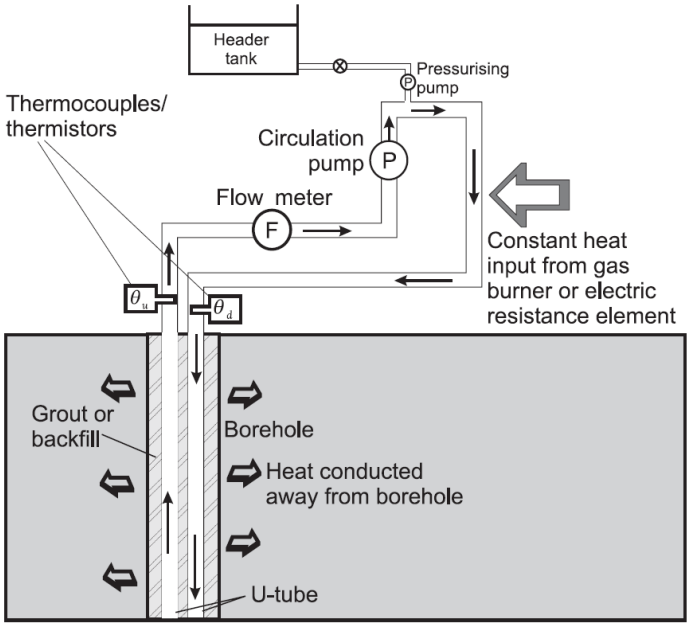

Figure 9. Schematic of the operational principles in a TRT rig after Banks (2012).

Time, as in different applications, is crucial in the development of a TRT. Different authors suggest different durations for the TRT, ranging from 12-14 hours in the case of Smith (1999b), up to a minimum of 50-60 continuous hours for Austin *et* al. (2000) and Gehlin & Spitler (2003). This refers mainly to the fact that when estimating the *in situ*

thermal parameters, the thermal conductivity becomes stable for data series starting at 10-15 hours, and becomes unstable again when the data series becomes too short (<30 hours) according to the observed effect by Gehlin (2002).

The result of conventional TRTs is very useful for the accurate sizing of BHE installations. However, it presents merely an average thermal conductivity of the surrounding ground and an average borehole thermal resistance.

Different to the consulted literature where the BHEs are vertical and over 100 m deep, our test BHE is horizontal with a depth maximum variation of 14° from the beginning to the end of the borehole (for debris draining purposes). We can then consider the thermal properties of the rock will not change if no discontinuities are found during drilling.

Detailed descriptions on the TRT are found under different sources (Gehlin (2002), Sanner *et* al. (2005), Banks (2012), and Spitler (2015)). Additional sources, such as Acuña *et* al. (2009), present new developments on the subject such as the Distributed Thermal Response Test, where the TRT results are enhanced by measuring temperatures at different depths in the borehole during the test.

The principle on which the TRT analysis is based to obtain the *in situ* parameters is the conductive heat transport in a medium with constant diffusivity α and absence of heat generation, described by the *heat transfer equation* (14) (Oberdorfer (2014), Al-Khoury (2012))

$$\nabla^2 T = \frac{\partial^2 T}{\partial x^2} + \frac{\partial^2 T}{\partial y^2} + \frac{\partial^2 T}{\partial z^2} = \frac{1}{\alpha}\frac{\partial T}{\partial t} \tag{14}$$

From the different analysis procedures used to evaluate the conductive transfer of heat, one of the simplest analytical methods of analysis is the Line Source Method (LSM), which is a simplification of the Cylindrical Source Method. The LSA is a solution to a pure conductive heat transfer process involving an infinite line source that begins generating heat constantly at time zero. The simplicityin this procedure is used to evaluate the results in the TRT.

A line source solution given in the form of an infinite series was developed by Whitehead (1927). Later, Ingersoll & Plass (1948), and Carslaw & Jaeger (1959) formulated

solutions based on the line source, being the latter one a solution that approximates temperature T at a radius r.

This expression can be obtained from Eq. (15) as presented by Oberdorfer (2014), where $T(t)$ goes to T_0 for all points in space except for *(x', y', z')* where it goes to infinity. With this solution and considering an equally distributed heat injection $q(t)$ per unit length starting at *t=0*, Eq. (14) can be rewritten like

$$T(t) = T_0 + \frac{1}{4\pi\lambda}\int_0^t \frac{q(t')}{t-t'} e^{-r^2/4a(t-t')} dt' \tag{15}$$

By applying a temporary constant heating rate $q(t>0) = q_0$ the expression becomes

$$T(t) = T_0 + \frac{q_0}{4\pi\lambda}\int_{\frac{r^2}{4\pi\alpha}}^{\infty} \frac{e^{-u}}{u} du \tag{16}$$

With the exponential integral term as the error function, which has no elementary solution

$$-Ei(-x) = \int_x^{\infty} \frac{e^{-u}}{u} du \tag{17}$$

Even with no elementary solution, an approximation can be made. Examples of this can be seen in Abramowitz & Stegun, and Gautschi & Cahill, with a formulation for the series expansion

$$Ei(x) = -\gamma - \ln(x) - \sum_{n=1}^{\infty} \frac{(-1)^n x^n}{n \cdot n!} \tag{18}$$

With this formulation, is possible to approximate the solution of the temperature at the borehole wall given a radius r_b.

$$T_{b(t)} = T_0 + \frac{q_0}{4\pi\lambda} \cdot \left[\ln\left(\frac{4\alpha t}{r_b^2}\right) - \gamma\right] \tag{19}$$

The maximum error in the temperature rise is 2% for this solution (Hellström 1991) compared to a full series expansion when

$$t > \frac{5r_b^2}{\alpha} \tag{20}$$

Banks (2012) considers this as the minimim time required for the logarithmic behaviour of the temperature gradient to become mathematically valid.

Other authors are a bit more conservative though. Ingersoll *et* al. (1954) and Gehlin (2002), for example, recommend 4 times the minimum time stated in Eq. (20).

$$t > \frac{20 r_b^2}{\alpha} \tag{21}$$

The overall thermal conductivity of the system can be obtained from the slope of the semilogarithmic curve for times bigger than Eqs. (20)-(21) once the slope reaches a linear behavior, as shown in Figure 64 in Chapter 5.

Additionally, Bauer *et* al. made reference that for the steady state, the description of the thermal flow is not valid for variations below

$$t = \frac{5 d_b^2}{4\alpha} \tag{22}$$

This is the main reason for the length of the test duration (>50 h). As mentioned in previous paragraphs, the thermal conductivity evaluated in this test includes all other aspects inherent in the borehole environment, therefore the effective thermal conductivity.

$$\lambda_{eff} = \frac{q_0}{4\pi} \cdot \left(\frac{\Delta T_b}{\Delta \log(t)} \right)^{-1} \tag{23}$$

The temperature at the wall of the borehole (T_b) cannot be usually measured, mainly due to the length, configuration, and environment of the boreholes; the positioning of the monitoring equipment, and the characteristics of the monitoring equipment (glass fiber probes has shown better improvement in this field). Taking this into consideration, only the temperature of the fluid can be experimentally determined, frequently taken as an arithmetic mean of the inlet and outlet temperatures T_f.

$$T_f - T_b = R_b q(t) \tag{24}$$

$$T_b = T_g + \Delta T_{b(t)} \tag{25}$$

The thermal borehole resistance R_b represents then the link between T_f and T_b and can be approximated theoretically as the sum of the thermal resistances of the pipe and the grout (R_p, R_g respectively) according to Marcotte & Pasquier (2008).

$$R_b = R_p + R_g \tag{26}$$

$$R_g = \frac{1}{S_b \lambda_g} \tag{27}$$

Where S_b as the shape factor of the pipe configuration inside the borehole and can be defined by

$$S_b = \beta_0 \left(\frac{d}{D_o}\right)^{\beta_1} \tag{28}$$

With β_0 and β_1 are the geometrical parameters function of the U-pipe's position in the borehole. On the other hand, pipe thermal resistance englobes the values for the effects of conduction and convection

$$R_p = R_{cond} + R_{conv} \tag{29}$$

$$R_{cond} = \frac{\ln\left(\frac{D_o}{D_i}\right)}{4\pi\lambda_p} \tag{30}$$

$$R_{conv} = \frac{1}{2\pi D_i h_i} \tag{31}$$

where d is the borehole diameter, D_i and D_O the inner and outer diameters of the pipe; h_i is the inside film coefficient and, λ_g and λ_p are the thermal conductivity values for the grout and the pipe.

Oberdorfer (2014) highlights, the reduction of a BHE to a line source is only valid in the range of a number of approximations and that there are some restrictions that have to bore in mind when carrying out the calculations.

1. Constant heat injection rate.
2. Homogeneous initial temperature.
3. Thermal parameter distribution.
4. Temperature dependence of inherent parameters.
5. Conductive heat transport.

3 *In situ* experiment

3.1 Description

Two numerical models have been developed to simulate and explain the heat flow in arrays of BHEs for the seasonal thermal storage at high latitudes. To validate the performance and results of such models, an *in situ* experiment in the underground research facilities of the Aalto University was designed.

The experiment aims principally to observe the development of the heat field in the hosting ground and under controlled conditions for its posterior comparison against the results from the numerical modelling of thermal flow. The purpose of the comparison is the validation of the numerical models for their applicability to simulate future and more complex scenarios.

The testing of the type of rock present on the tunnel has been done to obtain the mean thermal parameters of the local medium for simulated results closer to the observed ones. Previously simulations have been performed with the use of average values of λ, C_p, and α for the host rock taken from a previous study performed in Otaniemi by the Finnish Geological Service (GTK) for the Aalto University Real State Agency (ACRE 2016) and from literature.

The experiment consists on two stages. The main stage relates to the monitoring and evaluation of thermal flow in the rock and its storage capacity. An additional stage is performed to determine the local thermal parameters of the ground.

The main stage consists of the evaluation of the heat storage capacity for the selected field through the continuous injection of heat. This stage is divided into two phases.

In the first phase, hot water is circulated through the installed BHE for a period of 21 days at a constant temperature of 50°C (min); hence, the heating phase. The following step is to stop the circulation of the carrier fluid cutting the constant source of thermal energy into the rock; hence, the cooling phase. This phase allows part of the energy to dissipate through the boundaries of the ground, i.e. between rock and air and to migrate to other areas of the rock mass due to conductivity.

The evolution of the heated field around the BHE is monitored during the heating and cooling phases to assess the amount of energy retained by the rock mass after the cooling period.

The second stage of the experiment is the implementation of a TRT conducted with the BHE on site to determine the thermal conductivity of the rock (λ). During this stage, the inlet and outlet fluid temperatures are recorded for a minimum of 60 hours while the BHE is subjected to a constant power source.

The resulting parameters of the test are the effective thermal conductivity λ_{eff} and the borehole thermal resistance (R_b) for the tested BHE configuration and evaluated from the temperature curve obtained from the readings. The obtained *in situ* values are considered for the update of the model parameters for a more accurate simulation.

3.2 Settings

3.2.1 Heat flow and storage stage

The aim of this first stage is to assess the thermal flow occurring in the rock comprehended in between the BHE and the monitoring borehole. The capacity of the ground to contain the energy on a seasonal basis is simulated by two experiment phases in which heat is transferred to the ground for a determined period, followed by a non-energy transfer period, in which the energy is to be stored. The phases are defined as heating and cooling.

During the heating phase, a constant inlet temperature, of at least 50 °C, is input to the system for 20 days. The constant heat simulates an idealized heat pulse into the storage as energy is directly injected into the system without any withdrawal or power interruption while charging, as normally will occur in the current seasonal shallow storage systems.

Table 4. Storage experiment phases and parameters

Phase	Heating	Cooling
Period [days]	20	15
Temperature [°C]	50	N/A
Flow rate [lt/s]	0.065	0.0
Velocity [m/s]	0.36	0.0

3.2.2 Thermal Response Test (TRT)

Additional to the experimentation of heat flow and storage, the implementation of a thermal response test was thought. The purpose of this stage is to obtain the actual borehole thermal resistance R_b value for the BHE configuration achieved and used in the experiment. To get this value, the following experiment parameters are considered.

Table 5. TRT parameters

Parameter	Value (base)
Duration [hrs]	60 (minimum)
Temperature [°C]	50 (minimum)
Power [kW]	2.4-3
Flow rate [lt/s]	0.06
Velocity [m/s]	2.0
Regime	Turbulent

These values are based on the capacity of the water heater and circulation pump and considered as a starting point, the correct values are to be obtained from the mean values observed during the experiment.

3.3 Location

Finland is located on the Fennoscandian (or Baltic) Shield, composed by an old and stable bedrock (Archaean 3100-2500 Ma, and Proterozic 2500 – 1300 Ma), covered by relatively young Quaternary soil layers less than 5 m thick, as result of the progress and melting of glaciers in the Latest Ice Age.

The crystalline bedrock is characterized by granitoids, gneisses, and other metasedimentary or metavolcanic lithologies (Kukkonen (2000)). The typical geologic profile in southern of Finland, where Espoo is located, is divided in coastal with plutonic rocky hills partially covered with thin moraine layers, and valleys and flat terrains covered by thin layers of clay or silt. The underneath geology consists of Paleoproterozoic granite. The bedrock is normally found in almost-horizontal beddings of different thickness around the Otaniemi and Helsinki region, forming blocks of average to big size.

The experiment took place in the Aalto University, School of Engineering – Research Tunnel, located under the Otaniemi Campus, in Espoo, Finland. The campus is located on a small peninsula that reaches into the Maarinlahti (fi. Maarin Bay), a small influx of the Gulf of Finland, an area consisting mainly on University buildings and student

residences of medium size. Different green areas also to be found in the territory together with the campus buildings.

The tunnel is located approximately 18 m below the surface level (to the roof of the tunnel), varying from 19.3 m at the entrance of the research tunnel, to 16 m at the end of it, and with a height between 4.5 and 3.1 meters for the same points previously mentioned.

Figure 10 illustrates the research tunnel as in the original layouts, where the top part of the image shows the cross-section view of the tunnel along the driven axis, while the bottom part shows the plant view of the tunnel with the additional openings, corresponding to the meeting area (right) and the compressor room (left).

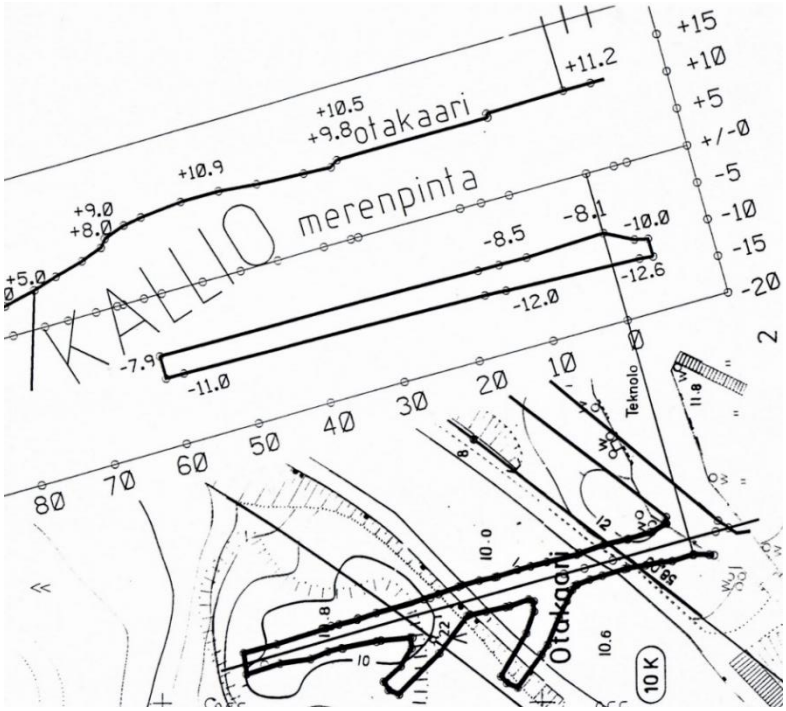

Figure 10. Original research tunnel layout

The characteristic rock of the area is granite with presence of hornblende gneiss, with a good effective thermal conductivity value of *3.3 W/(m·K)*. This value was obtained after a geothermal potential study by the Finnish Geological Service (GTK) during the winter 2014-2015, commissioned by Aalto University Properties to evaluate the geoenergy potential of the area as part of Aalto's efforts aiming to transform the campus in an energy self-sufficient campus.

The study consisted in TRTs performed in three 300 m deep boreholes in the bedrock found in the Campus. With the results from these studies, a map has been created to

represent the areas with the best potential for the geoenergy use (Figure 11) ranging from excellent (green) to mediocre (red).

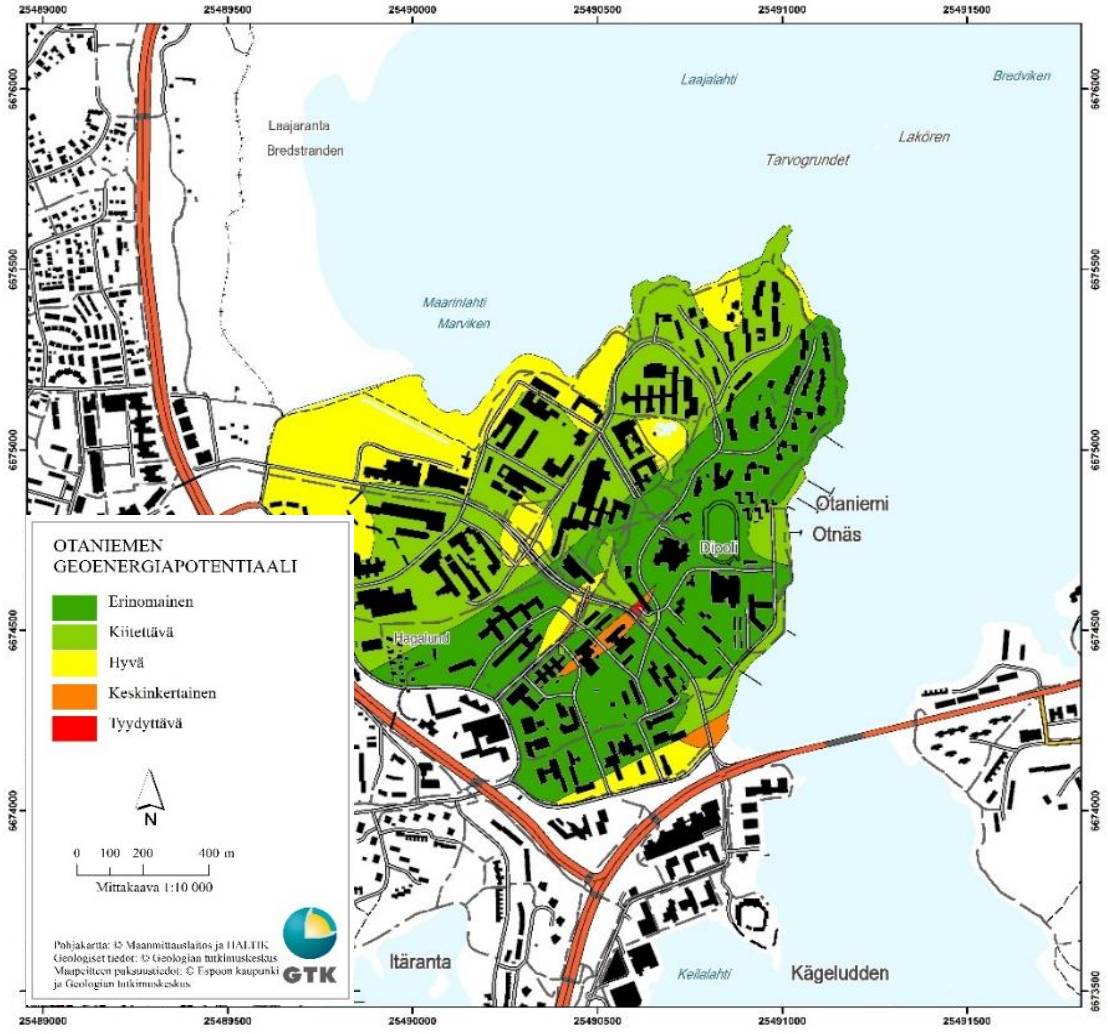

Figure 11. Otaniemi Geoenergy Potential Map. Modified after GTK (2016).

From this study an average $\lambda_{eff} = 3.3\ W/m \cdot K$ for the bedrock was determine, a value consistent with range values found in literature sources, Eppelbaum *et* al. (2014), Peltoniemi (1996), and Kukkonen & Peltoniemi (1998).

In general, the overall location of the tunnel is in an area with a high potential for geoenergy, underlying in the dark-green area. Considering the drilling was to be perform horizontally instead of vertically, the selection of the area was of importance to assure the correct development of the experiment.

The following was to define the wall where the drilling would take place. Different areas were considered for this purpose, the selection of the final spot was based on analyzing the pros and cons of each location and the effect on the performance of the experiment.

Figure 12 illustrates the five different areas inside the research tunnel considered as viable for the drilling of the BHE.

Between the factors taken into consideration for the area selection we can find,

- Access to water and power supply.
- Continuity in the rock mass.
- Undisturbed area, at least 1.5 m radius around the experiment hole.
- Maneuverability of drilling equipment.

Figure 12. Layout of the research tunnel and possible areas of drilling.

A video inspection was done after the borehole drilling to assess the homogeneity and continuity in the rock mass crossed in a second approach to identify the presence of diverse rock types within the BHE. The images from this surveying returned the presence of at least two rock types. The identification of the rock types was possible with help of Prof. Jussi Leveinen (2017), Engineering Geology from the Civil Engineering Department, Aalto University, School of Engineering.

The rock types in the research tunnel have been identified as:

- Fine-grained hornblende-biotite gneiss (Figure 13, left)
- Migmatic granite (Figure 13, right)

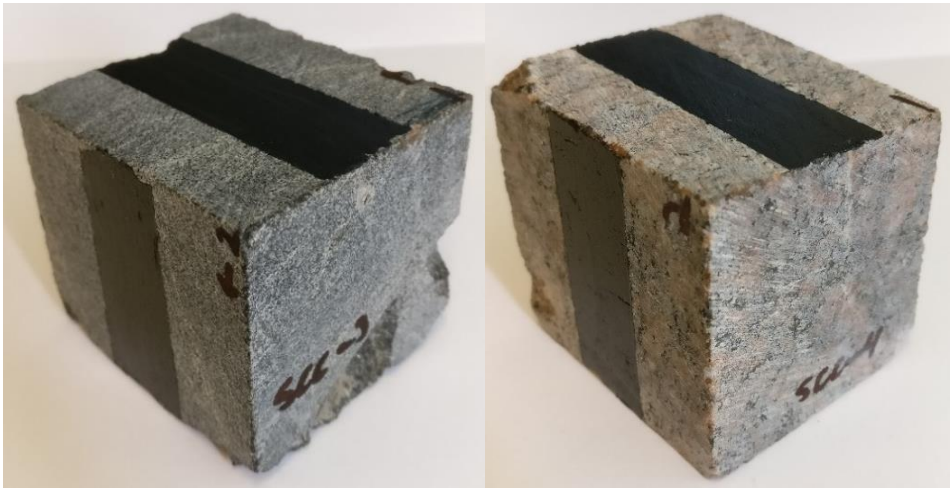

Figure 13. (Right) Sample of Gneiss. (Left) Sample of Granite.

Considering the presence of more than one rock, it was decided to perform a laboratory test to estimate the values of the main thermal parameters (λ & α), the bigger the difference of these parameters between the rock types, the higher variability in the heat flow process for each material. The laboratory testing consisted in the optical scanning of rock's surface with a *Thermal Conductivity Scanning (TCS)* with the support of the Geophysics department of the University of Helsinki.

Three samples of each rock type were tested, proceeding from rocks extracted from the tunnel walls with similar characteristics to the rock present where the experiment takes place. The rocks were sawed in cubes to create flat surfaces or faces, from which three were scanned.

The determination of the thermal conductivity is dependent of the scan direction, being determined perpendicularly to the direction of movement. The selection of the faces to be scanned (Figure 14) was done based on the movement direction of the optical sensor with respect to the rock foliation; one parallel, one perpendicular, and one normal to the plane of foliation.

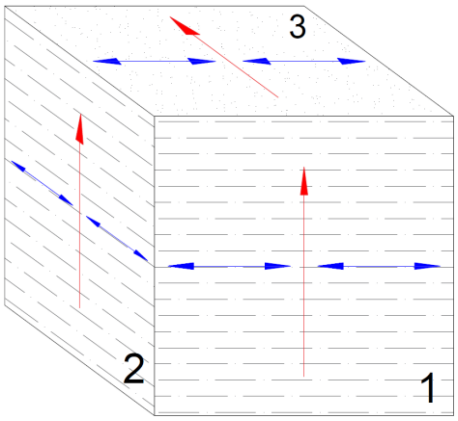

Figure 14. Schematization of rock sample with scan directions.

A description of how the TCS machine works and its advantages can be in found under Lippmann & Rauen (2017) and TU Darmstadt (2017) website. A summary of the TCS is also present in *Appendix E* together with the results obtained for the analyzed samples.

The physical properties of the samples are presented in Table 6. Likewise, the thermal parameters obtained from the TCS are shown in Table 7 & 8.

Table 6. TCS samples physical properties

Sample	Rock type	Weight [kg]	Volume [x10^{-3} m^3]	Density [kg/m^3]	ρ_{ave}
SCC1	Gneiss	0.396	0.150	2,641.667	*2,501.431*
SCC2	Gneiss	1.060	0.400	2,648.775	
SCC3	Gneiss	0.443	0.200	2,213.850	
SCC4	Granite	0.478	0.200	2,392.100	*2,507.200*
SCC5	Granite	0.787	0.300	2,622.100	
SCC6	Granite	0.878	0.350	2,507.400	
A	Grout	1.844	0.950	1,940.989	*1,925.702*
B	Grout	1.891	0.990	1,910.414	

Table 7. TCS results for Gneiss samples

Gneiss Direction	λ_{ave} [W/mK]	α_{ave} [x10^{-6} m^2/s]
1	3,076	1,621
2	2,704	1,264
3	2,541	1,468
Overall	**2,774**	**1,451**

Table 8. TCS results for Granite sample

Granite Direction	λ_{ave} [W/mK]	α_{ave} [x10^{-6} m^2/s]
1	3,012	1,611
2	3,033	1,599
3	2,868	1,544
Overall	**2,971**	**1,585**

For the **gneiss** samples, the average thermal conductivity is **2.774 W/m·K**, while for **granite** the value is **2.971 W/m·K**.

Considering both rocks in the experiment borehole, λ_{ave} is **2.872 W/m·K**, and α_{ave} equals **1.518 x10-6 m²/s**. These values are lower than the average reported by GTK; however, is valid to consider the reported value comes from a much larger sample and with a different method for granite solely.

An average thermal capacity **Cp = 723.546 J/kg·K** is obtained by solving Eq. (3) using as input the values obtained from the TCS.

$$C_p = \frac{\lambda}{\rho\alpha} = \frac{2.872\left(\frac{W}{m \cdot K}\right)}{2{,}504.315\left(\frac{kg}{m^3}\right) * 1.518x10^{-6}\left(\frac{m^2}{s}\right)} = 723.546\left(\frac{J}{kg \cdot K}\right)$$

These values are posteriorly introduced into the model as the material parameters when analyzing the scenarios, resulting in a better comparison between the model results and the observed data from the *in situ* experiment.

3.4 Configuration

3.4.1 Drilling

Most of the shallow geothermal projects involving borehole heat exchangers are built with a vertical projection, ranging between 50 – 200 m of depth, avoiding the ambient air temperature influence over the ground's surface and the subsurface media up to 15 m. Another reason for such depths is the thermal gradient from the Earth's core with increases with depth. Depending on the location in the globe, the thermal gradient can be very high at shallower depths, such as in Hungary, or very low even at great depths as it is the case in Finland (I. Kukkonen 2000) where a significant temperature increment is almost negligible before 1-1.5 m deep.

The experiment configuration consisted of two boreholes, one bigger borehole where the heat exchanger was installed, the experiment borehole, and a smaller one for the monitoring of the heat flow. The boreholes are referred from now on as EXBH and MOBH, respectively. In this experiment, the orientation of the boreholes was chosen horizontally, perpendicular to the tunnel wall, with sufficient inclination for cuttings removal (Figure 15). The orientation of the boreholes was decided also thinking on the

application of this configuration on other already built places with similar characteristics, as could be underground parking lots.

Both holes were planned for a length of 5 m, with a spacing of one meter between holes. The EXBH has a diameter of 107 mm for the installation of the BHE. The MOBH, on the other hand, has a diameter of 50 mm to minimize the effects of the open borehole in the readings during the experiment.

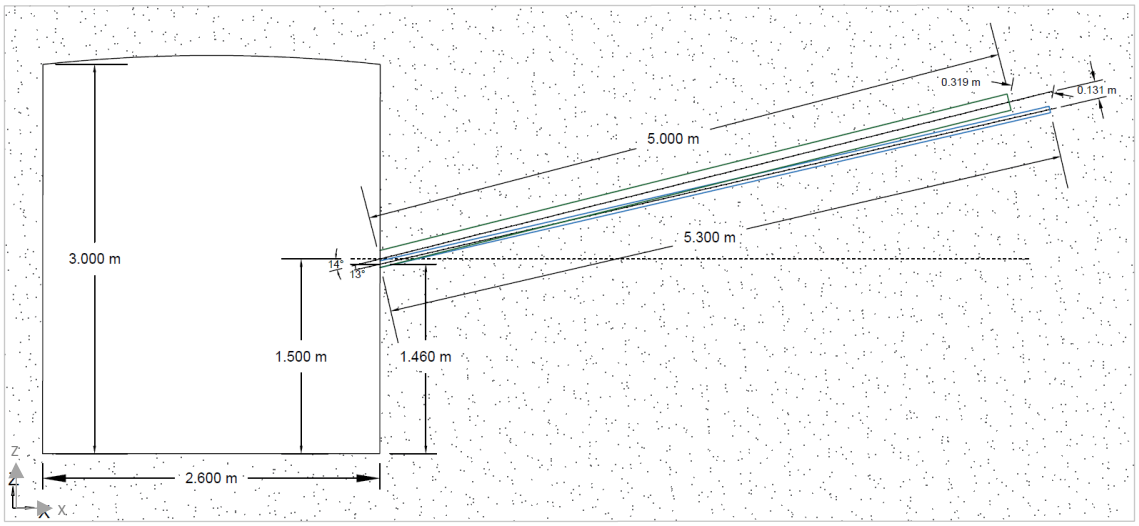

Figure 15. Cross-section view in XZ orientation of the boreholes

Figure 16. Location of the borehole collars on the tunnel wall.

The drilling was performed with a handheld drilling equipment with satisfactory results. The planned details of the drilling, as well as the result of it, are summarized in Table 9, and the plan-view representation of the resulting work is shown in Figures 16 to 18.

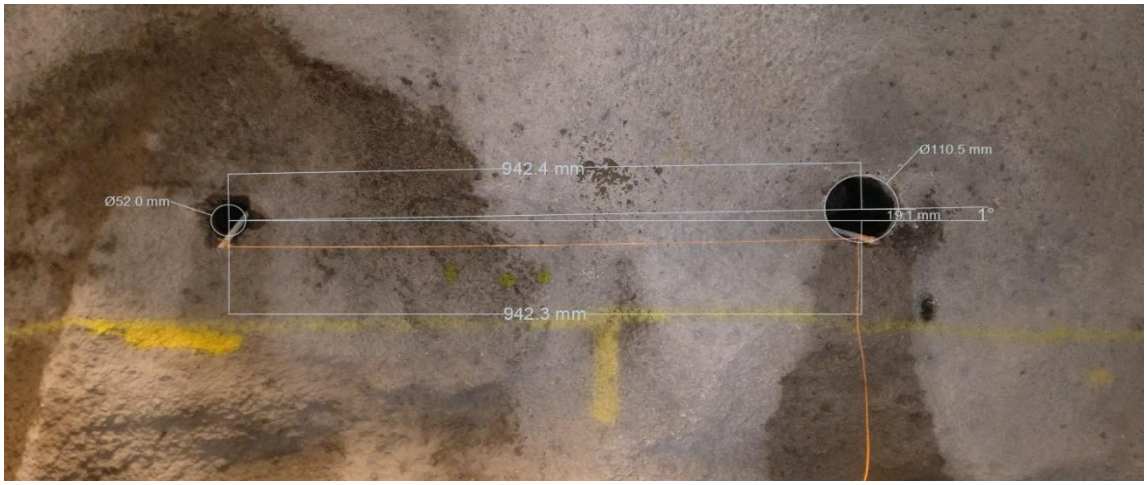

Figure 17. Distance between monitoring (left) and experiment boreholes (right).

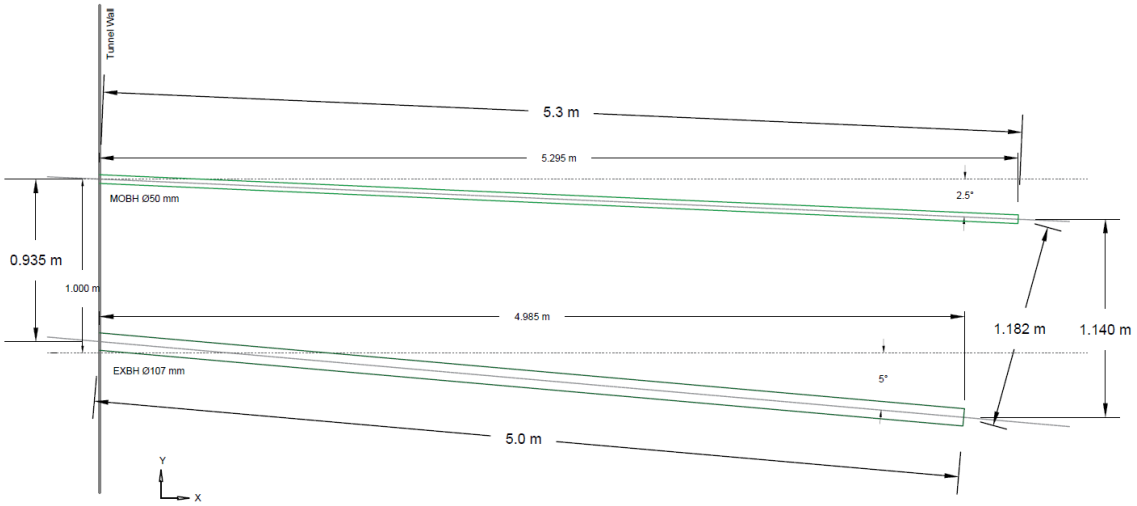

Figure 18. XY-view of the boreholes

Table 9. Planned and obtained configurations for the boreholes' drilling.

	Planned		**Achieved**	
	MOBH	EXBH	MOBH	EXBH
Height [m][1]	1.5		1.46	1.55
Inclination [°][2]	~5		13	14
Deviation [°][3]			2.5	5
Spacing [m]				
Collar	1.0		0.935	
Toe	1.0		1.182	
Diameter [mm]	50	100	50	107
Length [m]	5.0	5.0	5.3	5.0

[1] From the tunnel floor to borehole's center axis
[2] From the horizontal
[3] From the perpendicular to the wall ⊢

3.4.2 BHE Installation

Initially, the planned length of the BHE pipes was 5.0 m, from which **4.53 m** were achieved due to complications in the installation process.

The installation of the BHE consisted in a U-pipe composed by two PEX-a pipes joined by a customized brass U-turn. The pipes are connected to a 15 L capacity 3kW water heater through PEX-a pipes. A flowmeter with pulse counter and a circulation pump were installed in the return pipe before to the water heater. A power regulator is plugged to the water heater, adjusting the power provided to the heater by measuring the water temperature to keep it constant.

Custom-made centralizers were designed and built to fix the position of the pipes in the borehole, providing the correct spacing between shafts as well as between borehole wall and shafts.

The grouting was done using pure sulfates-resistant cement; no aggregates or thermal enhancers added. The quality of the grout material was evaluated at the beginning and end of the process by taking samples of it to determine the density of the final product.

Table 10. Grout properties

Sample	Weight [kg]	Volume [m^3]	Density [kg/m^3]
A	1.844	0.950	1,940.989
B	1.891	0.990	1,910.414
Average			*1,925.702*

Prior to the installation of the BHE, both boreholes were surveyed through a video camera to identify the heterogeneity of the rock drilled. This video inspection helped to assess the better place for the BHE installation. The parameters used for this evaluation were the presence and influence of underground water and the presence of discontinuities. Two main cracks are identified in the images retrieved from the videos taken, one for each of the boreholes.

In the EXBH, the biggest crack found in the surveying (Figure 19) seemed to be open in the section comprehended between the 2.5 m (left) and 3.2 m (right) from the collar. The fracture appears to be crossing the borehole vertically and in diagonal to the driven direction. The opening can be result of the reaming, as shards of rock were retrieve with

the cutting when drilling that exact area. Other than that, the rest of the fracture seems to be filled or was filled with cement during the grouting as no big variation in the temperature profile can be seen in the MOBH at such depth.

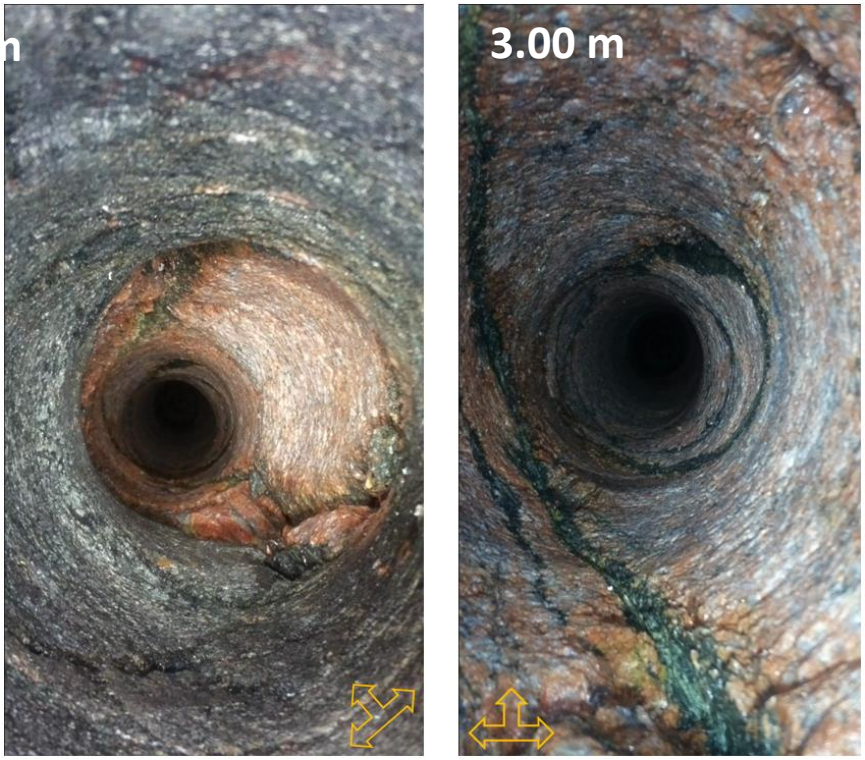

Figure 19. Open crack identified in EXBH after the drilling.

In the MOBH a possible crack is visible at the 2.0 m depth mark (Figure 20). Since the crack appears in the right-hand-side of MOBH, the area in direct contact with the heated field, it could have had influenced in the thermal flow.

Figure 20. Possible crack identified in MOBH at 2.00 m depth.

3.5 Monitoring

3.5.1 Equipment

Four measuring points were installed in the rock mass to track the thermal flow in the medium surrounding the heat exchanger. The measurement of the rock temperature along the boreholes is done with custom-made equipment built specifically for this project.

Twelve digital temperature sensors were installed along the boreholes, leaving one of them outside the rock to measure the temperature of the air close to the wall surface. Each sensor is encased in a small copper tube for protection and better contact with the wall. The sensors are connected in a series array through a data cable plugged to a Raspberry Pi® board that runs the monitoring code visualizing, measuring, and recording the temperature in each sensor.

The set composed by the 12 digital thermal sensors and the data cable is referred in this work as *Thermal Multisensor Probe* (*Probe*, for shorter reference), and identified by the letter *P*, followed the probe number from 1 to 4, e.g. *P3* stands for the *Probe 3*. Analogically, the thermal sensors are referred with the letter *S* and followed by their position number, from 1 to 12, counting from the tip of the cable towards the end plugged to the Pi board. The identifier for the sensors is, i.e. *S6 – Sensor #6*. The spacing between sensors is 50 cm, spacing that allows a clear identification of the temperature profile.

Two probes were installed along the MOBH and two in the EXBH. All the probes were placed horizontally, parallel to the tunnel floor. Probes 1 and 2 were allocated inside the EXBH along the BHE pipes. In a similar manner, Probes 3 and 4 were placed along the MOBH. The four probes were secured at half boreholes height (radius) by fixing them with the customized pipe centralizers used.

For the BHE, the probes were installed first, in the contact between rock and grout measuring the temperature of the rock at the borehole wall; and secondly, in the mid-distance between the borehole wall and the pipes axis, where the temperature of the grout can be obtained. Unfortunately, something went wrong during the installation and the probes did not respond once plugged, becoming useless for the experiment. Figure 21 shows the position of P1 and P2 in the EXBH.

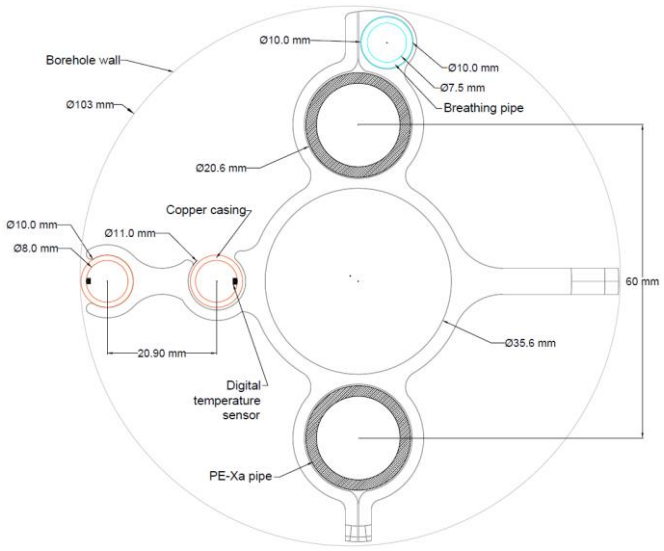

Figure 21. Cross-section view of the thermal multisensors probes installed in the EXBH.

For the MOBH, the probes were placed an opposites sides of the borehole (Figure 22) to measure in first instance, the temperature in the borehole wall holding direct contact with the heated field, and secondly, the temperature on the opposite wall to account for the effect of the void on the heat flow through the ground. The thermal sensors are hold by a customized centralizer and placed in position along the borehole via a PEX-a pipe.

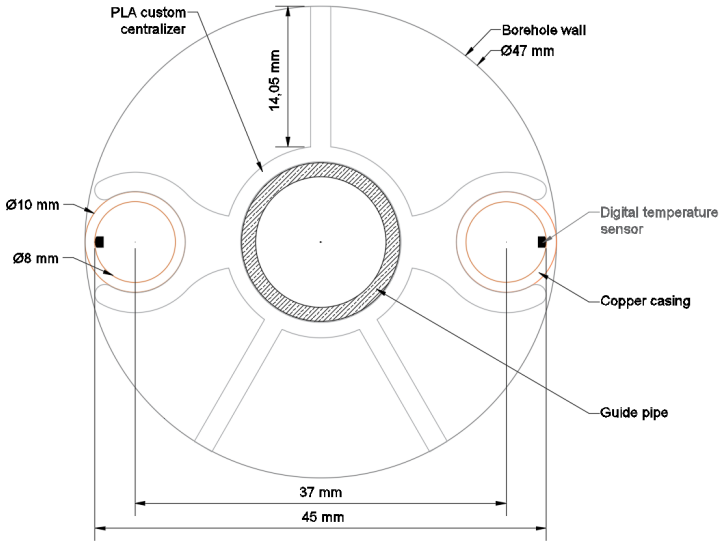

Figure 22. Cross-section view of the thermal multisensors probes installed in the MOBH.

Figure 23 conceptualizes the position of the thermal multisensory probes 3 and 4 inside the monitoring borehole. In the upper part, a three-dimensional representation is introduced, while in bottom, the planar XY view of the probes is shown. In the bottom image only four sensors are visible (S9 – S12), being the sensors located close to the tunnel wall.

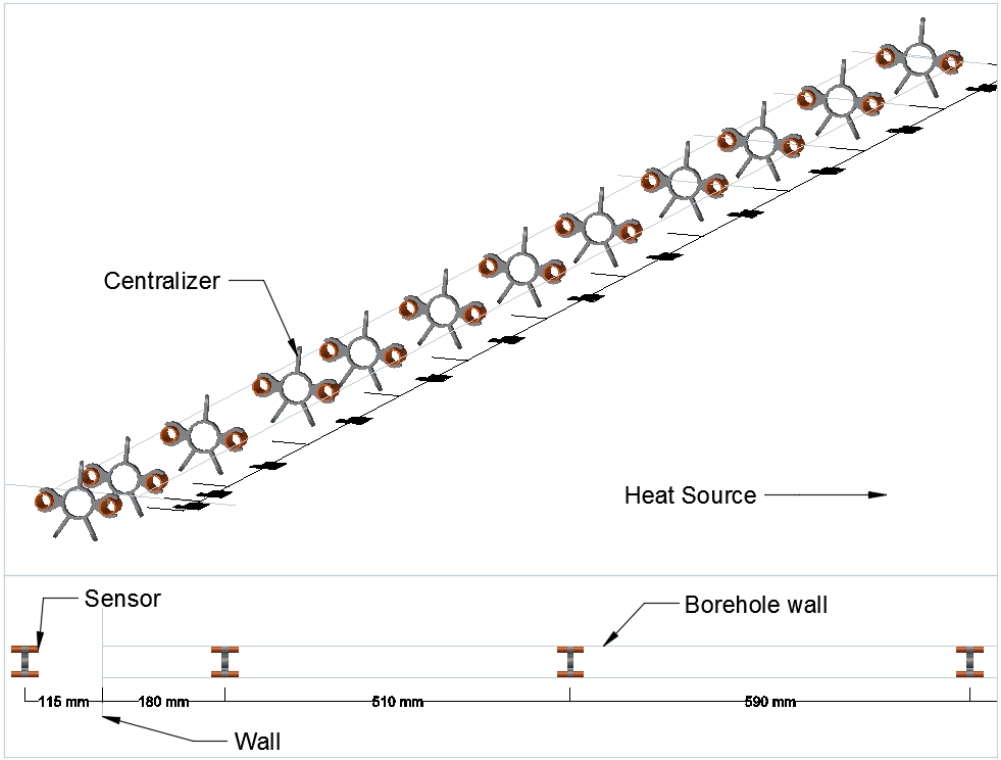

Figure 23. Conceptualization of thermal sensors array along the MOBH in 3D (up) and planar view (down)

Additional to the probes measuring the rock temperature, two thermal sensors are placed in at the inlet and outlet of the pipes. Here, the in- and outflow temperatures of the carrier fluid are monitored; allowing a better assessment of the temperature variation after the loop, and a more realistic determination of the actual heat transferred from the fluid to the ground and other elements in between. Figure 24 illustrates the thermal sensors in these points.

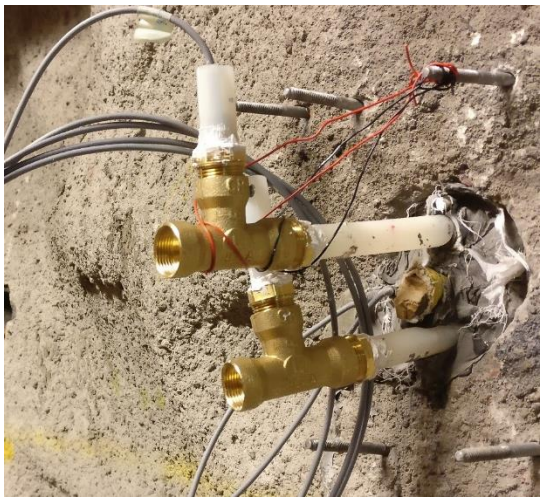

Figure 24. Thermal sensors located in the inlet and outlet points of the BHE loop.

3.5.2 Initial rock temperature (baseline)

Probe 3 was the first thermal sensor probe installed in the monitoring hole, recording the intact tock temperature for a longer period. The initial records were used to establish the baseline temperature for the ground prior to the thermal flow in the heat exchanger system.

Considering the temperature in the rock varies according to the depth at which the measurement takes place, the determination of a single temperature is intricate. Consequently, the temperature is evaluated at each one of the sensors locations along the borehole, Figure 25, and averaged for the determination of the undisturbed rock temperature T_{S_0}.

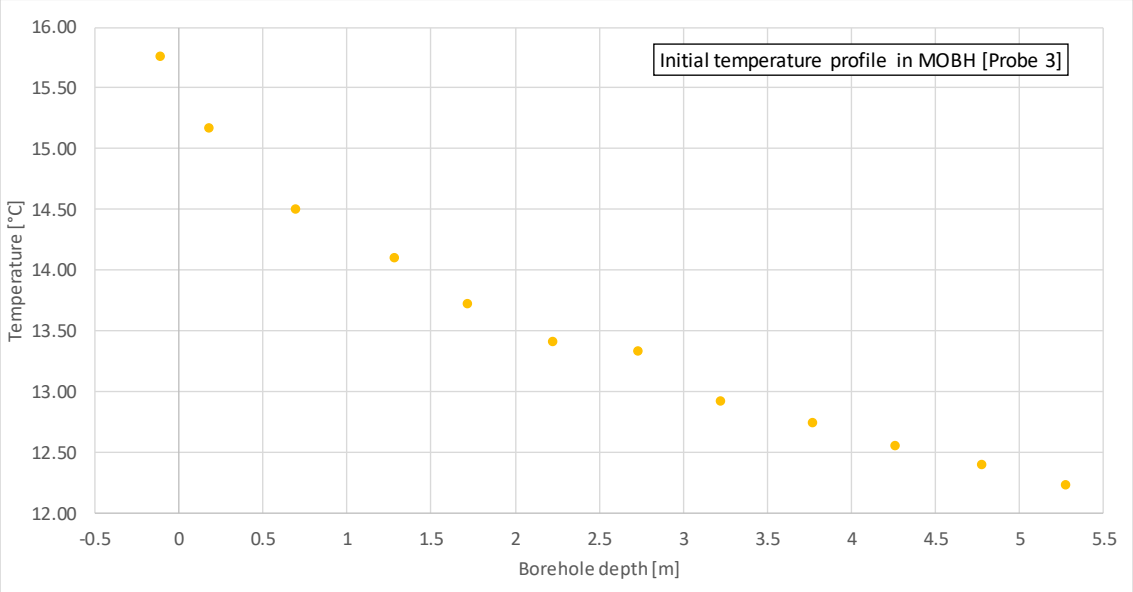

Figure 25. Probe-3. Initial temperature profile in MOBH.

An average T_{S_0} of **13.191 °C** was calculated by accounting the sensors readings after the first half meter from the wall in. The average air temperature in the tunnel recorded by S12 was **15.764 °C**.

Table 11. Temperature readings for Probe-3 sensors and their position inside the monitoring borehole.

Sensor	Position [m]	Temperature [°C]
S1	5.275	12.233
S2	4.770	12.394
S3	4.260	12.552
S4	3.770	12.741
S5	3.220	12.920
S6	2.730	13.331
S7	2.220	13.409
S8	1.710	13.724
S9	1.280	14.101
S10	0.690	14.505
S11	0.180	15.176
S12	-0.115	15.764

Figure 26 shows the records obtained from the baseline period at MOBH. Two spikes in the readings can be seen for the sensors placed in the hole, corresponding in first instance, to a moment when the probe was taken out to change the support system; and secondly, to the moment where Probe-4 was placed. These two peaks have been left out for the average temperature calculation.

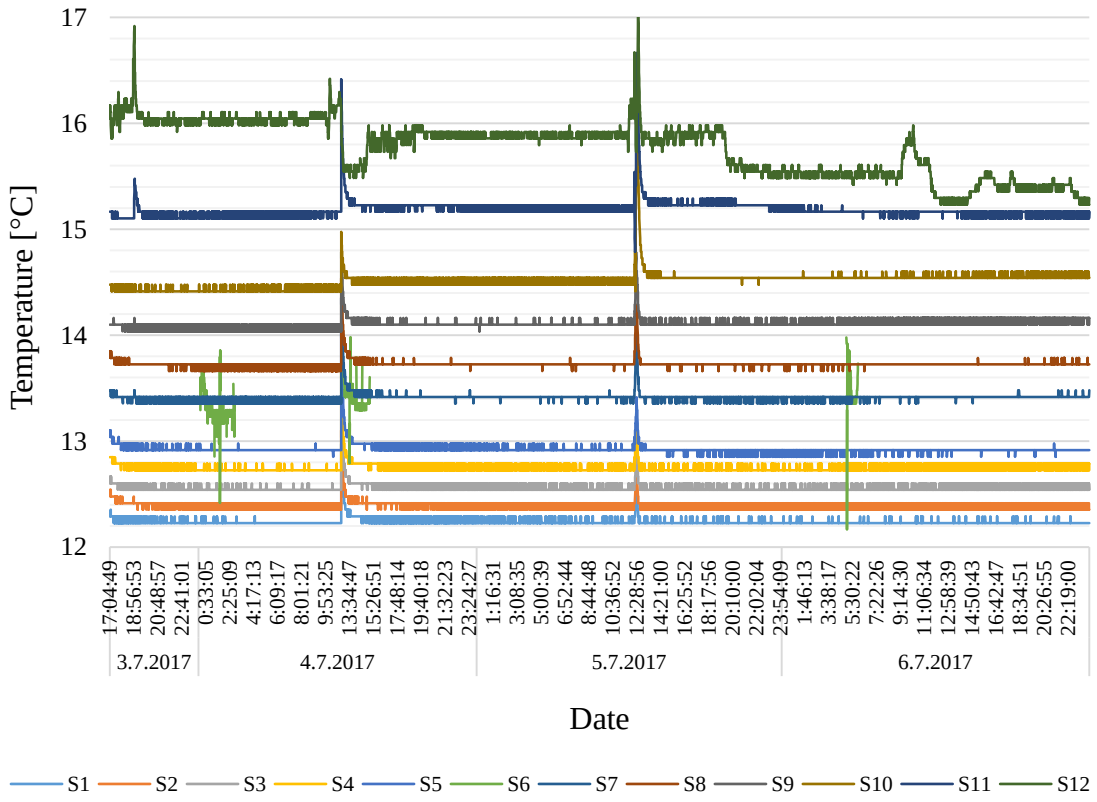

Figure 26. Probe-3. Readings prior to heat injection.

In like manner, water was pumped into the BHE and let to rest to achieve the thermal equilibrium with the system. The temperature of such water was recorded by the thermal sensors located in the inlet and outlet of the pipes. This information returns an average temperature value higher than the obtained from the sensors in the MOBH. The reason for such variation might lay in the fact that the in- and outlet sensors are located outside the wall, air temperature has inference in the readings.

Similar to the results seen for Probe 3, the peaks shown in Figure 27 correspond to the test run of hot water into the system; however, the time of injection was not long enough, therefore the abrupt decline in the temperature and its normalization. The average temperature recorded was 15.398°C and 15.409°C for Inlet and Outlet sensors respectively, with a mean temperature of **15.404°C**.

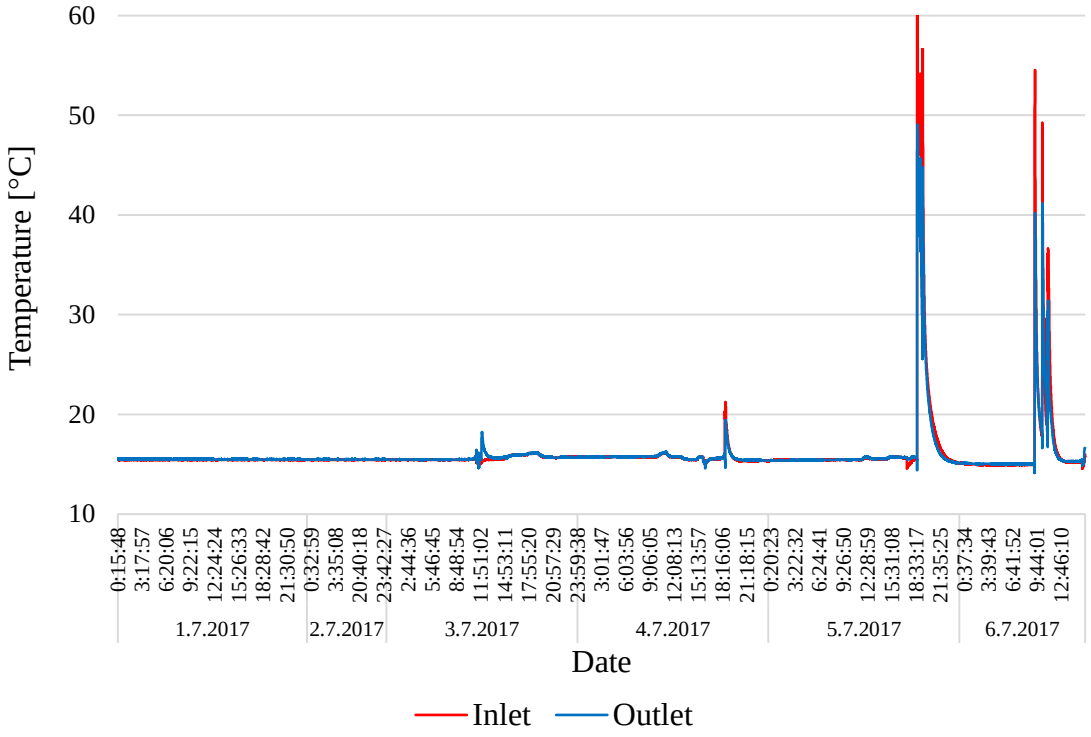

Figure 27. Inlet & Outlet records for stagnated water before heat flow.

3.5.3 Flow rate

The flow rate of the carrier fluid in the system was measured with help of a flowmeter with a pulse counter. The flowmeter is calibrated from factory, returning one liter per

second every 77 pulses. The digital pulse counter in the flowmeter is connected to an Arduino® board that transforms the electrical pulses into digital data. A Raspberry Pi® board runs the code to monitor and register the data processed by the Arduino® board.

The aim was to keep a constant flow speed as its variation impacts directly on the temperature variation in the system; however, it was not entirely possible to keep it constant through the whole length of the experiment as seen in Figure 28.

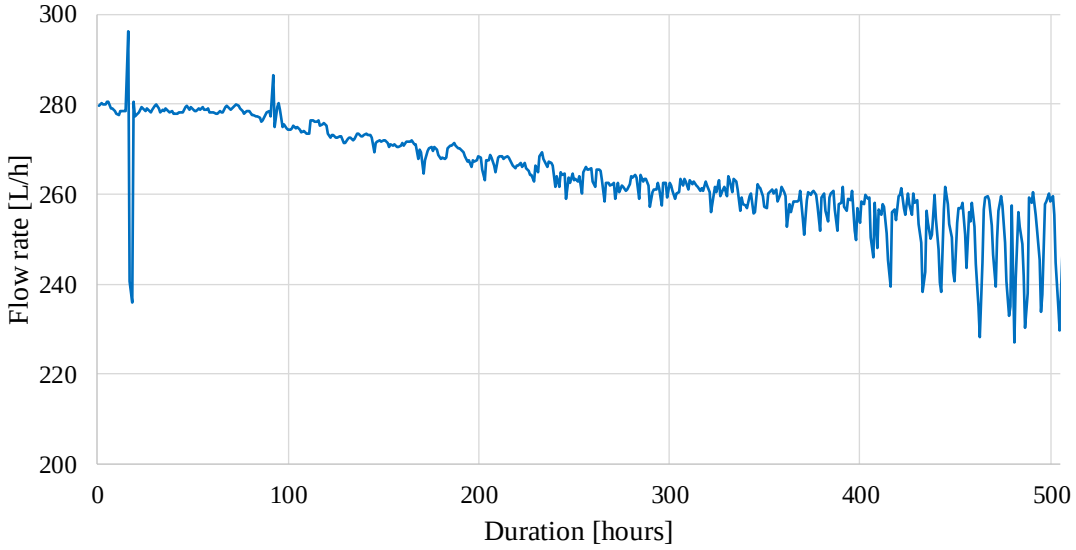

Figure 28. Flow meter records.

The flow rate presented a continuous drop no matter the measures taken. Nonetheless, the temperature did not seem to present a significant variation, probably as the drop on the fluid's flow was subtle (Figure 29).

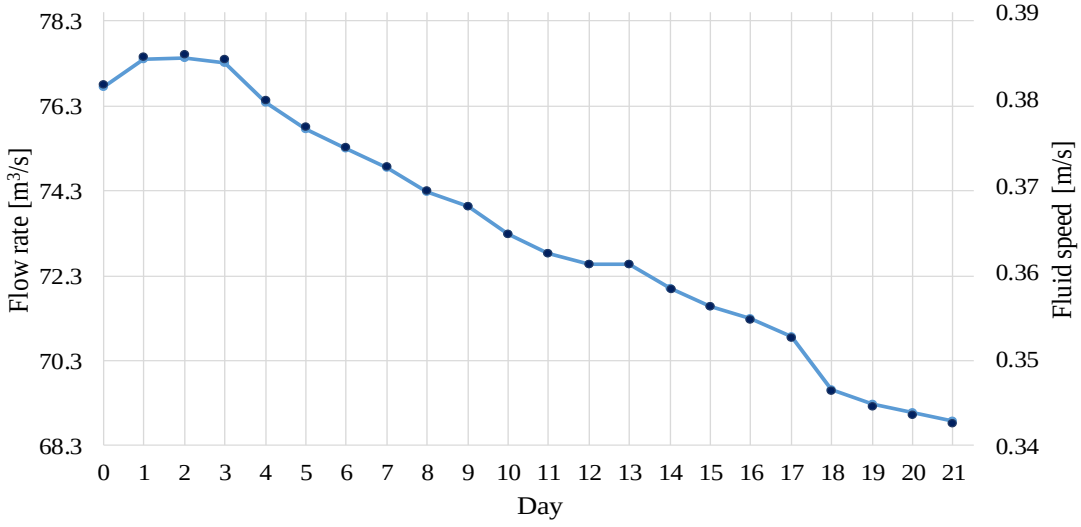

Figure 29. Monitored flow rate and fluid speed during the experiment.

An average flow rate of **0.07352 L/s**, evaluated in hours, was considered for further calculations. Considering the cross-sectional area of the pipes as **2.01 x10^{-4} m^2**, the average carrier fluid velocity is **0.366 m/s**.

3.5.4 Carrier fluid temperature

Two points were established for the temperature measurement in the carrier fluid, one at the inlet and one at the outlet of the loop. The input temperature of the fluid was set constant during the heating phase. This parameter was better controlled with the aid of a power controller installed in the water heater and the heater itself. Figure 30 shows an almost constant water temperature entering the BHE, as well as the temperature coming out of the loop. The figure also shows the variation in the flow rate had almost no negative impact in the temperature. An average temperature of **57.3 °C** was obtained for the inlet.

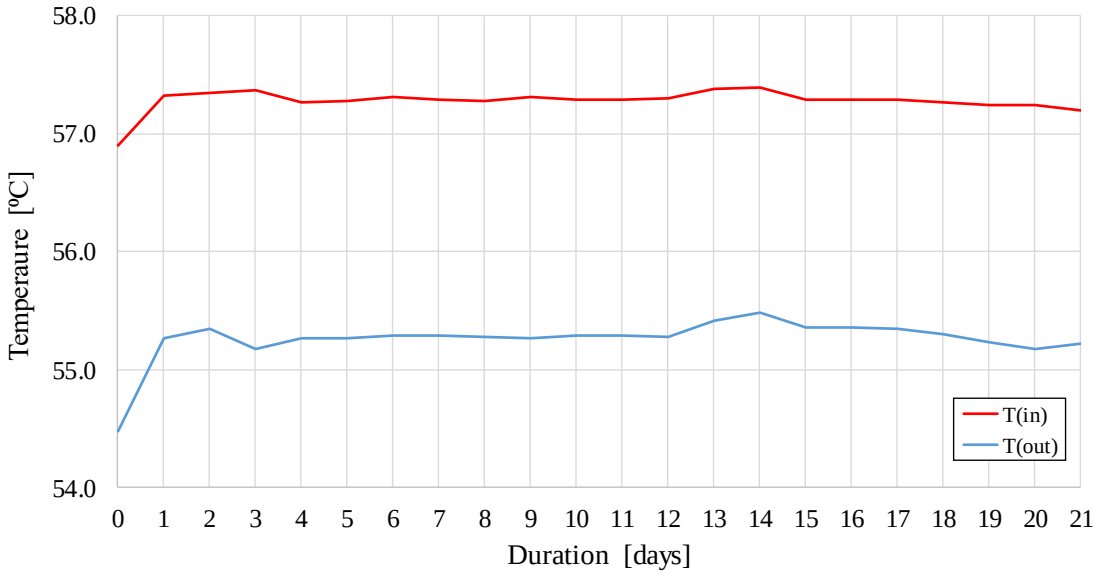

Figure 30. Monitored temperature in carrier fluid, inlet and outlet of the BHE.

4 The Models

Aalto University has performed the simulation of thermal flow for different BHE arrays thought the software COSMOL® Multiphysics. For the simulation of the different scenarios, two models have been used, namely the *Weak Form Equations (WFE)* and the *Heat Transfer in Pipes (HTiP)* models, each of them with advantages and disadvantages over the other.

The main difference between these two models is the utilization of the weight the different parameters if the borehole heat transfer equation in each of them. For example, the WFE model accounts the grout element in the variable present in the equations; however, it does not take account of the entire volume of grout for the analysis, while the *HTiP model*, being a fully 3D model does.

Another difference to note is the properties of the elements involved, the *HTiP*, being a built-in module from COMSOL, evaluates the thermodynamic properties of the carrier fluid based on the properties included in the software, while the *WFE model* requires the insertion of these properties in tabular form. A brief description of the theory behind the models is shown in the following sections.

4.1 Weak form equations

The use of the so-called *weak form equations* is the first modelling approach incorporated into COMSOL® Multiphysics by Aalto University.

The model is based on the strong form differential equations (Eqs.(32)-(34)) for steady state heat transfer in a U-tube presented by Al-Khoury *et* al. (2005).

$$-\lambda_f \frac{d^2T_i}{dz^2} dV_i - \rho_f C_{p_f} \frac{\alpha u h}{2} \frac{d^2T_i}{dz^2} dV_i + \rho_f C_{p_f} u \frac{dT_i}{dz} dV_i + b_{ig}(T_i - T_g) dS_{ig} = 0 \qquad (32)$$

$$\lambda_f \frac{d^2T_o}{dz^2} dV_o - \rho_r c_r \frac{\alpha u h}{2} \frac{d^2T_o}{dz^2} dV_o - \rho_r c_r u \frac{dT_o}{dz} dV_o + b_{og}(T_o - T_g) dS_{og} = 0 \qquad (33)$$

$$-\lambda_g \frac{d^2T_g}{dz^2} dV_g - \lambda_g \left(\frac{\mathrm{d}T_g}{\mathrm{d}z} n_z\right) dS_g - b_{ig}(T_g - T_i) dS_{ig} + b_{og}(T_g - T_o) dS_{og} = 0 \qquad (34)$$

where ρ_f and $C_{p(f)}$ are the density and heat capacity of the carrier fluid. T_i, T_o and T_g are the temperatures measured at the inlet and outöet points, and at the grout, respectively. The characteristic leght of the pipe elements is represented by h, α is the rocks thermal diffusivity, λ_f and λ_g are the thermal conductivity of the fluid and grout, respectively, and b_{ig} and b_{og} are the reciprocals of the thermal resistance between the pipes and grout. Finally, S_{ig}, S_{ig} and S_g, denote the circunference of contact between inlet and oulet pipes and grout, and the circunference of grout, respectively.

A complete description of the implementation of this approach is explained by Janiszewski *et,* al. (2017), where the results of different scenarios of multi BHEs fields are included.

The strong form equations are converted into a set of weak form equations (Eqs. (35)-(37)) multiplying by a test function N^T, integrating by parts, and using certain boundary conditions.

$$\int_{V_i} \lambda_f \frac{dN^T}{dz}\frac{dT_i}{dz}dV_i + \int_{V_i} \rho_f C_{p_f} u\left(\frac{\alpha h}{2}\frac{dN^T}{dz} + N^T\right)\frac{dT_i}{dz}dV_i + \int_{S_{ig}} b_{ig}N^T(T_i - T_g)dS_{ig} = 0 \qquad (35)$$

$$\int_{V_o} \lambda_f \frac{dN^T}{dz}\frac{dT_o}{dz}dV_o + \int_{V_o} \rho_f C_{p_f} u\left(-\frac{\alpha h}{2}\frac{dN^T}{dz} + N^T\right)\frac{dT_o}{dz}dV_o + \int_{S_{og}} b_{og}N^T(T_o - T_g)dS_{og} = 0 \qquad (36)$$

$$\int_{V_g} \lambda_g \frac{dN^T}{dz}\frac{dT_g}{dz}dV_g - \int_{S_g} b_{sg}N^T(T_g - T_s)dS_g - \int_{S_{ig}} b_{ig}N^T(T_g - T_i)dS_{ig} - \int_{S_{og}} b_{og}N^T(T_g - T_o)dS_{og} = 0 \qquad (37)$$

where b_{sg} is the reciprocal of the thermal resistance between the grout and the rock.

Figure 31 conceptualizes the weak form equations schematizing the BHE elements interaction.

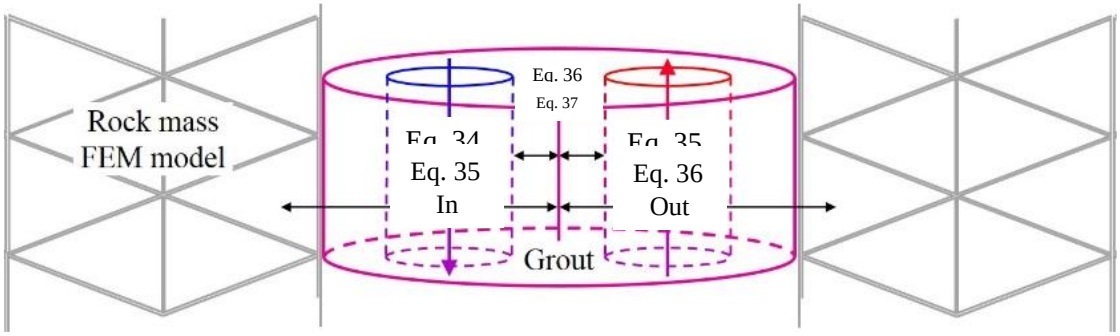

Figure 31. An illustrative example of the interactions of the implemented heat transfer equations, modified after Janiszewski et. al (2017).

Eq. (35) and (36) represent the thermal flow in the in- and outlet pipes. Eq.(37) is the interaction of the grout with both flow directions, and the ground.

The reciprocals of thermal resistance factor can be obtained by analogy with the Fourier and Ohm's laws for heat flow and current flow, as previously stated. The reciprocals between pipe elements and grout are equal and are calculated using Eq.(38).

$$b_{ig} = b_{og} = \frac{1}{R_{conv} + R_p} = \frac{1}{\frac{1}{h_{conv} \cdot \left(\frac{r_o}{r_i}\right)} + \frac{r_o \cdot ln\left(\frac{r_o}{r_i}\right)}{\lambda_p}} \tag{38}$$

with r_o and r_i as the outer and inner radii of the pipes, respectively; and λ_p as the pipe's material thermal conductivity. Nevertheless, the previous equation is only a simplification for the calculation of such resistive values which are dependent of the BHE configuration, the *in situ* ground properties and the filling material used. Al-Khoury *et* al. (2005) suggest the determination of this value via experimentation.

The convective heat transfer coefficient h_{conv} assuming turbulent flow conditions inside the pipe and is calculated using Eq. (39),

$$h_{conv} = \frac{Nu \cdot \lambda_r}{2 \cdot r_i} = \frac{(0.023 \cdot Re^{0.8} \cdot Pr^{0.4}) \cdot \lambda_r}{2 \cdot r_i} = \frac{\left(0.023 \cdot \left(\frac{u \cdot 2 \cdot r_i}{\nu_r}\right)^{0.8} \cdot \left(\frac{\rho_r \nu_r c_r}{\lambda_r}\right)^{0.4}\right) \cdot \lambda_r}{2 \cdot r_i} \tag{39}$$

where u is the fluid flow velocity, and ν_f is the fluid kinematic viscosity.

The reciprocal of the thermal resistance between the grout and surrounding rock is calculated using Eq. (40),

$$b_{sg} = \frac{1}{2 \cdot (R_{conv} + R_p) + R_g} = \frac{1}{2 \cdot \left(\frac{1}{h_{conv} \cdot \left(\frac{r_o}{r_i}\right)} + \frac{r_o \cdot ln\left(\frac{r_o}{r_i}\right)}{\lambda_p}\right) + \frac{r_g \cdot ln\left(\frac{r_{eq}}{r_g}\right)}{\lambda_g}} \tag{40}$$

where r_g is the grout, or in this case, the borehole radius, and r_{eq} is the equivalent pipe radius, Eq. (41), found by creating an equivalent area equal to the sum of the area of both pipes.

$$r_{eq} = \sqrt{r_i^2 + r_o^2} \tag{41}$$

The set of weak equations are implemented into the software's interface as linear elements more than 3 dimensional.

4.2 Heat transfer in pipes

The Heat Transfer in Pipes (HTiP) model, on the other hand, is a built-in module of COMSOL® Multiphysics (2017), in which the physics interface solves the energy balance for 1D pipe elements. Heat transfer from fluid to pipe wall, followed by heat transfer in solids describe the thermal flow between domains.

The model is coarsely summarized as a 3D domain representing the grout within which two 1D elements represent the pipes. The inside pipes flow is assumed to be fully developed, represented as an average flow velocity and used as input in the heat flow calculation.

Janiszewski *et* al. (2017) describe the interaction of heat transfer in pipes as follows,

$$AC_p\frac{\partial T}{\partial t} + \rho AC_p u \cdot \nabla T = \nabla \cdot A\lambda\nabla T + f_D\frac{\rho A}{2d_h}|u|^3 + Q + Q_{wall} \qquad (42)$$

where ρ, C_p and λ are fluid parameters, and u is the tangential fluid velocity. The cross-sectional area inside the pipe is represented with A, for an inner pipe or hydraulic diameter d_h for circular pipes, and f_D is the flow resistance friction factor according to Churchill friction model. Q is the heat source at a given temperature and Q_{wall} is the heat transferred through the pipe wall calculated with the Eq. (43).

$$Q_{wall} = (hZ)_{eff}(T_{ext} - T) \qquad (43)$$

The heat transfer through the pipe wall depends on the temperature difference, and the effective heat transfer coefficient $(hZ)_{eff}$ is calculated as

$$(hZ)_{eff} = \frac{2\pi}{\frac{1}{r_o h_{int}} + \frac{\ln\left(\frac{r_o}{r_i}\right)}{\lambda_p}} \qquad (44)$$

with r_o and r_i as the pipe's outer and inner radii, respectively. The internal film heat transfer coefficient h_{int} calculated as

$$h_{int} = Nu\frac{k}{d_h} \tag{45}$$

The heat flow between the in-pipe fluid and the grout is achieved by coupling the *heat flow through the pipe wall* to the *heat transfer in solid*, where Q_{wall} becomes the heat source in the solid.

The transient heat conduction in grout and rock is calculated as

$$\rho C_p \frac{\partial T}{\partial t} + \nabla \cdot -\lambda \nabla T = Q \tag{46}$$

where the material properties ρ, C_p and λ are those of the rock and the grout depending on the domain calculated, and Q are heat sources and sinks.

As an addition to the models, and to take account of the temperature variation at the surfaces of the investigated site (i.e. ground surface and tunnel walls), in both models the temperatures of the involved surfaces are prescribed as a boundary conditions, modelled with the *sinusoidal surface temperature* variation given by Carslaw & Jaeger (1959).

The temperature fluctuates with time according to the annual ground's surface temperature change, and attenuates with depth according to the thermal diffusivity of the ground. The temperatures at depth are calculated as

$$T(z,t) = T_{z,0} + \Delta T_{z,0} e^{-z\cdot\sqrt{\frac{\pi}{P\alpha}}} \cdot \cos\left(\frac{2\pi t}{P} - z \cdot \sqrt{\frac{\pi}{P\alpha}}\right) \tag{47}$$

where $T(z,t)$ is the ground temperature at depth z (from the ground surface) and time t. $T_{z,0}$ is the annual mean ground's surface temperature calculated from the annual mean surface air temperature through the relationship,

$$T_{z,0} = 0.71 \cdot T_A + 2.93 \tag{48}$$

proposed by Kukkonen (1986) to account for the temperature differences of ground and air due to snow cover, and specifically for the case of the high latitude countries. The $\Delta T_{z,0}$is the amplitude of annual ground surface temperatures, and P is the period equal to one year (given in seconds).

The air in the tunnel is heating up the surrounding rock, and the process is modelled as a heat convection. The convective boundary condition is used in the pre-heating step of the model to account for the increase in the temperature of the exposed rock surface since the construction of the tunnel, in this case five years.

The heat flux through the tunnel walls is modelled using

$$q_0 = h_{air}(L, p_A, T_{ext}) \cdot (T_{ext} - T) \tag{49}$$

where the q_0 is the heat flux through tunnel surfaces, and h_{air} is the convenction coefficient dependant on the dimensions of the tunnel surface, air pressure (assumed 1 atm) and the tunnel air temperature T_{ext}. Additionally, a constant geothermal heat flux is prescribed on the bottom surface of the model.

Following this first approach, a case scenario for the *in situ* experiment with the *HTiP* model was simulated following the original experiment length, with heating and cooling periods of 45 days each. The results of this simulation are presented in the conference paper *Numerical prediction for underground thermal energy storage in the Otaniemi Research Tunnel* (Janiszewski *et* al., 2017) presented at the 3rd Nordic Rock Mechanics Symposium held in Helsinki, Finland in October 2017.

5 Results

5.1 Heat flow and storage

The experiment ran 21 days in the heating phase and 15 days in the cooling phase, for a total of 36 days, an extra day from the previous thought time of 20/15 days, and shortened from the originally planned 45/45 days scenario.

The data obtained from the experimentation and the monitoring process is shown in this section followed by the results obtained from the numerical modeling. Three different scenarios were simulated by the two numerical models. Scenario B corresponds to the performed experiment length, while Scenario C represents to the originally planned experiment time.

A comparison between the observed and the simulated data for Scenario B is made at the end of the section.

5.1.1 Monitoring results

Different parameters were monitored during the progress of the experiment,

- the flow rate of the carrier fluid, through a flow meter with pulse meter to take account of the liters per hour.
- the carrier fluid temperature (inlet and outlet), through the thermal sensors installed in the inlet and outlet of the U-pipe.
- the temperature in monitoring borehole (MOBH), measured at opposing points of its circumference with the thermal multi-sensor thermal probes (P3 & P4).
- and the tunnel temperature.

Temperature in MOBH

The variation in the temperature along the MOBH was tracked with the multi-sensor thermal probes 3 and 4 (P3 & P4). As mentioned in chapter 3, the probes were installed at opposite sides of the borehole, leaving P3 in direct contact with the heated rock, and P4 touching the wall opposing the heated rock after a 3.7 cm air gap (Figure 22).

The gap influence on the rock temperature can be identified in the slight variation between the readings of both probes. This variation is also the result of the distance in between probe 4 and the heat source. Nevertheless, the distance is so short, that the discontinuity in the rock mass (gap) accounts for a better explanation for the readings variation between probes.

Temperature after phases

The resulting curves from the monitored data, Figure 32 to 34, show the same behavior and almost identical values between Probes 3 and 4. A slight variation is seen between curves, ranging from *0.118 to 0.396°C* at the peak of the heating phase, and *0.022 to 0.154°C* at the end of the cooling phase, depending on the sensor position inside MOBH.

For the heating phase, the trend is constant along the experiment, as it can be identified in Figure 32. The shape of the curve corresponds to the boundary conditions of the BHE. Being the wall in contact with the tunnel air, heat will escape to the air at a lower temperature; hence, the sensors closer to the wall will record an overall lower temperature than those "outside" the surface air influence.

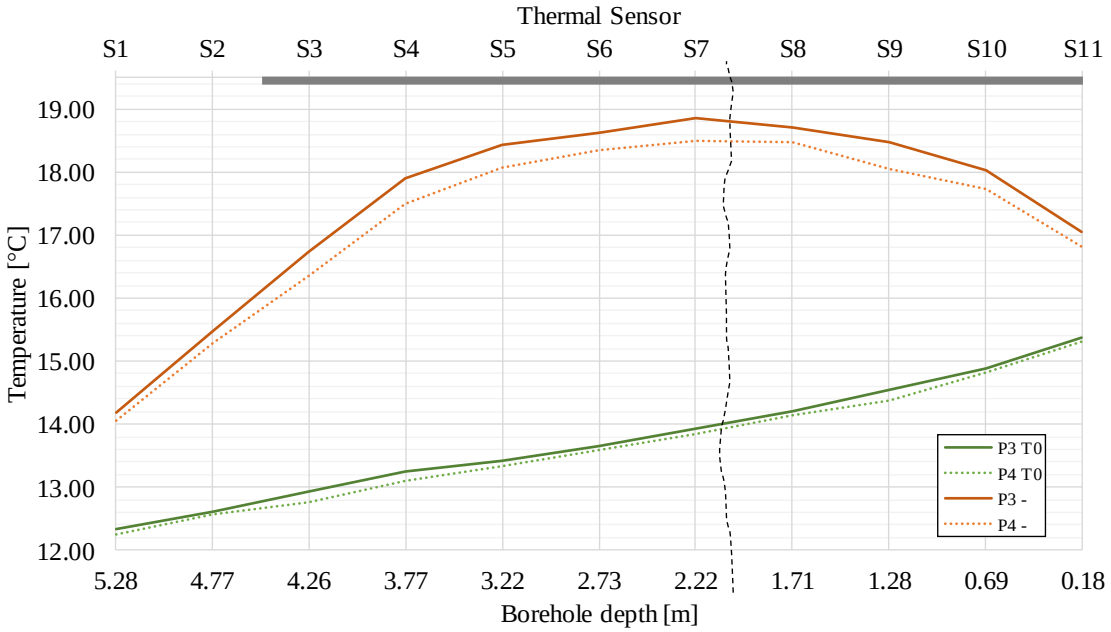

Figure 32. Temperature profile in MOBH after heating phase. P3 and P4 refer to the temperature readings in each probe at the end of the monitored period. T0 is the initial time (T=0). The dashed line represents the probable fracture present in the monitoring borehole. The gray scale (upper section) represents the length of the loop in the BHE.

An additional factor to the air-contact boundary is the presence of possible fractures crossing the boreholes. Two main fractures were identified in the boreholes during the video survey, one for each borehole. The fractures are located between 2.5 – 3.2 m of depth for the experiment borehole (EXBH), and between 1.71 – 2.22 m for MOBH. The possible fracture zone in the MOBH is represented by a dashed line between at the mentioned depth in the figures of the monitored data during the different experiment phases.

By analyzing the observed temperature profiles at the monitoring point for both phases, the location of the crack in the MOBH seems to have an influence in the thermal flow, at least at the sensors. The drop in the temperature profile for the sensors located just before the *2.00 m* mark can be a combination of such discontinuity and the effect of the surface air temperature. Nevertheless, this assumption cannot be taken as a fact since is difficult to assess it without knowing the orientation of the crack for which a geological mapping and geophysics methods are required and out of the scope of this project.

Interestingly, the fracture observed in the EXBH seems not to affect the thermal flow towards the MOBH, since no alteration in the temperature profile is seen in the latter for the location of the crack crossing the BHE. The orientation of the fracture could have inference on this effect, as it runs diagonally to the borehole axis into the rock mass and in direction of the MOBH, possibly affecting the heat flow at the toe area in the MOBH. Additionally, the grout filling also increases the continuity in the medium by filling gaps. Finally, the vertical arrangement of the BHE loop provides symmetry to the heat transfer process by having half of the BHE and its elements transferring energy to the monitoring point.

Opposite to the BHE's collar, the toe has no physical boundary with the rest of the rock mass. Here, the thermal conductivity of the ground determines the amount and rate of heat migrating to the rest of the rock mass.

In MOBH, a bigger difference between the readings at the first sensor in the toe (S1) and the third sensor inline (S3) can be seen compared to the rest of the hole. This effect can be a consequence of the BHE's loop length of 4.5 m (represented by the gray square in the figures), ending between the thermal probes' sensors 2 and 3.

Notwithstanding with the previous figure, the slight difference in values recorded is not clearly identified in case of the cooling phase curves for the different thermal probes (Figure 33). The explanation could lay in the fact that P4 stopped working 5 days before the end of the experiment, not recording the variation in the temperature for the last days.

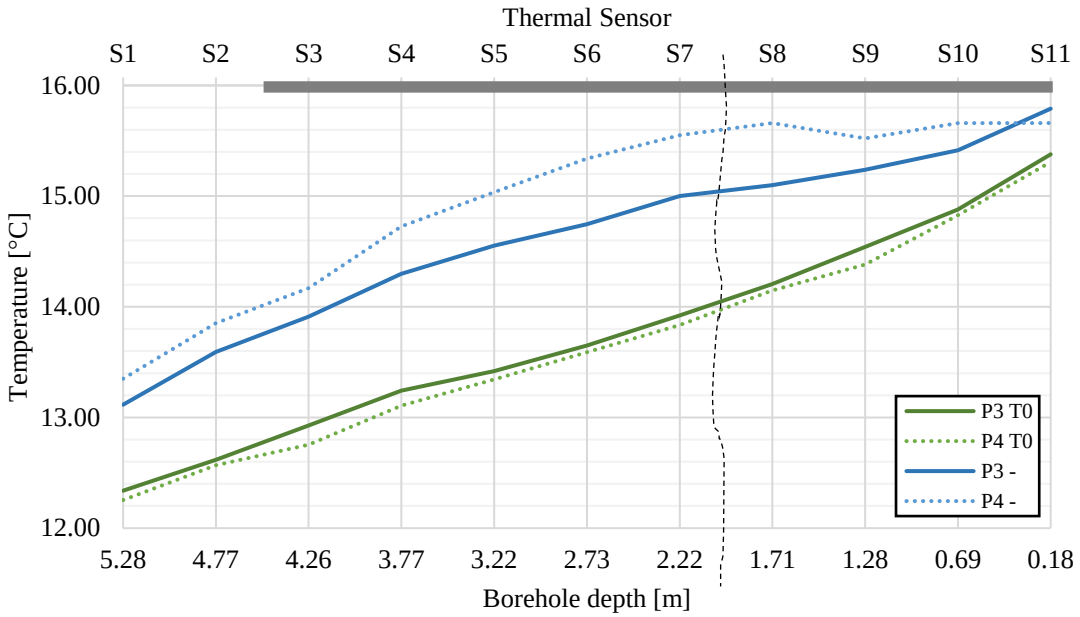

Figure 33. Temperature profile in MOBH after cooling phase. P3 and P4 refer to the temperature readings in each probe at the end of the monitored period. T0 is the initial time (T=0). The dashed line represents the probable fracture present in the monitoring borehole. The gray scale (upper section) represents the length of the loop in the BHE.

A numerical fitting was done with help of MS Excel® fitting the cooling curve and obtain the missing data. After the fitting shown in Figure 34, is possible to appraise the curves for both probes are closer in value than the curves after the heating phase. However, a slightly higher value in the middle sensors for P4 can be identified, most probably by overestimation of the missing data.

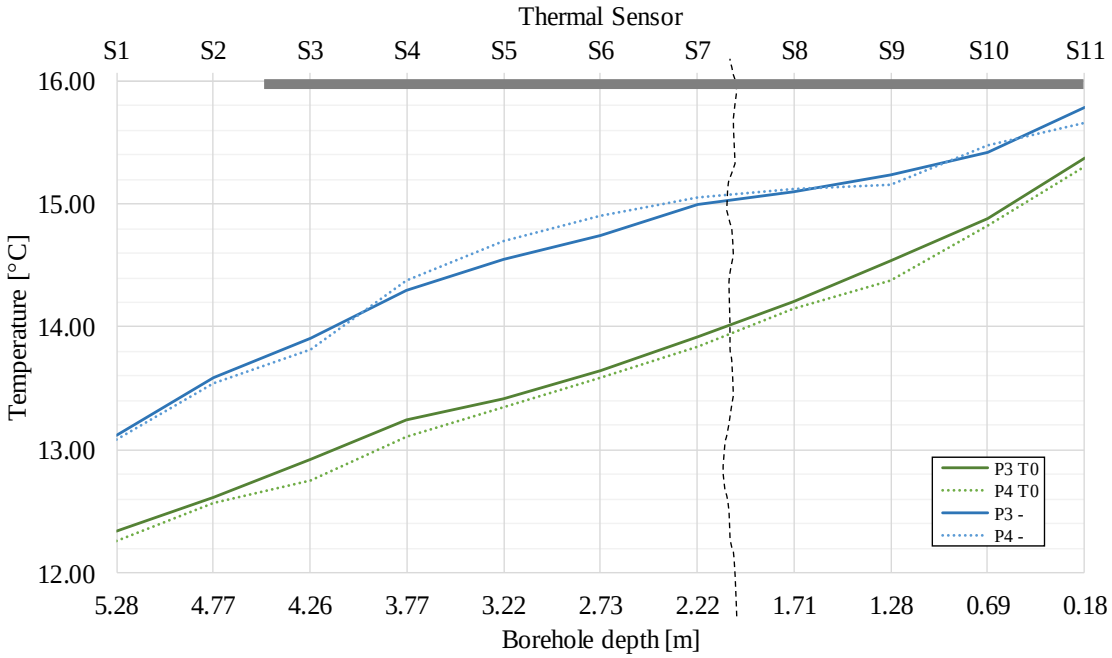

Figure 34. Temperature profile in MOBH after cooling phase (fitted). P3 and P4 refer to the temperature readings in each probe at the end of the monitored period.

Stored thermal energy (Temperature gained)

With the observed data, the difference in temperature gained at the end of the different phases was calculated, providing an idea of the amount of stored thermal energy in the rock. This analysis is useful when designing the seasonal storage by identifying the point where higher amount of energy is transferred to the reservoir. When having an array of boreholes, this could also help to increase the efficiency of the energy utilization by sectoring the depth from where heat is retrieved.

The gain in temperature after the heating phase is evaluated at the different sensor locations inside the MOBH with both probes and plotted in Figure 35. The stored thermal energy represents the difference between the temperature at the end of the heating phase and the rock temperature prior to heating.

Analyzing the figure, the area in the monitoring point with the highest increment in temperature is located between 2.0 and 3.5 m of depth, accounting for 20% of the monitoring borehole length, and localized in the in the center of it, approximately. The highest temperature difference in the temperature is found in sensor 5 (S5) for the Probe 3 with a temperature increment of *5.07°C*, and in S4 in the case of Probe 4 with *4.755*°C from the initial value.

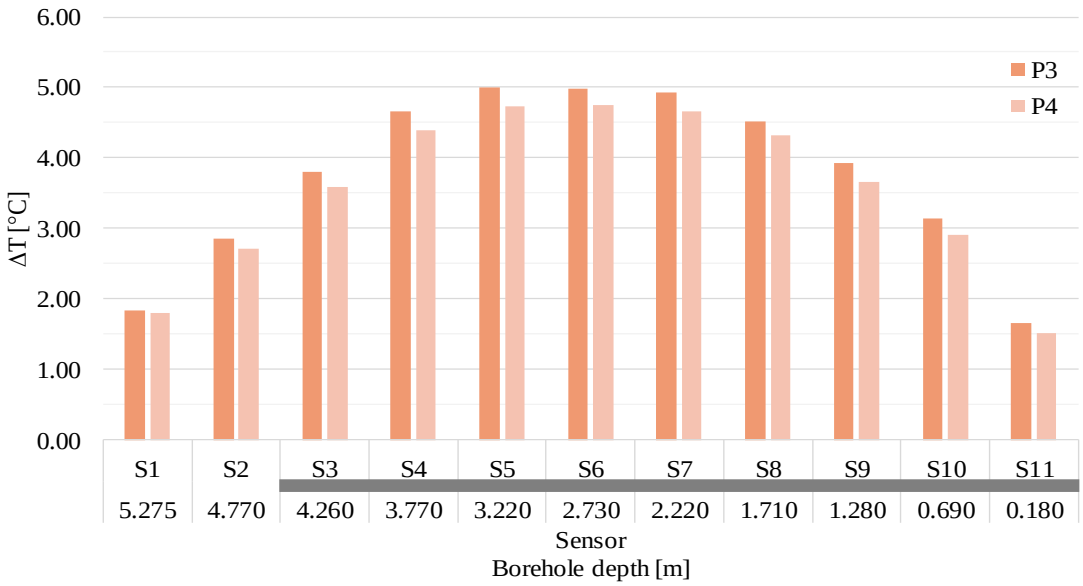

Figure 35. Measured temperature gain at MOBH for each sensor on thermal probes 3 and 4 after the heating phase. The gray scale (lower section) represents the length of the BHE loop.

It can be inferred from the figure that by adding a thermal insulation on the surface of the tunnel wall the heat loss near the surface could be reduced, increasing considerably more than 20% of the BHE length and therefore, the rock volume under its influence.

Making a comparison between the lengths of both boreholes, MOBH and BHE, the area with the highest temperature gain corresponds to the third quarter of the BHE length starting from the collar, accounting for a 22% of the U-pipe.

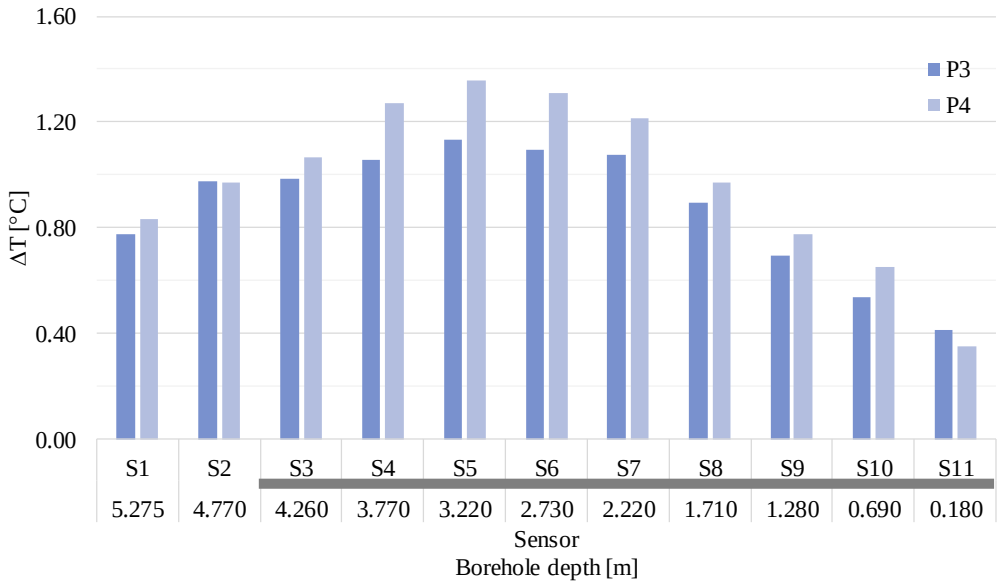

Figure 36. Measured temperature gain at MOBH (after the fitted values) for each sensor on thermal probes 3 and 4 after the cooling phase. The gray scale (lower section) represents the length of the BHE loop.

The maximum gain in the temperature after the cooling phase is in S5 with an increment value of *1.132°C* and *1.356°C* for P3 and P4, respectively. Contrasting with the previous figure, the highest net increment in the temperature of the rock recorded by the sensors is found in P4. This seems opposite to the profile obtained after the heating period where the highest temperature was in P3, closer to the heat source.

Carrier fluid temperature

The carrier fluid temperature was maintained constant during the 21 days that the heating phase lasted, with a goal temperature of *50°C* set after the capabilities of the heater and operational fluid temperature for the circulation pump. A power controller installed in the heater was set to regulate the input temperature. Nonetheless, the temperature achieved during the heating phase was higher with an average value of *57.277°C* at the intake. The temperature was kept overall constant during the 21 days period with slight variations as seen in Figure 37.

On the other end of the loop, the thermal sensor at the outlet recorded a similar behavior for the carrier fluid leaving the loop. The trend in the temperature at this point presents a bit higher differences than in the case of the inlet temperature measured; however, the temperature is also almost constant during the 21 days measured with an average value of *55.260°C*.

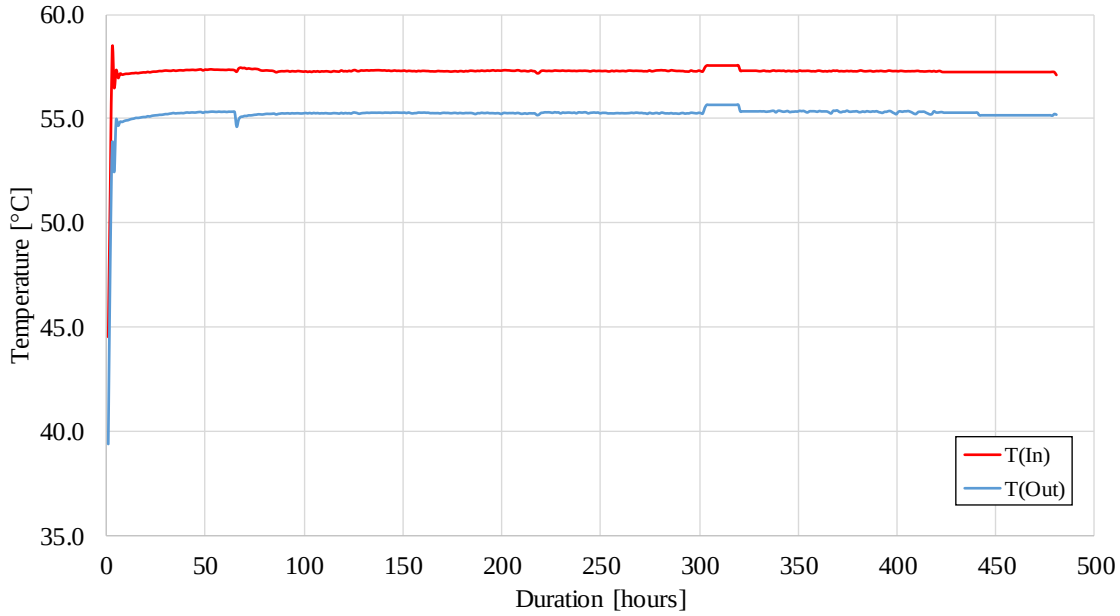

Figure 37. Measured carrier fluid input & output temperature during heating phase.

5.1.2 Modelling results

The resulting settings of the experimentation process are taken as simulation settings for the numerical modelling with Comsol® Multiphysics.

The input parameters used in the modelling proceed from different sources. The ground's thermal parameters λ_s and α_s are taken from the laboratory results, while the C_p is calculated from the tested parameters. In contrast, the grout thermal properties and the carrier fluid (water) are taken from literature (The engineering toolbox 2017) for the *WFE model*, while *HTiP model* utilizes the built-in properties from the software's material library.

Besides materials properties, the software requires a value for flow rate and input temperature, taken from the mean hourly values obtained from the experiment and the monitoring process.

The experiment duration varied from the originally planned 45 days per phase length due time and operational constrains. Different scenarios were designed to account for the impact the shortening of the phases could have over the experiment for heat transfer. Based on the phase length, the scenarios are

Table 12. Phase lengths for simulation scenarios

Phase	Heating	Cooling
A	45 days	15 days
		45 days
B	21 days	15 days
C	15 days	15 days

From the three scenarios, Scenario B is later compared against the obtained data from monitoring process to determine which model has the closest results to the real case.

Due to the nature of the 3D environment of the FEM analysis software, the presence of discontinuities such as fractures or lithology change are not taken into consideration, unless the boundary is drawn in the model, modifying the nodes of the finite element mesh, not the case of this study. Additionally, the cross-sectional area of the simulated environment is oversimplified using simple geometrical elements; important factors when comparing results between simulation and observed data, especially at boundary conditions such as the wall surface.

As a first step, the models simulate the initial temperature in the ground according to the depth, and at each sensor location inside the MOBH. The determination of the initial values is achieved through the application of Eq. (47) for the variation in the annual ground surface temperature and fluctuating with depth. Considering the time the tunnel has been excavated, the period of evaluation for the pre-heating study was based in 5 years. The results of this first assessment are plotted in Figure 38.

Nevertheless, the models do not take into consideration the actual air temperature in the tunnel since its construction, factor that affects the distribution of the temperature in the rock mass. The resulting temperature is considered as the undisturbed ground temperature T_{S_0} for the simulated scenarios.

The plotted data shows the same trend and quasi-identical values for T_{S_0} differing slightly between each other as the depth increases.

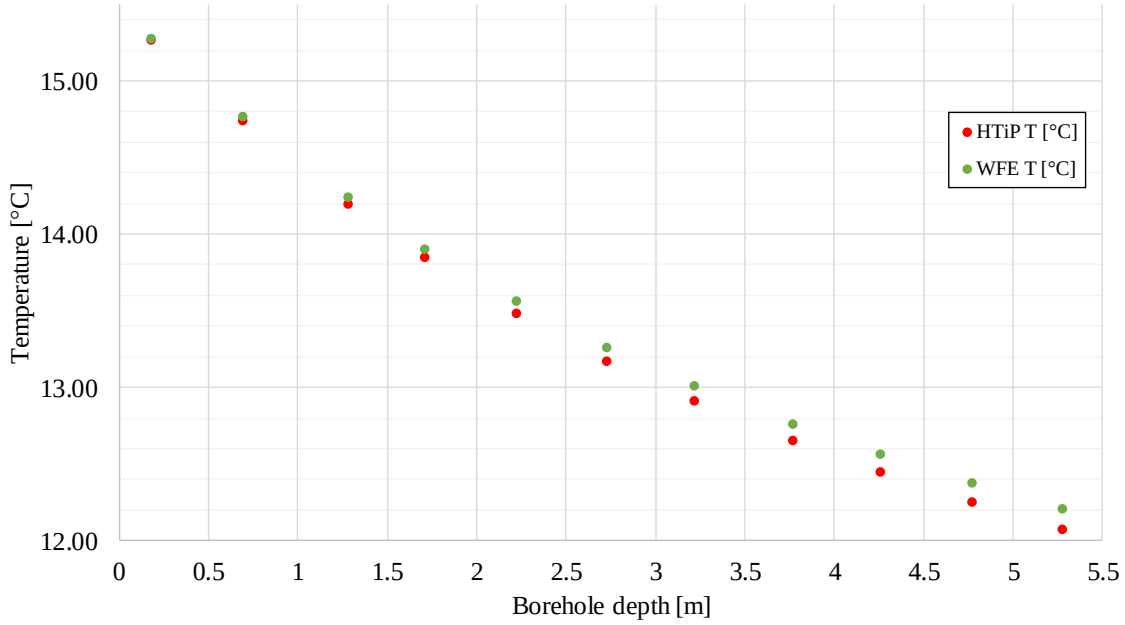

Figure 38. Initial or undisturbed ground temperature (T_{S_0}) fir the simulated sensor points inside MOBH for both models.

Posterior to the determination of the initial temperature, the simulation of the heating phase starts with an hourly time step. The evaluation in hours has a more results of the heat development over time. Subsequently, the cooling phase runs with a daily time step, as no additional accuracy is necessary. The results of both models for the three scenarios are plotted per phase and compared between them.

For the heating period simulation, Figure 39 plots the resulting temperature profiles read in the monitoring points in the different scenarios. Evidently, the highest temperature is obtained after the longest heating period, consistent with a higher amount of energy transferred. Interestingly, the highest temperature obtained from the *WFE model* (Scenario A) is lower than the middle value (Scenario B) for *HTiP*, while the initial temperature T_0 is practically the same for both, being even less for the latter model.

The profiles behavior for both models and the different scenarios is very similar, keeping the trend between models as well as the temperature difference. In all cases, the *HTiP model* always returns a higher value, with the exemption of the initial temperature. The *HTiP model* considers the entire grout volume in the BHE and its thermal capacity (C_{p_g}), besides the temperature depending variations in the thermodynamic properties of water, factors that could explain the higher simulated values. On the other hand, the *WFE model* accounts for the grout element only as part of the formula, not with the same weight as in *HTiP*, also the thermodynamic properties of water are set to *50°C*.

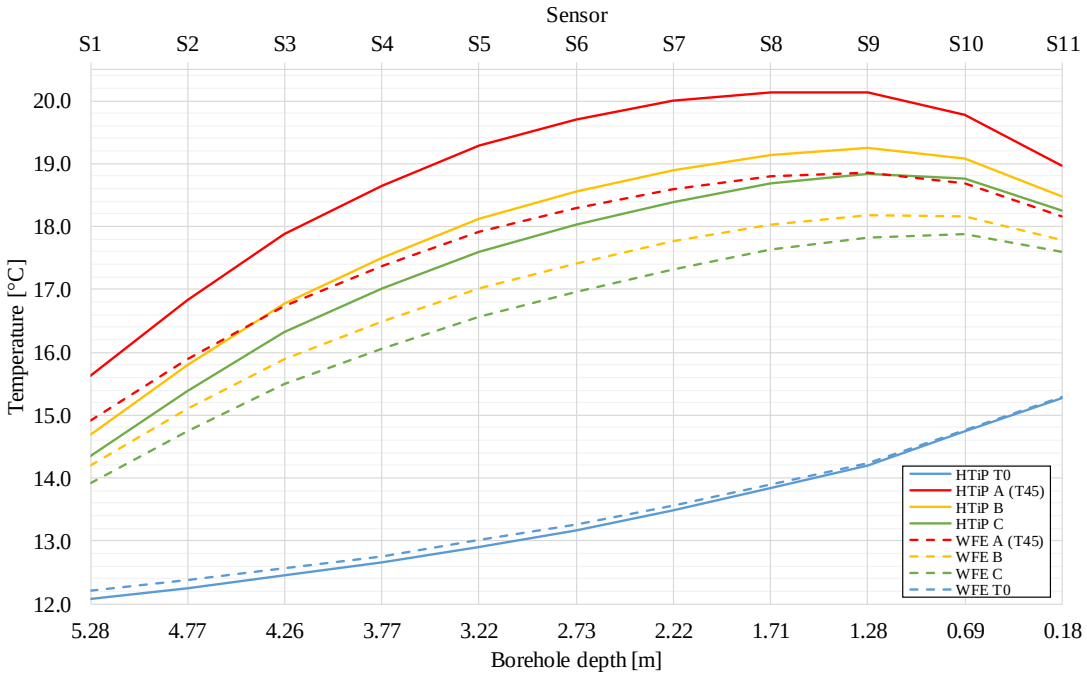

Figure 39. Models comparison. Temperature in MOBH after heating phase.

Figure 40 shows the temperature simulated for MOBH after the cooling period. Here, Scenario A presents for two cooling periods of 45 and 15 days, while Scenarios B and C show 15 days cooling period each. The figure shows how for 45 days of cooling in

Scenario A, for in both models, the temperature decreases beyond the final temperature for Scenario C, with a third of duration for both phases. In addition, by the end of the 45 days of cooling, both models show less difference in values than for the rest of the scenarios shown.

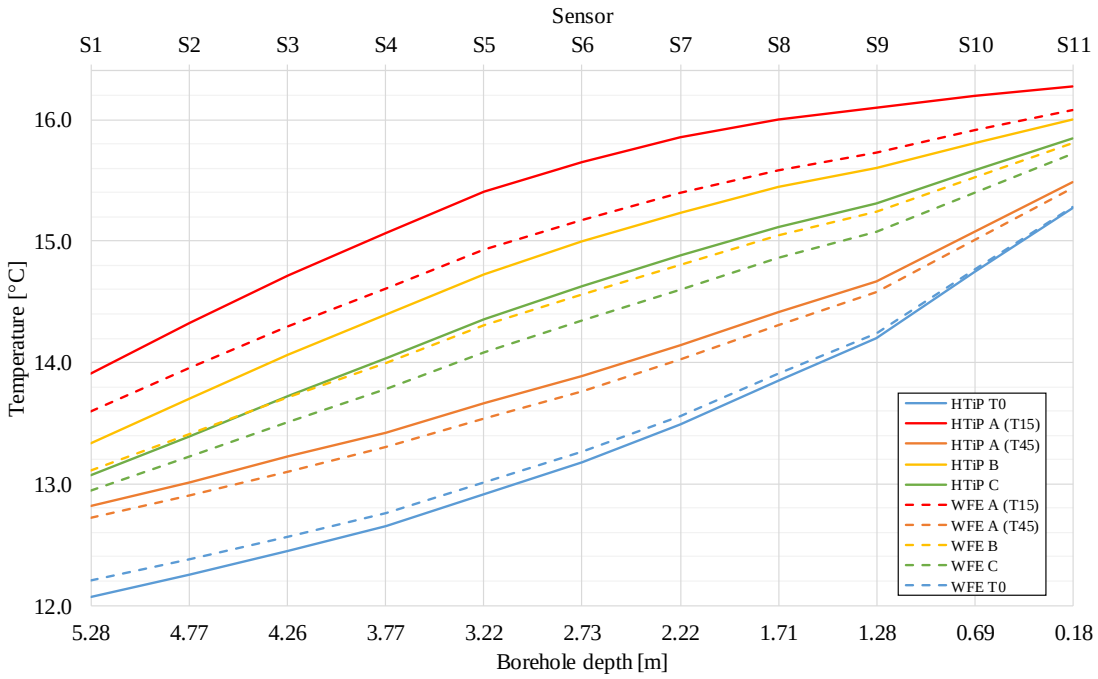

Figure 40. Models comparison. Temperature in MOBH after cooling phase.

Referring to the MOBH, the final temperature indicates how much energy was transferred from the source to the rest of the ground at this point, and the amount lost because of the different boundaries in the storage system. In the seasonal storage case, is important to consider the duration of the heating phase and when the energy retrieval would take place, as energy dissipates to the colder regions, making the process not as efficient as it could be if the retrieval starts too long after the heat injection has stopped.

To measure the variation in energy transferred after each phase, the increment in the temperature is evaluated at the simulated sensors inside MOBH, and presented in graphic form in Figure 41 &42. These figures illustrate the temperature gained by the end of the heating and cooling phases, respectively. From the images is seen, the higher amount of energy retrieved would occur when the heating phase is the longest and the cooling phase is reduced to the minimum, represented by the scenarios A for 45 days heating and 15 days of cooling.

Figure 41 compares the values of the biggest increment in temperature after heating phase for each simulated scenario for both models. The values are plotted together and contrasted against each other, showing the longest heating period in accordance to the initial temperature calculated by the models.

The highest value is obtained in the *HTiP model* – Scenario A with an average temperature increment in the sensors of *5.448°C*, and a maximum of *5.527°C* at S6 located in the center of the borehole (2.73 m).

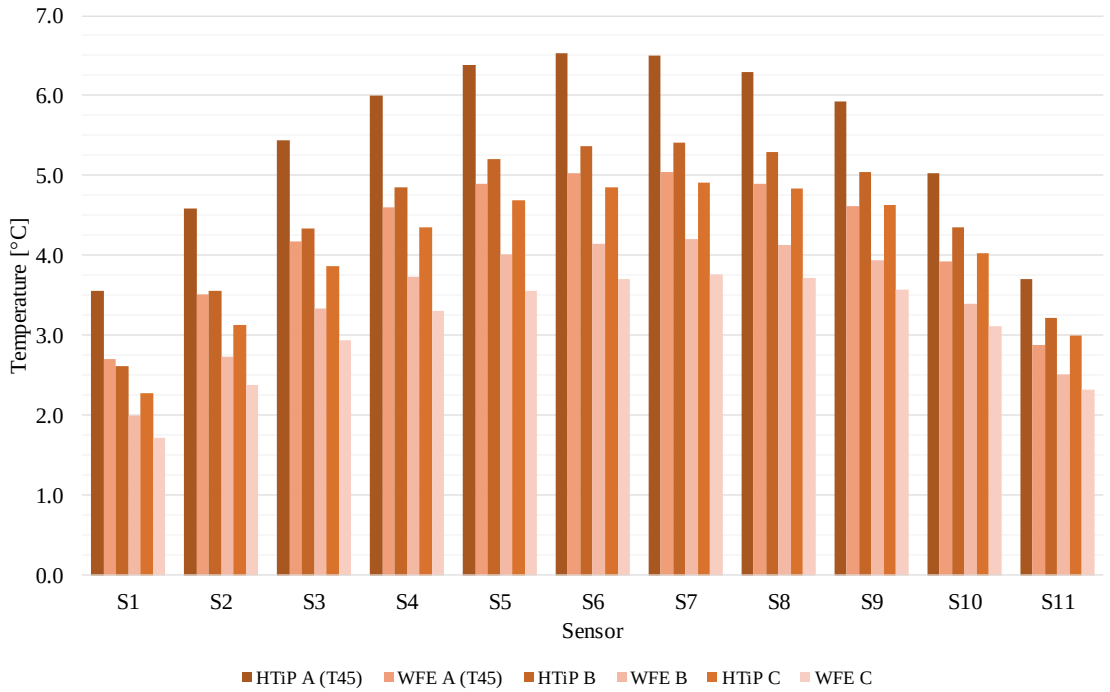

Figure 41. Models comparison. Temperature increment at each sensor in MOBH after heating period.

Likewise, Figure 42 presents the temperature gained after the cooling period. From the image is seen the highest increment occurs also in the *HTiP model* – Scenario A but for a cooling period of 15 days only, reaching a maximum increment of *2.491°C* recorded at S5. Contrastingly, the lowest value for after the cooling is obtained in the same Scenario for the *WFE model* for 45 days of cooling. The result is consistent with the previous results as the *HTiP model* returned the highest values in each scenario, and the effect the longer cooling period has on the dissipation of heat through the mentioned boundaries.

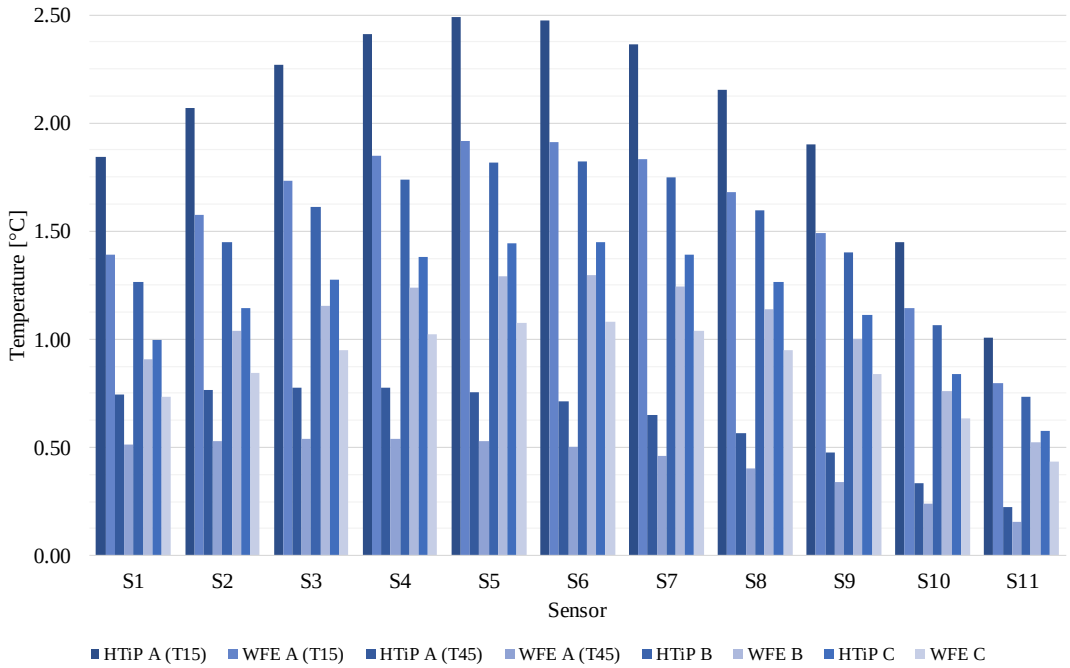

Figure 42. Models comparison. Temperature increment at each sensor in MOBH after cooling period.

The comparison becomes useful to decide the length of the different phases for a seasonal storage, by determining the optimal length based on operational costs and revenue, since the rock has a determined capacity after which increasing the length of heating the gain in temperature does not increase significantly. In the models, for example, the highest difference in temperature for extra 24 days of heating (Scenario A vs B) is *0.998°C* for HTiP (S8) and *0.678°C* for WFE (S9).

Temperature profile evolution

In addition, the evaluation of the temperature profile development in the borehole was done on a 5 days step for both models to account for the additional days of heating. Figure 43 & 44 show the simulated temperature profiles along the borehole for the *HTiP* and *WFE* models, respectively. In both cases, the difference between the obtained values tend to decrease as the heating period is increased, reaching a point where the increment or gain in temperature becomes practically imperceptible.

The figures also show that the *HTiP model* estimates higher values than the *WFE model* for the whole duration of the heating period, being an exemption the initial temperature of the rock, as previously discussed. The variation between models' values can be considered as significant as the highest temperature profile (45 days) for the *WFE model*

corresponds to fictional curve laying between the 15 and 20 days curves of the *HTiP model*. Withal, the difference in the hottest point at the end of the 45 days of heating for both models is only around 1.5°C as the temperature varies less and less with the increment of heating time.

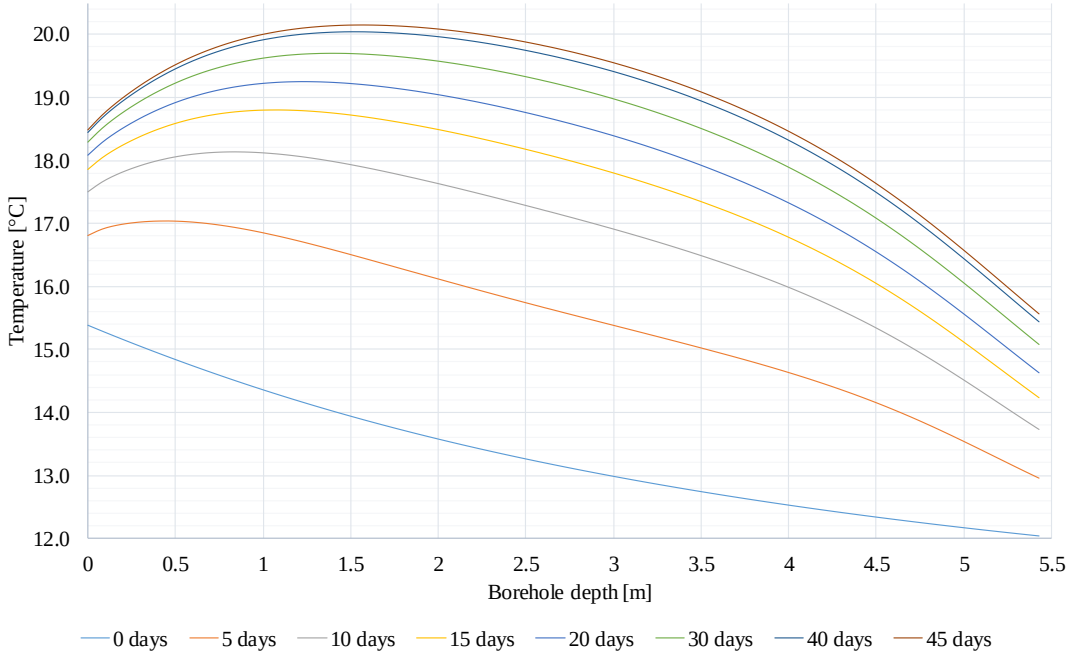

Figure 43. Temperature evolution along MOBH over 45 days heating period – HTiP model.

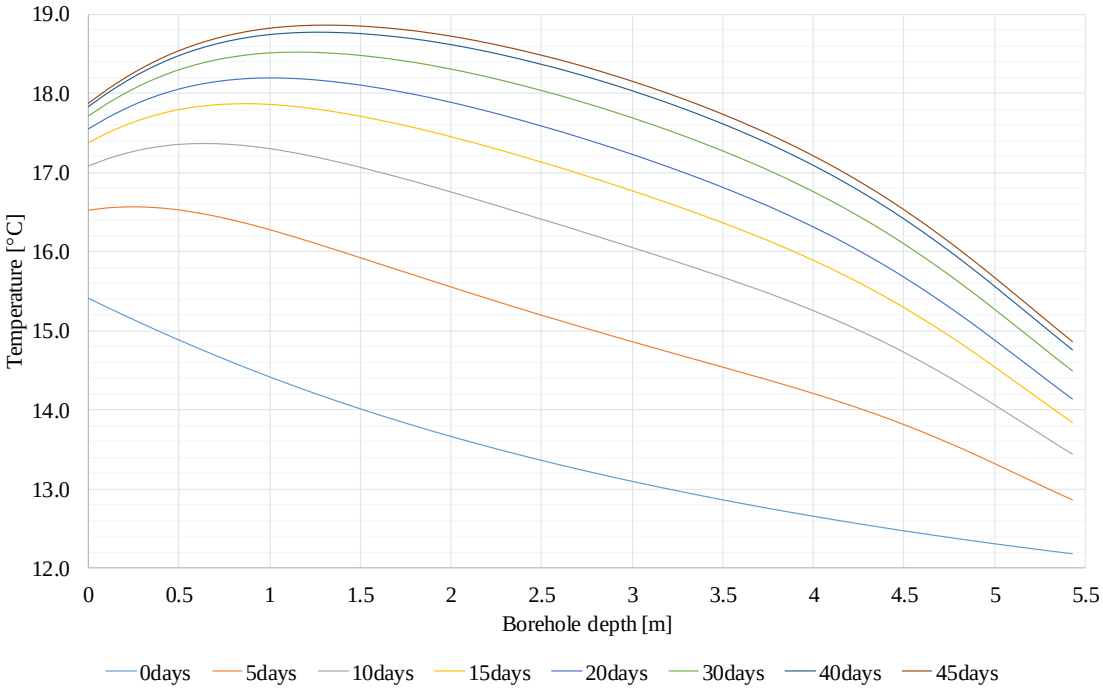

Figure 44. Temperature evolution along MOBH over 45 days heating period – WFE model.

2D isotherms representation

A thermal 2D visualization of the heat field around the BHE's was done with the tools of Comsol® Multiphysics for the different scenarios at the last day of each phase. The images show how the deviation of the borehole was taken in consideration for a better simulation process and results that are more reliable. A dashed line represents the location and deviation of the monitoring hole parallel to the BHE. The figures show the experiment site in its planar view, namely in the XY-direction. In the figures, the orientation is inversed though, having the MOBH to the right-hand side of the BHE when looking it from the wall surface.

The 2D representation of the heat field around the BHE provides graphic explanation for the obtained temperature profiles. Different isotherms cross the MOBH at different points showing a higher temperature in the central sensors than in the rest. Additionally, the effect of the boundary effect mentioned at the toe of the EXBH, i.e. the continuity of the rock, is shown. Since Scenario B is the one compare to the monitored data, only the images for it are shown.

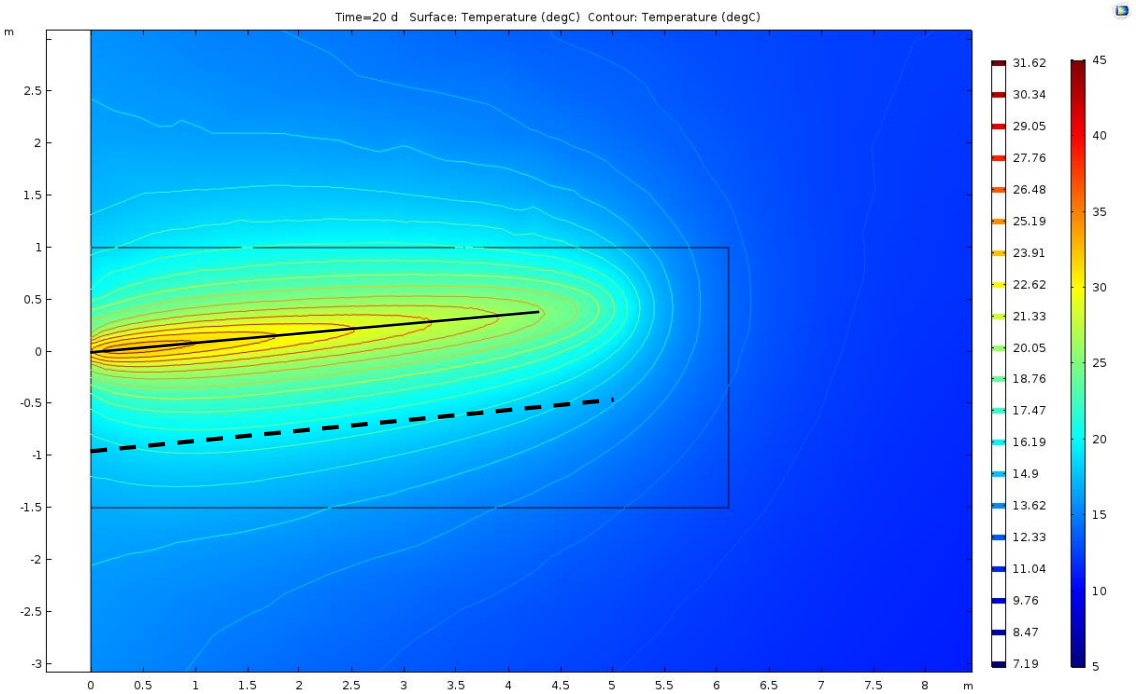

Figure 45. Heat field isotherms in the experiment site after heating – HTiP model. The solid black line represents the BHE length, the dashed line represents the MOBH.

Figure 45 & 46 show the achieved heat field in the rock mass after the heating period for the *HTiP* and *WFE* models, respectively. The isotherms show the extension of the BHE

influence by the end of the analyzed phase and the temperature achieved in the grout/rock medium, not in the carrier fluid. The length of the BHE exchanger is represented in the figures with a solid black line in $y = 0$. On the other hand, the MOBH is represented by a dashed line at $y \approx 1$.

The highest temperature is found in the first meter of depth of the BHE, where the temperature of the carrier fluid is the highest. As the fluid circulates the temperature in it decreases, transferring the lost heat to the ground and increasing the ground temperature as shown by the rainbow code. The reach of the isotherms in the ground will be result of the ground thermal properties. Heat will migrate to further zones in the ground faster and easier with a higher thermal conductivity value, increasing the extension of the heated field.

The variation between models for the hottest point of the BHE-ground system is approximately *3.9°C*, being the *HTiP* the one returning the highest value (*32.21°C*) after 21 days of heating. *WFE model* achieved a maximum temperature of *28.32°C*.

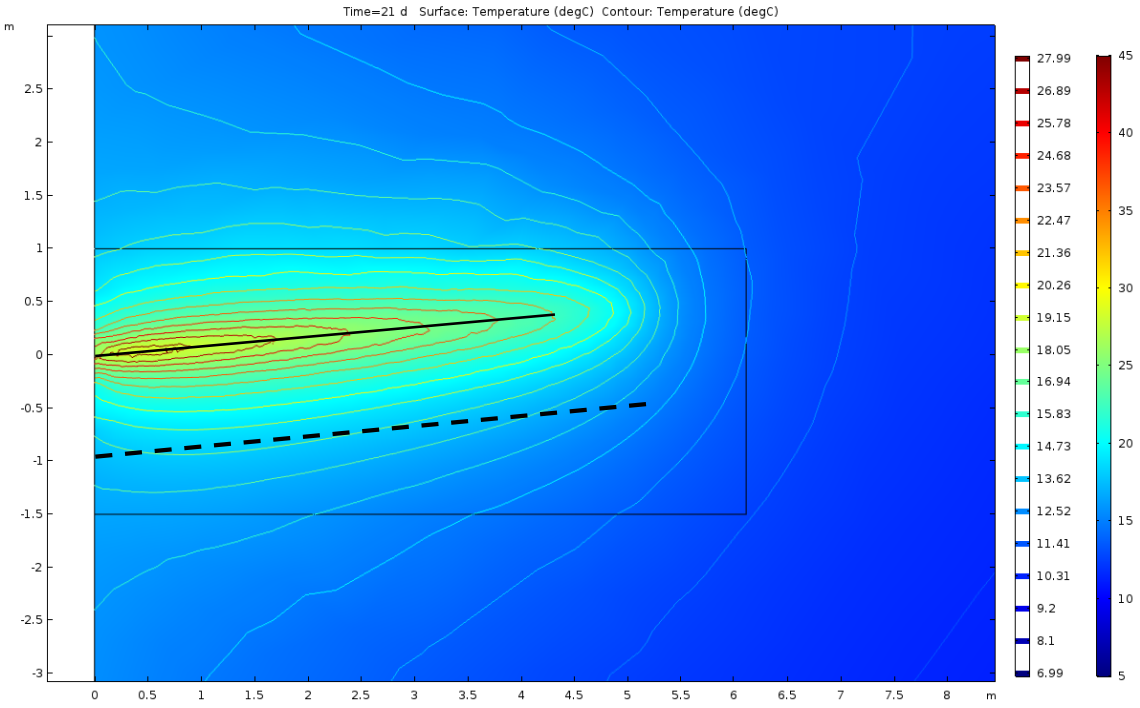

Figure 46. Heat field isotherms in the experiment site after heating – WFE model. The solid black line represents the BHE length, the dashed line represents the MOBH.

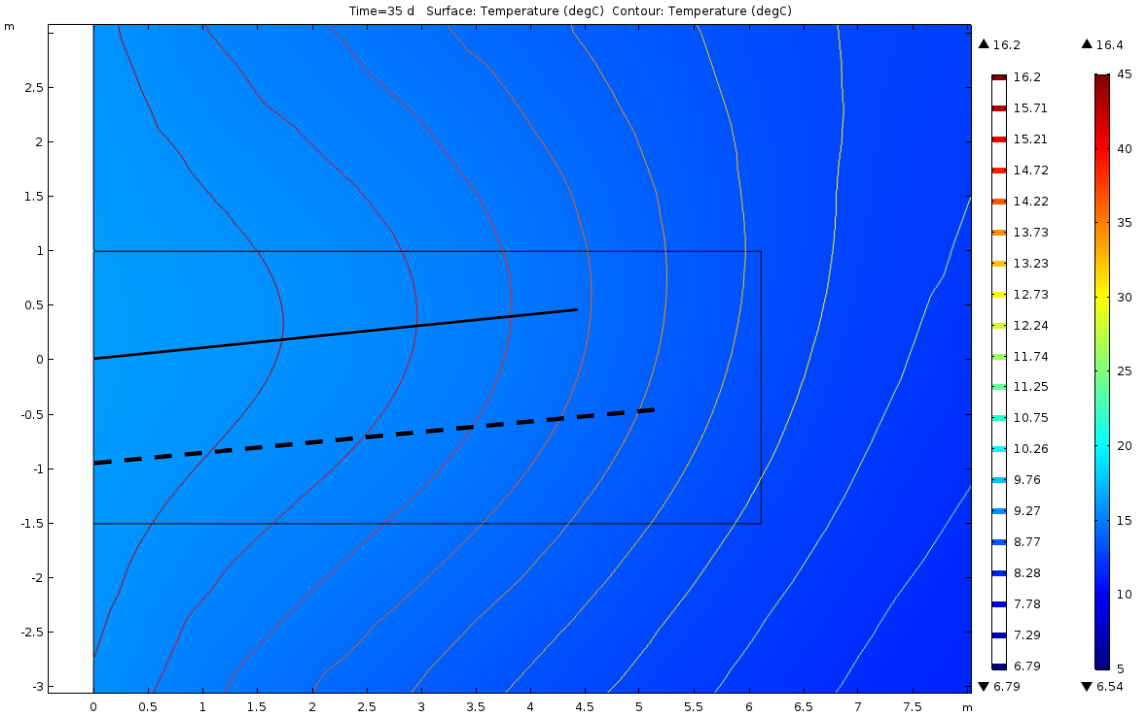

Figure 47. Heat field isotherms in the experiment site after cooling – HTiP model.

The temperature difference between models is smaller for the cooling phase, with a variation of *0.02°C* between models, a big contrast with the heating results. Figure 47 shows a maximum temperature in the ground of *15.71°C* for the *HTiP model*, while *15.69°C* is returned for the *WFE* case in Figure 48.

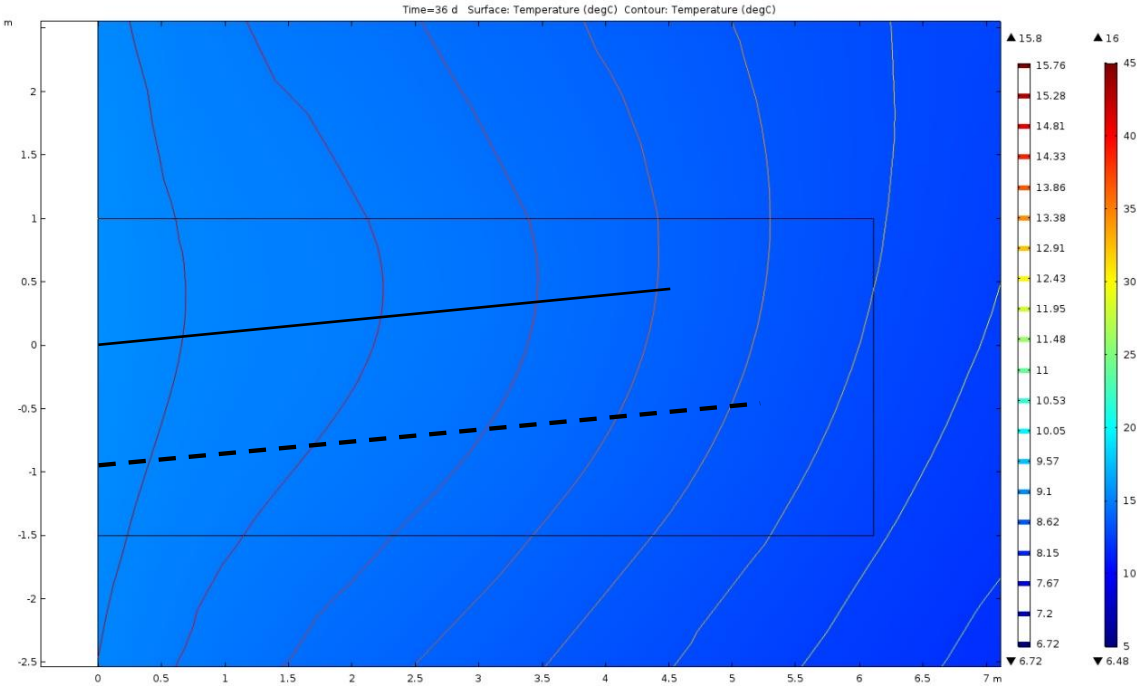

Figure 48. Heat field isotherms in the experiment site after cooling – WFE model.

The isotherms are attenuated with the increasing cooling steps, in other words, the hyperbolical behavior flattens towards a linear representation as the cooling period is increased.

Finally, Figure 49 illustrates the variation of the carrier fluid temperature in the loop and the temperature at the monitoring points, in- and outlet. An average temperature considered constant during the entire heating period was set as the input value. Subsequently, the models calculate heat transferred and the temperature in the outlet after the loop, depending on the thermal properties of the elements in the BHE and its configuration.

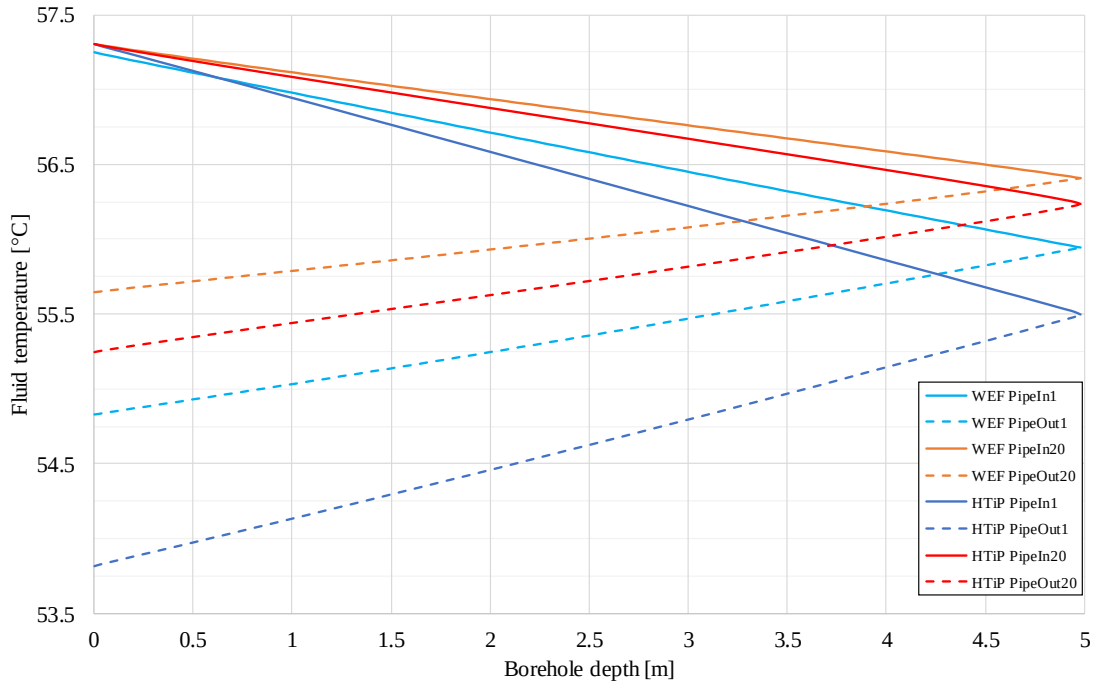

Figure 49. Scenario B simulated carrier fluid temperature at inlet and outlet of the BHE according to the models. PipeIn1 and PipeOut1 refers to the temperature entering and going out of the BHE by the end of day 1 of the heating phase, respectively. Same case for PipeIn/Out20 for the last day of heating phase.

The accurate simulation of T_I and T_O is a big advantage when designing a BHEs array. The definition of the input temperature will have an impact in the costs of operation by providing certain power input, making a project feasible or not.

5.1.3 Comparison observed vs. modelled data

The comparison against the observed data was performed the results of Scenario B, with the same characteristic experiment length of 21 days heating, 15 days cooling. The discrepancy between the results is taken into consideration to validate the results of the numerical models.

On a first approach, the models ran with an average value for flow rate and inlet temperature, values used in the scenarios comparison. The flow rate was recorded every 10 seconds, and the in- and outlet temperature every 30 seconds. The recorded values were averaged in hours; the mean values of all the heating hours were used as models input values. The average flow rate (q) was used by the models to calculate the fluid speed (u). Similarly, the average input temperature (T_I) was used by the model as carrier fluid temperature for the heat pulse.

On a second approach, the observed values during the heating were averaged per hour for q and T_I, and fed to the models as tables instead of a unique mean value. This approach intended to simulate the changes in the flow rate that would eventually determine the amount of heat transferred by affecting the power rate. The results of both approaches delivered very similar values with a variation of approximately *0.02°C* at the end of the heating phase compared to the first approach.

Undisturbed ground temperature

The first assessment was the evaluation of the preheating phase or determination of the undisturbed ground temperature T_{S_0}. The results of the preheating phase in the models are compared against the observed data for the baseline temperature described in Chapter 3. The values measured in MOBH were obtained through the monitoring of the rock temperature with Probe 3 for approximately 76 hours.

The temperature difference on a first assessment shows a maximum absolute variation of *0.238°C (1.64%)* for the *HTiP model*, and *0.262°C (1.81%)* for the *WFE model*, compared to the recorded values. Furthermore, the minimum absolute variations are *0.008 (0.06%)* and *0.012 (0.10%)*, respectively. Table 13 displays the difference in temperatures for each sensor in contrast with the observed initial rock temperature.

Table 13. Temperature variation for each model (Scenario B) with reference to the measured T_{S_0}

Sensor	Depth	Observed	HTiP		WFE	
	[m]	[°C]	ΔT [°C]	ΔT [-]	ΔT [°C]	ΔT [-]
S1	*5.275*	12.233	-0.161	-1.31 %	-0.028	-0.23 %
S2	*4.77*	12.394	-0.142	-1.14 %	-0.017	-0.14 %
S3	*4.26*	12.552	-0.104	-0.83 %	0.012	0.10 %
S4	*3.77*	12.741	-0.088	-0.69 %	0.020	0.16 %
S5	*3.22*	12.92	-0.008	-0.06 %	0.090	0.70 %
S6	*2.73*	13.331	-0.156	-1.17 %	-0.069	-0.52 %
S7	*2.22*	13.409	0.078	0.58 %	0.152	1.13 %
S8	*1.71*	13.724	0.124	0.90 %	0.182	1.32 %
S9	*1.28*	14.101	0.094	0.67 %	0.137	0.97 %
S10	*0.69*	14.505	0.238	1.64 %	0.262	1.81 %
S11	*0.18*	15.176	0.090	0.59 %	0.103	0.68 %

Furthermore, Figure 50 contrasts graphically the observed data against the temperature values simulated by preheating equations in the models prior to the circulation of the heated carrier fluid. In the graph is observable the same trend for the three cases, showing a high degree of accuracy and precision. The corresponding comparison was made for the data at the end of each phase.

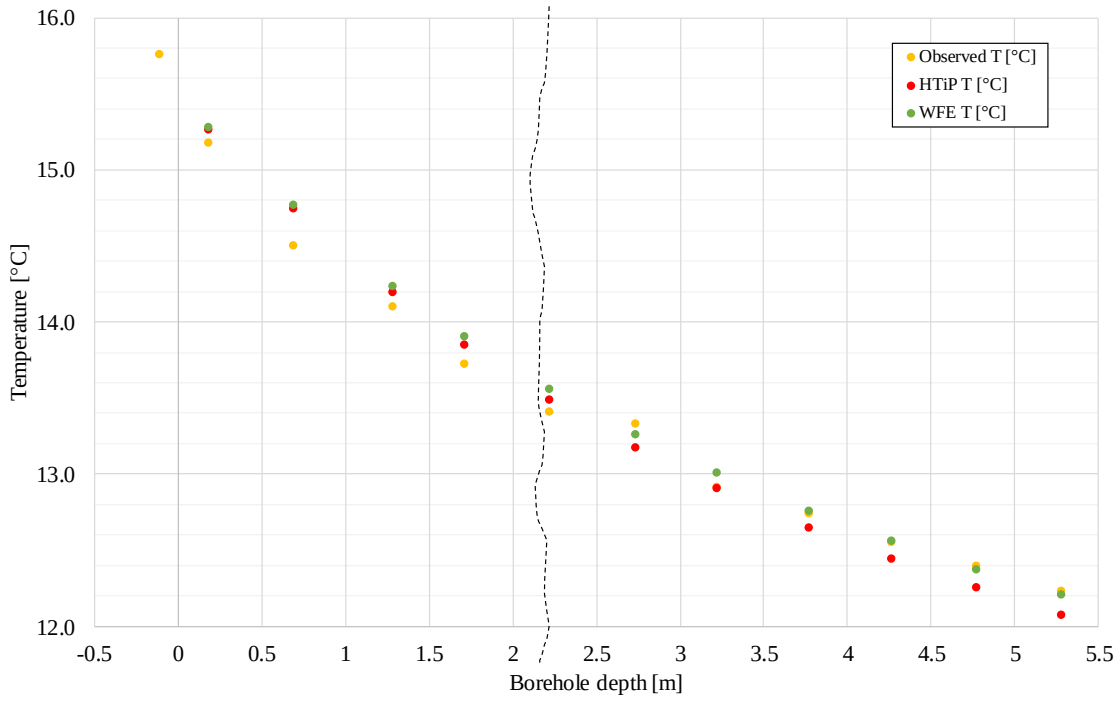

Figure 50. Initial or undisturbed ground temperature (T_{S_0}). Observed data vs. results of Scenario B simulations. The dashed line represents the probable fracture present in the monitoring borehole.

In the 3D Comsol® model, the simulated thermal sensors are located at 0.94 m to the left hand side of the heat source, corresponding to the axis along the monitoring borehole. In

the *in situ* experiment; however, the central axis of the borehole is located between the two thermal probes, with the sensors located approx. 0.02 m to each side. The readings obtained from the probes reflect the temperature of the borehole wall at these points.

Finally, the 3D models do not consider the discontinuity created by the borehole itself at the monitoring point, this can have an effect in the readings as it has been seen that the gap buffers the heat transfer.

By analyzing the first measurements given by the two thermal probes moments prior to initializing the circulation of the heated carrier fluid, the differences in the baseline temperature are evident. The variation, up to *0.5°C*, is result of a first attempt to start the circulation of hot water in the BHE; however, due to loses in the system this first step lasted only 8 hours, enough to increase the disturb the temperature of the rock. Four days passed to allow the rock to cool down before restarting the water circulation. Nonetheless, the temperature did not drop as expected, leaving the temperature at that moment as the new initial temperature.

Figure 51 illustrates the results for the preheating temperature on Scenario B for both models and the initial values observed by the two probes installed (P3 & P4) at $T = 0$ (T_0). A fifth series (T_{SO}) is plotted to illustrate the difference between the undisturbed ground temperature and the initial value after the mentioned 8 hours of circulated heat.

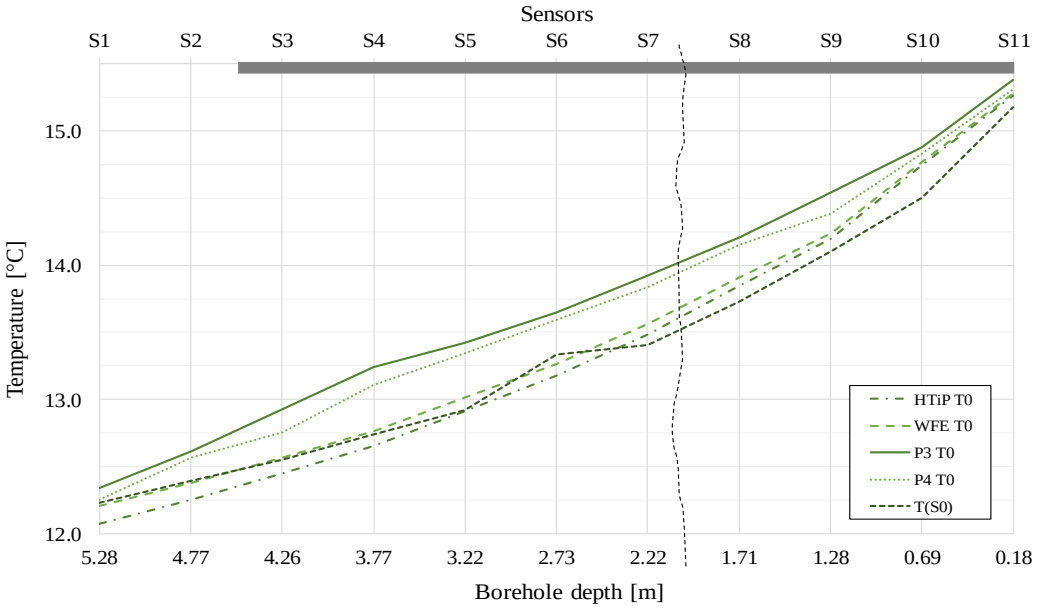

Figure 51. Initial temperature in MOBH for modelled results of Scenario B and observed data in the multi-sensor thermal probes (P3 & P4). T0 is the initial time (T=0). Dashed line: probable fracture present in the MOBH. Gray scale (upper section): length of the loop in the BHE.

Heating phase

The temperature profiles obtained from the simulations are now contrasted against the observed temperature profile in the monitoring borehole in Figure 52 where four different curves can be observed. Two curves correspond to the simulated results of the two different models for Scenario B (*HTiP & WFE*), and two series that represent the temperature measured in the monitoring borehole (P3 & P4).

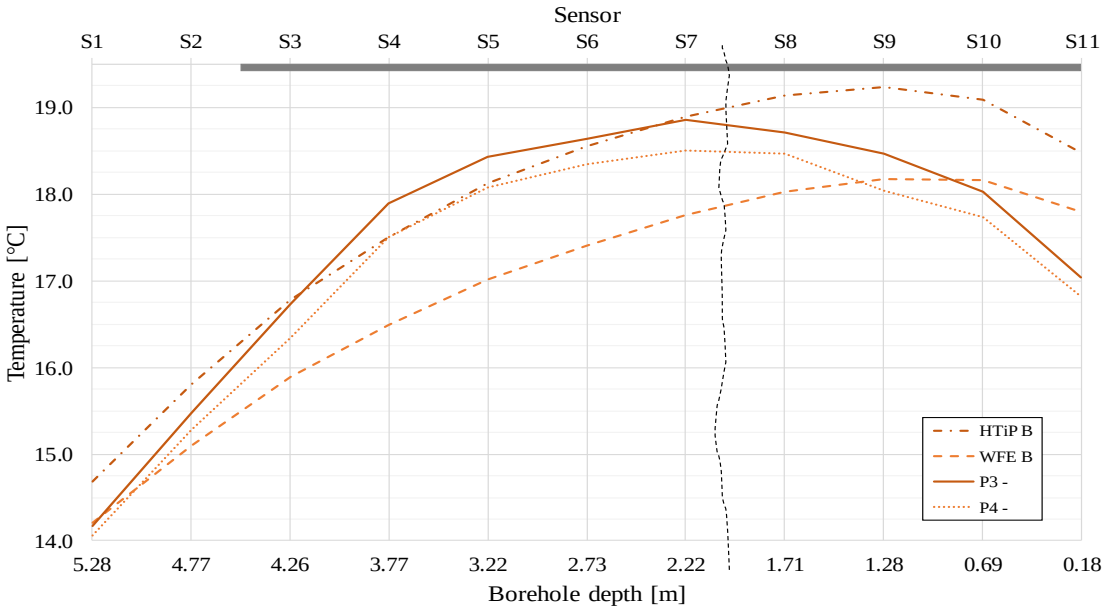

Figure 52. Temperature profile in MOBH after the finalized heating phase. Dashed line: probable fracture present in the MOBH. Gray scale (upper section): length of the loop in the BHE.

The observed profiles in MOBH have almost the same shape for both thermal probes, varying in values due to the discontinuity in the ground and the distance to the heat source. The behavior is the same in both probes, running parallel one to another, as installed in MOBH. Same behavior can be observed in the simulated results, where the difference in values between models is higher (up to *1.188°C*) than the difference between the probes (*0.086°C*).

Both probes show a closer value to the results provided by the *HTiP model* for sensors 3 to 7, being Probe 3 the closest one to the *HTiP model* curve. Notwithstanding are the values at the points closer to the collar & the toe, where the discrepancy between the simulated temperature values and the monitored values is prominent.

The bigger difference between the simulated and the real data is found at the borehole extremities. The variation percentage is calculated for each sensor as

$$Variation[\%] = \frac{T_{Model_j Sensor_i}}{T_{Probe_k Sensor_i}} - 1$$

where $Sensor_i$ is the ID of the sensor compared, $Probe_j$ is the measuring probe (3 or 4), and $Model_k$ refers to the model used (*HTiP* or *WFE*).

For the values of P3 against the results from *HTiP* (HTiP-P3), for example, the variation in the temperature is *3.59%* at the toe, and *8.44%* close to the collar, meaning the HTiP model calculated a higher temperature of such at the mentioned points. For the sensors in the range S3 – S7, the maximum absolute variation would be *2.17%* at S4.

Figure 53 summarizes the variation in the results of observed against model for both models and probes. Probe 3 and *HTiP model* present the best correlation of the four cases by having the least variation in values.

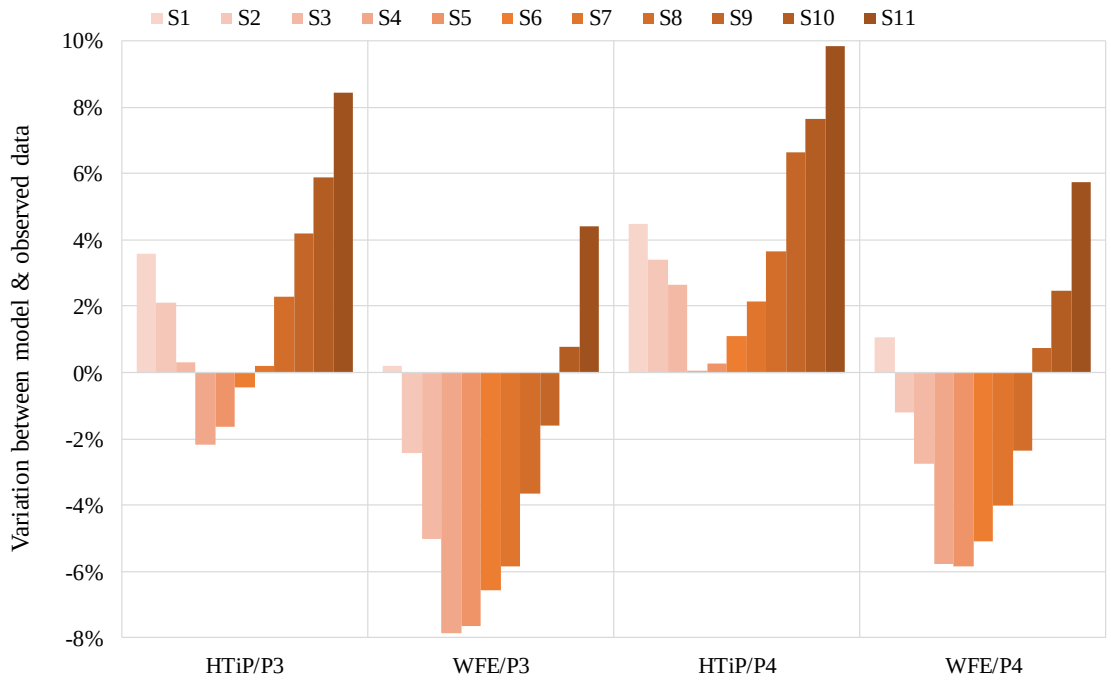

Figure 53. Variation in sensor temperatures after heating. Model over observed.

It is important to outline, during the experiment time different factors could have inference in the variation of the values in the boreholes extremities. In first instance, the flow of air inside the tunnel was never the same as during weekdays people were

performing tasks in the tunnel, turning off the ventilation, and vice versa when finishing the shift or during weekends.

In the toe area, the discrepancy in the values could be explained as result of the construction processes of the BHE. During the grouting, previously mentioned, an air pocket could have been left at the end of the borehole, creating a buffer zone due to the low thermal conductivity of air and decreasing the amount thermal energy transferred in this area.

Cooling phase

Different to the results of the heating phase, the profiles in the cooling phase lay in between the simulated values. In Figure 54 can be seen how the trend of the series is still quite similar for the four cases, presenting a drop after S7 in direction to the collar, just as seen previously for the heating case.

This repeated effect could corroborate the inference some conditions in the tunnel might have had over the variation of these values. For example, during the last days experiment, a fan was placed very close to the BHE wall area, affecting the temperature in the wall surface. Currently the models do not take into consideration such externalities.

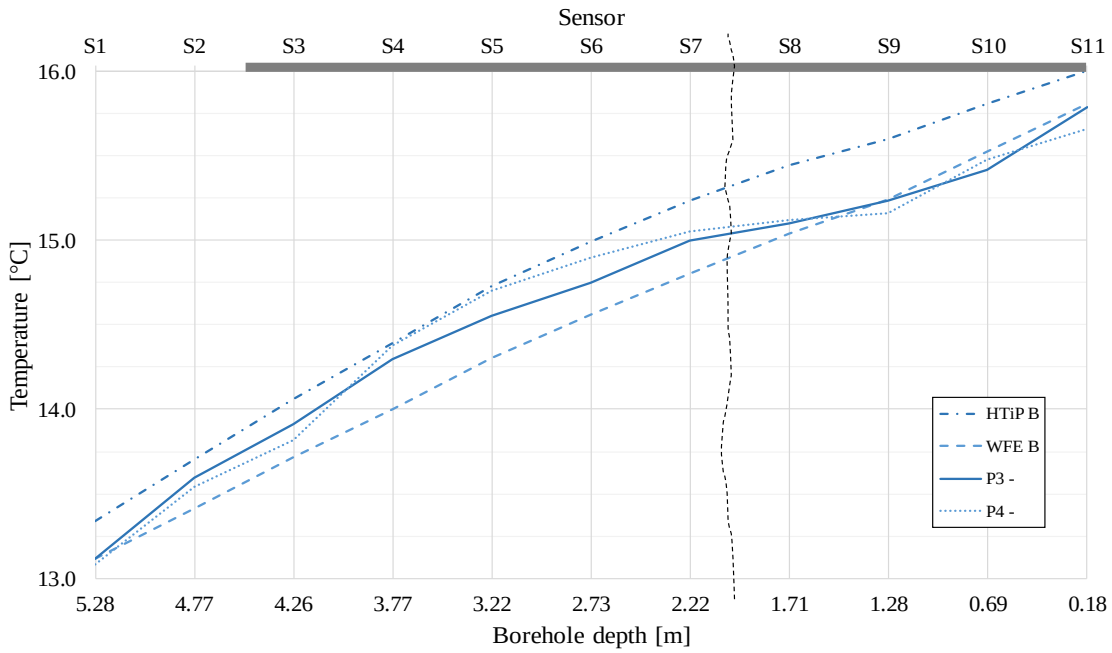

Figure 54. Temperature profile in MOBH after the finalized cooling. The dashed line represents the probable fracture present in the MOBH. The gray scale (upper section) represents the length of the loop in the BHE.

The variation in the values after the cooling period is shown in Figure 55. For the HTiP *model* the prediction is overestimated for all the sensors, been the maximum variation in P3-S10 with *2.54%*. Compared against P4, the highest variation is at S9 with *2.89%* difference.

Furthermore, the *WFE model* underestimates the predicted values in the model for both cases P3 and P4, with the exceptions of the sensors closer to the wall, where the predicted values are higher as no ventilation is considered, just like in the *HTiP model* case.

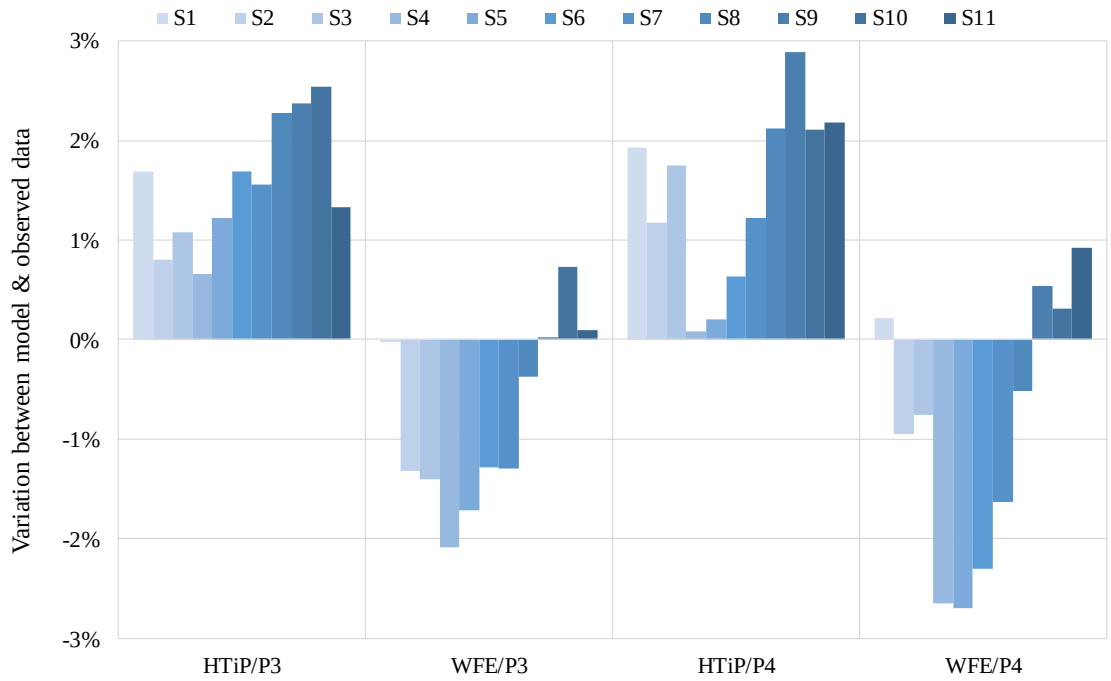

Figure 55. Variation in sensors temperature after cooling. Model over observed.

Stored thermal energy (Temperature gained)

The simulated temperature gain with the *HTiP model* shows a closer relation to the stored energy recorded *in situ* for the sensors located in the center of the borehole for the heating phase (Figure 56). However, the increment in temperature is over estimated by the model at the sensors located in the toe and closer to the wall, probably because of the discussed factors.

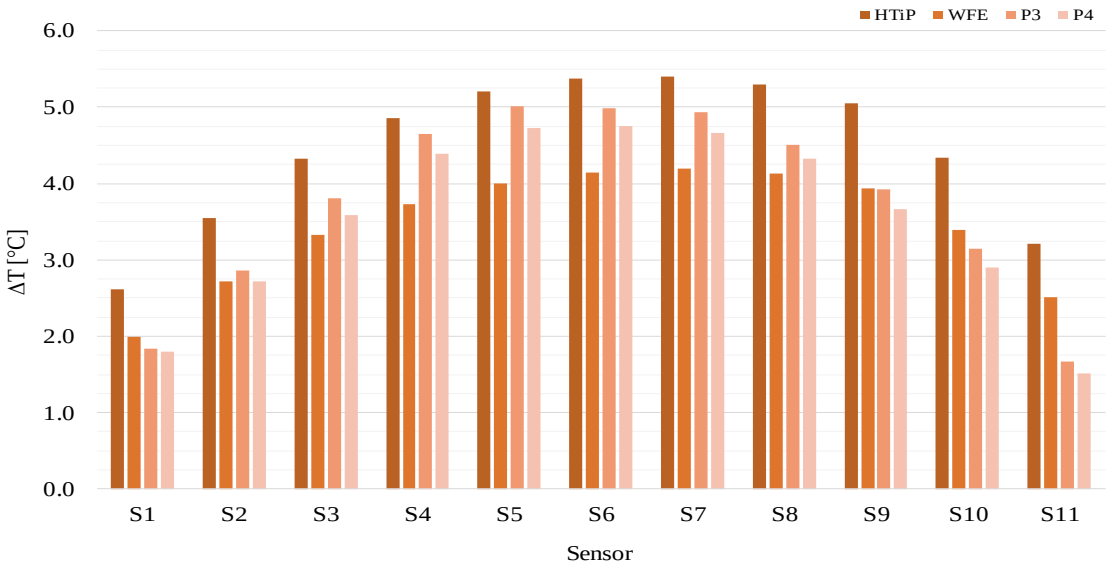

Figure 56. Data comparison. Temperature increment at each sensor in MOBH after heating. Model vs observed.

In Figure 57, referring to the cooling phase, the closest similarity in values is found with the WFE model over all the length of the borehole. This result outcome was expected by looking at the final temperature curves graph where the *in situ* values lay in between the modelled values. It is important to bear in mind, the initial temperature for the simulated cases and the *in situ* measurements were not the same, affecting the difference between the simulated and real gained temperatures, where the simulated temperatures present a bigger increment.

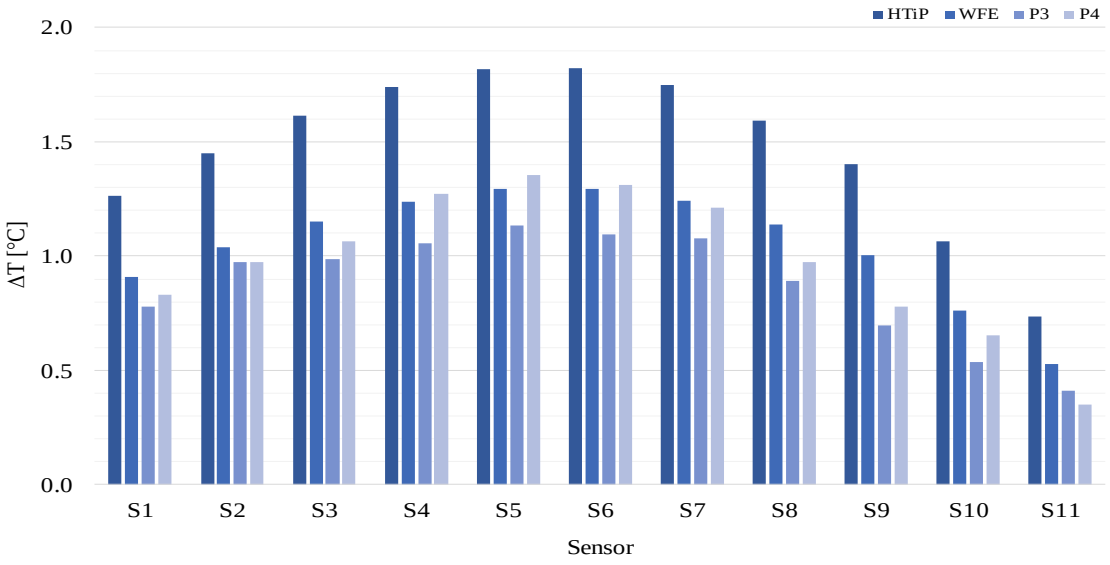

Figure 57. Data comparison. Temperature increment at each sensor in MOBH after cooling. Model vs observed.

Temperature profile evolution

An additional comparison of the evolution in the temperature profiles is presented. The following figures show the increment in the measured and simulated value at the monitoring borehole for every 5 days periods. Two figures have been previously introduced, the initial temperature and the temperature in the MOBH after the heating phase in day 21. The additional figures present the profiles for the days in between.

The temperature curves in MOBH present a quasi-identical trend and very close values at the beginning of the heating phase. With the development of the experiment though, the profiles start to grow apart, especially when contrasting the simulated values curves one against each other. The profiles corresponding to the *HTiP* and the *WFE* models show an increased separation after 10 days of heating, when the *HTiP model* starts to return higher values.

The thermal probes, on the other hand, show a close relationship to each other maintaining the temperature difference between sensors almost constant during the length of the heating phase. Likewise, the trend is constant with a few variations in the first 2.0 m of the borehole.

Finally, the difference between the values monitored and simulated become less with the increment in heating duration. Before the 10^{th} day, the values seem to be quite out of range, having the model underestimating the temperature in the MOBH, specifically for the central region of it, and with very similar values for the borehole's extreme points.

By the end of the phase, however, the situation is shifted by closer values at the toe and the borehole center in comparison to the wall contact area where the both models overestimate the temperature. By looking at the evolution of the models and the closer quantitative similarities with the observed data over time, it could be inferred, the longer the experiment the better correlation with the modelled data. Nonetheless, this is an assumption that would require corroboration.

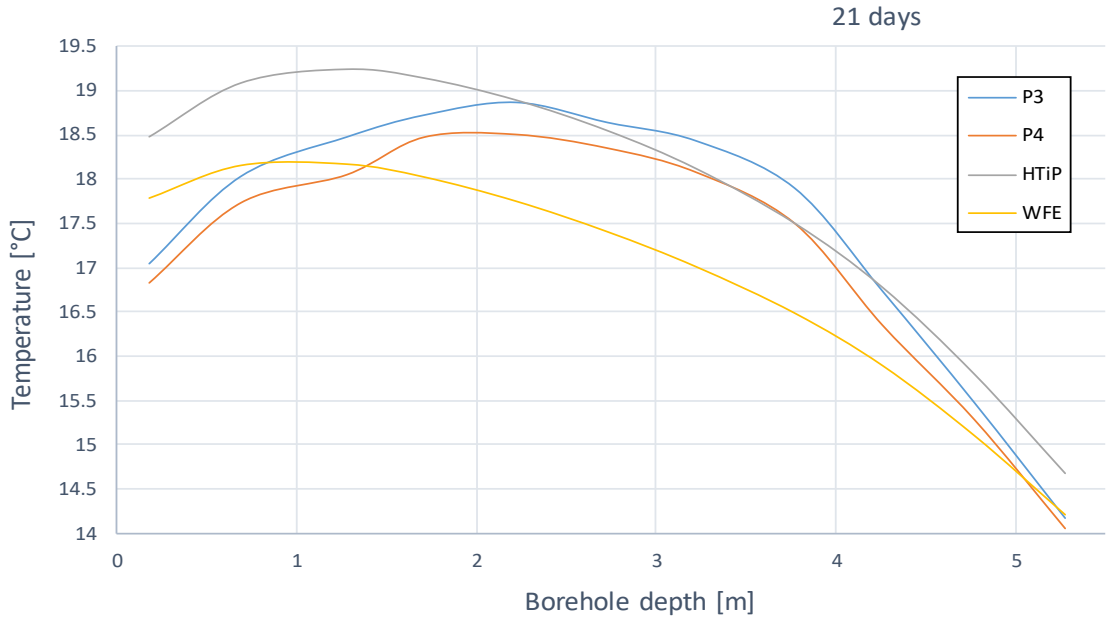

Figure 58. Temperature profiles for simulated and recorded values at day 21.

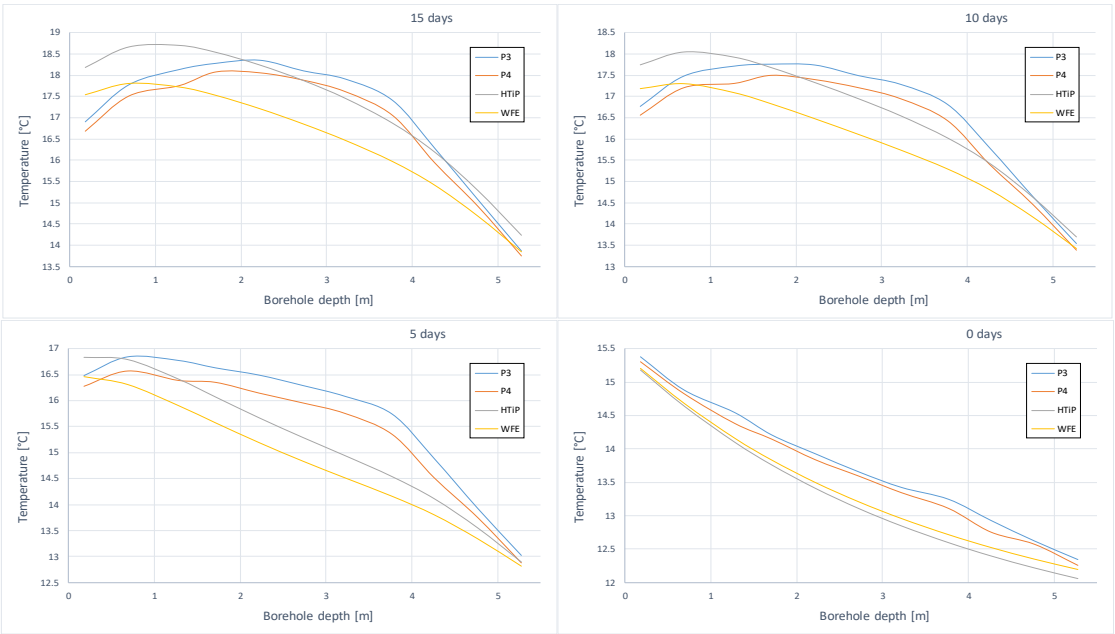

Figure 59. Evolution of temperature profiles for simulated and recorded values on 5 days steps

Carrier fluid temperature

The temperature in the carrier fluid was also compared. In the last model, the temperature of the fluid was inserted into the model as a table, having the average temperature values per hour corresponding to the length of the heating phase. However, on a first approach, the temperature was set as an average, allowing the models to calculate the changes in the temperature of the carrier fluid with time. The comparison between the obtained values of the monitoring and the initially simulated values are presented in Figure 60.

The figure shows that the carrier fluid temperature in the outlet of the system was simulated close to the measured values, although with a discrepancy of *0.27°C* for the *WFE model,* and *-0.17°C* for the *HTiP model,* approximately. Nevertheless, the tendency in the simulated value is similar to the one monitored, giving validity to this step in the models.

The inlet temperature is set as an average, meaning no calculation is done during the length of the heating phase, reason why the tendency and correlation with the measured values is better.

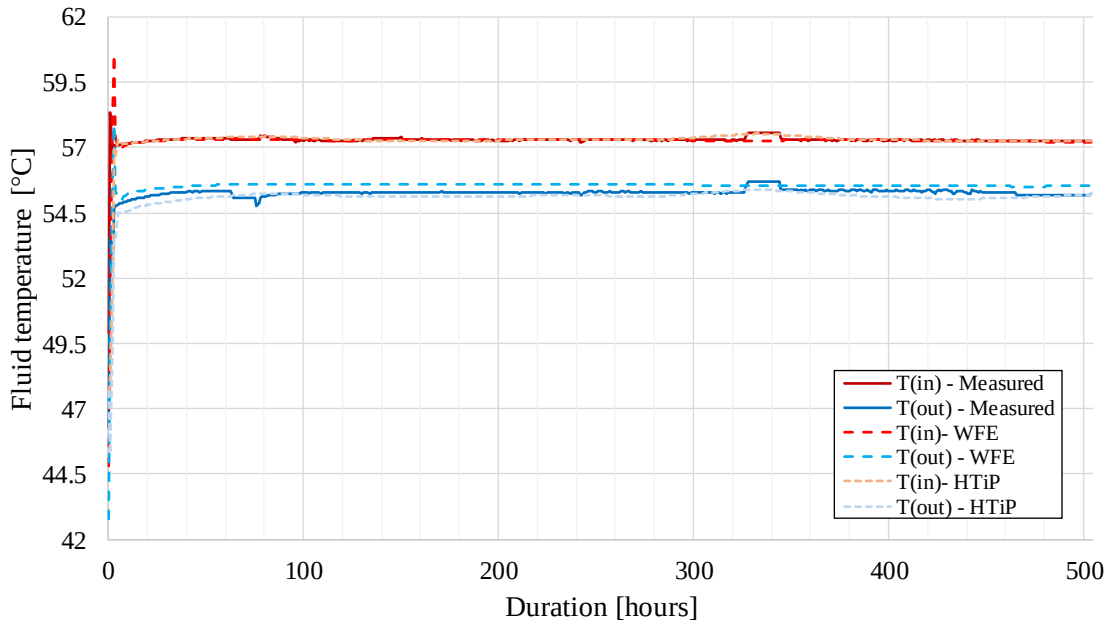

Figure 60. Carrier fluid temperature at the in- and outlet sensors during the heating phase. Model vs observed.

5.2 Thermal Response Test

The section presents the calculation of the thermal conductivity and the borehole thermal resistance parameters for the BHE configuration through a thermal response test (TRT). The calculation process used is based on the example presented in Banks (2002). The TRT had to be conducted after the thermal flow experiment due to time constrains caused by drilling and loses in the pipe system

The duration of the TRT stage was **99 hours** (a total of 5,945 minutes), with constant power input and semi-constant flow rate for the following configuration

- 5.0 m long borehole
- 4.5 m long U-tube loop
- 107 mm borehole
- Granite/gneiss rock
- 2.4-3kW water heater

Figure 61 plots the results of the fluid temperature measurements during the TRT stage, for which the initial average ground temperature T_{S_0} was set as **14.024°C** from the last temperature measured after cooling. The mean temperature (T_{ave}) in the loop is calculated as the average temperature of the inlet (T_I) and outlet fluid temperature (T_O).

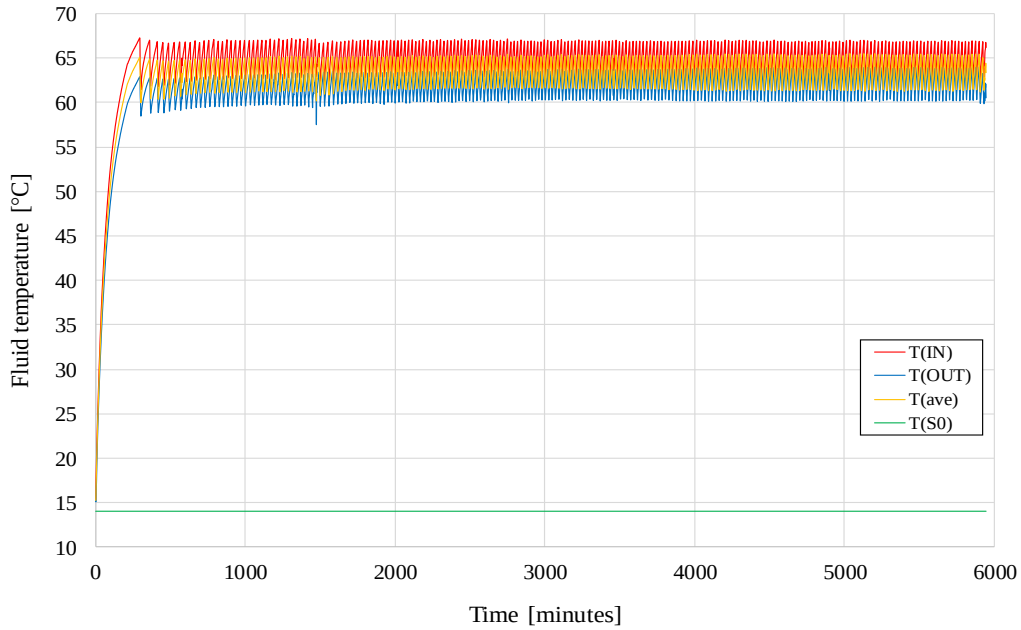

Figure 61. Fluid temperature records from the in- & outlet ($T_{(IN)}$& $T_{(OUT)}$) measuring points. $T_{(ave)}$ is the mean fluid temperature, and $T_{(S0)}$ refers to the undisturbed ground temperature, in this case the initial temperature of the ground before the TRT.

The overall mean temperature of the fluid was **62.861°C** for the observed time, with $T_{I_{ave}}$.*64.421°C* and $T_{O_{ave}}$.*61.3°C*.

In similar manner, Figure 62 plots the variation in the fluid velocity for the duration of the TRT. The overall average flow rate was measured as **216.504 L/h** or **0.06 m3/s**. Considering the pipes cross-sectional area, the average velocity is u=**0.299 m/s**. The flow regime is fully turbulent according to Eq. (5) *(5)*and the thermodynamic properties of water at 62.8°C.

$$Re = \frac{\rho u D_h}{\mu} = \frac{981.283\left[\frac{kg}{m^3}\right]*0.294\left[\frac{m}{s}\right]*0.016[m]}{0.448x10^{-6}\left[\frac{m^2}{s}\right]} = 10,513$$

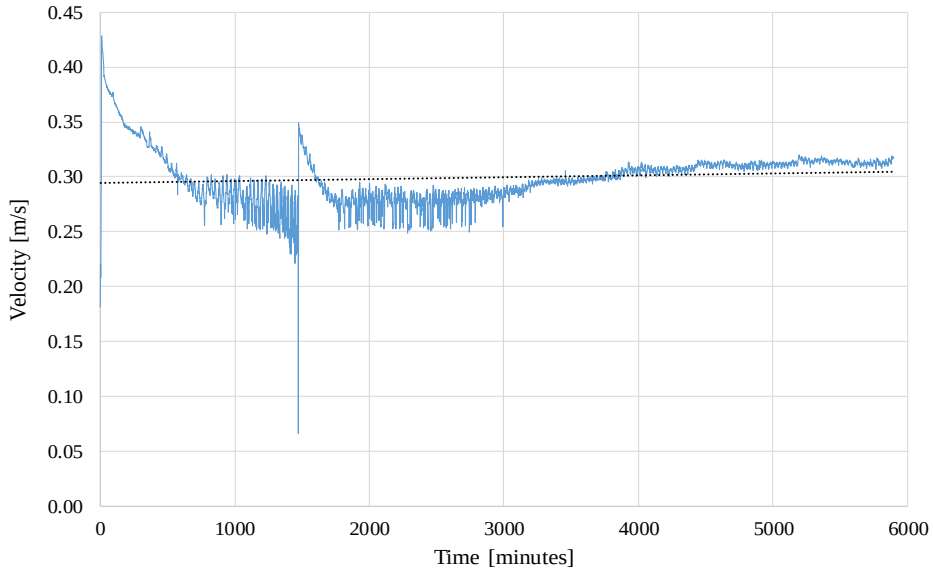

Figure 62. Carrier fluid velocity in the BHE loop during the TRT duration.

The mean temperature displacement ($T_{ave} - T_{s_0}$, MTD) in the BHE is obtained by subtracting the undisturbed rock temperature T_{s_0} from the mean fluid temperature T_{ave}. The resultant curve is plotted in logarithmic ($\log_{10}$) scale and a straight line is fitted to the linear part of the curve to obtain the temperature gradient per $\log_{10}$ cycle, as shown in Figure 63.

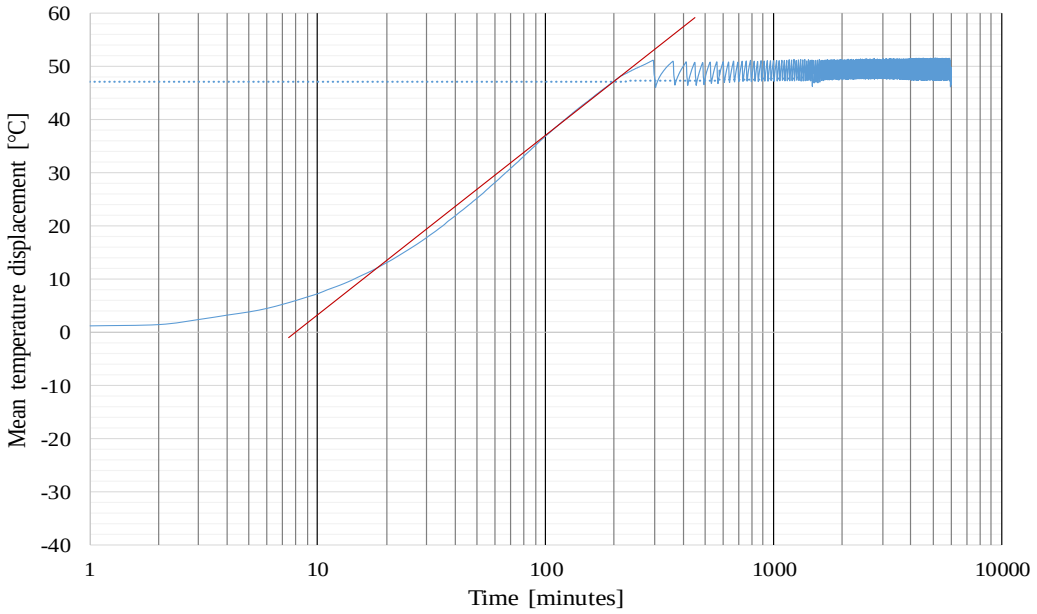

Figure 63. Mean temperature displacement for in the EXBH with the x-axis in log scale. The red line represents the portion considered for the evaluation of the gradient per cycle of log_{10}.

The literature suggests leaving out of consideration the first 10 hours (600 minutes) of data collected under the premise that at later times, the heat front has expanded until the rock mass, measuring the actual thermal properties of the ground, and not only the grout.

The back-calculation process to determine the value of thermal conductivity from the experimented data becomes iterative depending on the assumption of the S_{VC}, or vice-versa. Accordingly, the mean values obtained from the laboratory tests were used as a first approach to calculate a S_{VC} value by solving Eq. (3)*(3)*, as well as the minimum time required for the experiment.

A minimum experiment time is suggested depending on the thermal properties of the ground and the borehole size. Two minimum experiment time values were calculated, t_{min1} and t_{min2}, corresponding to Eqs.(20) - (22)*(20)(21)*, respectively, being the second approach the conservative case.

λ_{ave}	2.872	W/m·K
α_{ave}	1.518	x10^{-6} m^2/s
S_{VC}	1.892	MJ/m^3·K

	Seconds	**Minutes**	**Hours**
t_{min1}	210.80	3.51	0.06
t_{min2}	843.21	14.05	0.23

These values of t_{min} mean the logarithmic approximation for the BHE configuration becomes valid after **14.05 min** for this borehole configuration by following the most conservative approach, much sooner than the recommended in literature.

An explanation to this effect could be that the size of the borehole has a big influence in the speed at which the logarithmic approximation is likely to be valid. Banks (2012) mentions in fact, the narrower the borehole diameter, the sooner is likely to get the log effect, and ends recommending boreholes with a diameter bigger than 150 mm to perform TRTs.

In this project; however, the borehole diameter used for the whole experiment (with its respective stages) is less than the recommended one, mainly due to the availability of drilling resources. Additionally, the length of the borehole is much shorter than previous studies cited by different authors. Finally, the distance between pipes and borehole walls is very small (1 cm), reducing the influence provided by the grout for this configuration.

The length of the borehole has a direct effect in the calculation of the BHE's thermal conductivity by influencing the heat rate (q) into the system. Heat rate can be obtained through Eq.(50).

$$q = \frac{Power}{length_{loop}} = \frac{P}{L} \tag{50}$$

where P is the heater power in W, and the L is the length or depth of the loop in meters inside the borehole.

$$q = \frac{2400(W)}{4.5\ (m)} = 533.333\ \left[\frac{W}{m}\right]$$

The minimum time is represented by the orange box in Figure 64; this part of the curve is left out of consideration for the calculation of the gradient. On the opposite side, the green box leaves out the part where the measurements became practically unchanging. At this point can be said the system reached its thermal equilibrium, or the heating power and flow rate were not enough to keep the increment in temperature, probably due to limitations of the heater.

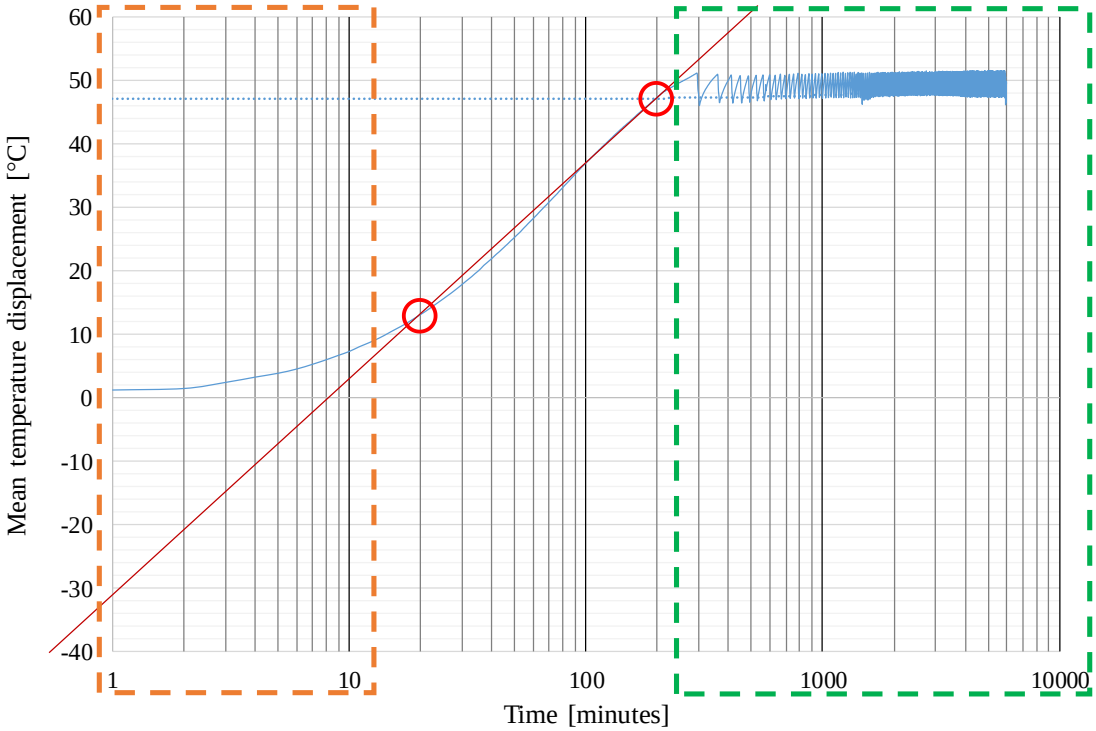

Figure 64. Graphical evaluation of the MTD Log₁₀ curve.

Once the minimum time has been established, and based on the curve of the mean temperature displacement in the BHE, a straight line is fitted to the linear portion of the curve, obtaining the temperature gradient per $\log_{10}$ cycle that can be expressed as

$$Gradient\ (°C\ per \log_{10} cycle) = \frac{2.303q}{4\pi\lambda} \tag{51}$$

Two points corresponding to the temperature values at the minutes 20 and 200 were chosen to obtain the gradient since the range represents the linear part of the $\log_{10}$ curve for the mean temperature displacement.

x_1	Log(20)	Minutes	y_1	14.06208	°C
x_2	Log(200)	Minutes	y_2	48.21825	°C

$$Gradient = 48.218 - 14.062 = 34.156\ \left(\frac{°C}{\log_{10} t}\right)$$

Now with the gradient of the temperature curve, the thermal conductivity of the borehole configuration can be obtained by solving Eq. (51) for λ.

$$\lambda = \frac{2.303q}{4\pi Gradient} = \frac{2.303 * 533.333\left[\frac{W}{m}\right]}{4 * \pi * 34.156\left[\frac{K}{\log_{10} t}\right]} = 2.862\left[\frac{W}{mK}\right]$$

By extending the gradient line until $x = 0$, the interception with the y-axis can be found. Since the curve of the MTD is in logarithmic scale, the intersection at $x = 0$ is complicated to graph. Using the trend line function in MS® Excel the interception is found at $y = -34.561°C$. Figure 65 illustrates this step, plotting the analyzed portion of the MTD curve, the gradient, and the interception point dictated by the trendline equation.

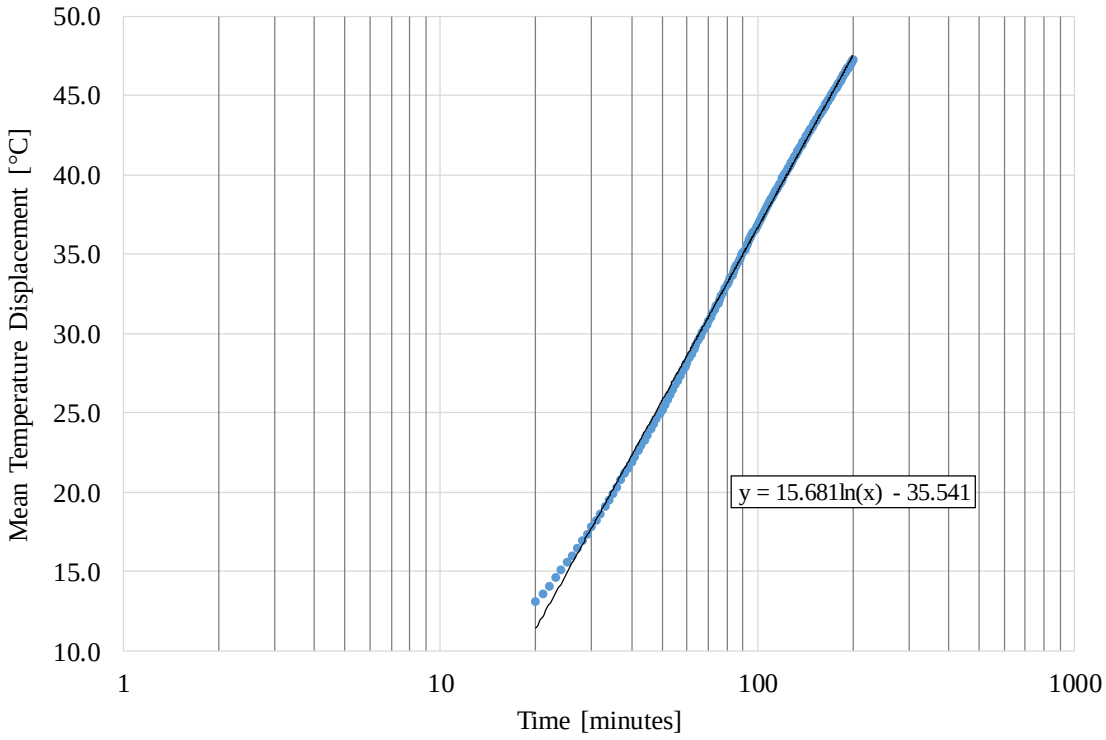

Figure 65. Zoom-in to the analyzed data and corresponding equation

The borehole thermal resistance is calculated with Eq. (52) using the previous values of λ and S_{VC}, the interception on the y-axis, and the design parameters for the BHE configuration.

$$Intercept = qR_b + \frac{q}{4\pi\lambda}\left[2.303\log_{10}\left(\frac{4\lambda}{r_b^2 S_{VC}}\right) - 0.5772\right] \quad (52)$$

where r_b is the borehole radius expressed in mm, S_{VC} in MJ/(m^3·K), and λ in W/(m·K).

Solving for R_b, Eq. (52) can be rewritten as

$$R_b = \frac{Intercept}{q} - \frac{1}{4\pi\lambda}\left[2.303\log_{10}\left(\frac{4\lambda}{r_b^2 S_{VC}}\right) - 0.5772\right] \quad (53)$$

$$R_b = \frac{-34.561}{533.333} - \frac{1}{4*\pi*2.862\left[\frac{W}{mK}\right]}\left[2.303\log_{10}\left(\frac{4*2.862\left[\frac{W}{mK}\right]}{(0.1\ m)^2*1.892\left[\frac{MJ}{m^3K}\right]}\right) - 0.5772\right] = 0.157\left[\frac{mK}{W}\right]$$

Banks (2012) mentions, a good thermal resistance for BHE is generally <11 m·K/W, as boreholes with thermally enhanced grout are in the range 0.06-0.08 m·K/W. The result obtained for EXBH's R_b is higher than the generally considered value for poor thermal resistance (>0.14 m·K/W).

It is possible to conclude based on this analysis; the EXBH has a poor thermal resistance. This result was expected since the grout used to fill the borehole was pure cement/water mixture.

6 Discussion

An even and constant heat flux provided to the storage system without any sort of intermediate retrieval is an idealistic approach in the current seasonal storage systems. Normally, an intermediate heat pump is added to the system to increase the output temperature of the carrier fluid since the heating provided is not enough to reach the design temperature for the system to be efficient. Nonetheless, this experiment simulates idealistic conditions where the heat flux is relatively constant and stable with an elevated temperature and flow rate.

The results from the simulation process can be considered as validated satisfactory, dealing very close to the reality results for the experimentation process. The first part of the modeling, the preheating stage, show the strongest correlation of the whole experiment results by simulating the base temperature with the lowest differences when compared to the *in situ* values. Unfortunately, the first intent to run the heating phase stopped after few hours due to problems in the circuit; increasing the temperature of the rock. Additionally, the abnormally hot temperatures during the weekend just after the first attempt had an influence in the setting of the initial temperature for the beginning of the experimentation, since the temperature did not decrease to its original state.

Nevertheless, the initial temperatures for the models and the on-site values present a remarkable similarity in the temperature profile in the borehole as in a first instance. The models were set to simulate the few hours of heating prior to the correct start of the experimentation; however, these did not change as expected, leaving the initial values almost as if this step would not have been taken. Furthermore, the variation in the maximum temperature achieved by the end of the heating phase would not have changed significantly, for the same heating period, as the results of the 45/45 days model showed the increment in temperature beyond the experimental 21 days was around 1°C only.

By comparing each sensor individually, the trend in the temperature development along the monitoring borehole for both experiment phases is similar to the resulting trend of the numerical modelling. The trend for the temperature profiles along the borehole after each phase follow the same premise. The best fit obtained from this project was found between

the results of the *HTiP* and the values observed in P3 in the central area of MOBH for the post-heating period with a maximum variation of *2.17%* from the recorded values.

For the heating period, the *HTiP* model overestimated most of the values along the borehole with exception of three sensors in P3, where the values were underestimated. In a different manner, the *WFE* underestimates the temperature values for most of the values with exception of the sensor at the toe and the close ones to the wall.

The results of the second phase of the experiment present an analogously behavior to the ones at the end of the heating phase. The *HTiP* model overestimates in this case all the values read by the probes, now for the central sensors. *WFE* on the other hand, shows the similar trend between phases with the difference that the higher absolute difference is in relation to P4 instead of P3, as in the heating phase.

For both models, *HTiP* and *WFE*, the average variation in the values obtained from the comparison against the probes were in average *4%* and *1.3%* for heating and cooling phase, respectively.

The variation in the results from models to probes differ in a small percentage (up to 10% for *HTiP*-P4 at heating) mainly due to physical conditions not taken into consideration in the modeling process.

The operation of the ventilation in the tunnel represents one of these instances, with the ventilation tube found right above the experimentation area, creating some air current around the wall. Besides this ventilation tube, an extra fan was put parallel to the wall, creating an extra point of circulation, lowering the temperature of the surface. The air flow in the tunnel was not modelled and only a convection boundary with a constant tunnel temperature was used.

Other point to consider is the possibility of an air bubble trapped at the borehole's toe. Even when the grouting process went without too many complications, the air drainage from the hole could have been not as fast as the grouting speed due to the breathing pipe size, resulting in the blockage of the tube leaving a compressed air bubble inside. The presence of an air pocket in the toe would decrease the thermal flow of the area as the conductivity reduces significantly. The presence of an air pocket is an assumption, considering there is no easy method available at the tunnel to corroborate the statement.

In the experiment, two main cracks were identified from the videos taken in both boreholes. In the EXBH, the biggest crack found in the surveying seemed open in the section comprehended between the *2.5 m* and *3.2 m* depth marks, crossing the borehole vertically orientated and diagonally to the drive direction. The openness of the crack was identified during the reaming, as shards of rock were retrieve with the cuttings at that exact area. The rest of the fracture seems to be filled or was probably filled with cement during the grouting as no big variation in the temperature profile can be seen in the MOBH for such depth. Simultaneously, the thermal conductivity for the different rock types found is very similar, for which the contact in the models was overseen.

In the MOBH, on the other hand, a possible crack is visible in the *2.0* m depth mark. This discontinuity could have had influenced in the transfer of heat. Looking at the different figures for the temperature profile in the monitoring point, is possible to perceive the drop in the temperature in the first part of the boreholes is located between sensors 7 and 8, between the *2.22 m* and *1.71 m* depth marks, respectively. The drop in the temperature profile for the sensors located before the *2.00 m* mark can be a combination of such discontinuity and the effect of the airflow close to the wall surface.

In a similar manner to the presence of the discontinuity in the rock, the flow of ground water in the rock mass does not seem to have affected or modified the development of the heat profile for the investigated area. Reasons to it might be the filling of the crack with the filling material during the grouting process. Before the grouting, some water could be spotted at the borehole's collar. By inspecting it with the camera it was possible to see that after joint area in direction to the toe, no water could be seen in the borehole, indicating the water was mostly coming through it. After the grouting though, no wet areas could be seen in the surroundings of the BHE.

Additionally, the level of groundwater flow in the rock mass seems to be rain event dependent, having no presence of big water presence on the wall on the dry days of summer, and manifesting during the rainy ones although in the surroundings to the experiment area, with almost no clear visible water presence.

The current models do not consider groundwater flow or discontinuities in the rock mass. Despite the lack of these considerations, by contrasting the results of the numerical approaches to the experimentation data, these factors do not seem to be of influence in

the transference of heat in the investigated area, resulting in similar temperature profiles for the theoretical and practical cases.

It is important to mention, there is no real geological mapping of the wall subjected to experimentation, being the wall covered with shotcrete. A full assessment of the discontinuities crossed by the BHE is therefore quite difficult. Furthermore, there is no data on the ground water flow in the area, having a seemly vertical movement and area constrained, with most of it coming out from the toe of the wall in different sport along the tunnel. The experiment area not included between them.

About the TRT, the resulting effective thermal conductivity of the BHE configuration is very close to the averaged result of the two different rock types present in the borehole and that were analyzed through laboratory testing.

The obtained values of thermal conductivity and borehole thermal resistance are, for this case, effective values as they account for a specific borehole heat exchanger configuration. The grout was not thermally enhanced, fact that would reduce the thermal conductivity of the entire configuration. Unfortunately, the grout samples were not thermally scanned like the rock specimens, and therefore no thermal properties for the grout were tested, leaving room to some irregularities in the grout that could affect such properties, e.g. air bubbles. The fact the thermal conductivity obtained from the laboratory testing and the local TRT are practically the same raises questions if the results for the TRT are reliable.

First, the entire time of the experiment was correct and consistent with the recommended literature, by having a TRT time over 60 hours. Nevertheless, the evolution of the temperature profile did not look like the sources consulted, with a straight gradient quite short and soon in the logarithmic representation of the temperature.

Similarly, the calculated values for minimum experiment time are very short, 14 min in the most conservative case. The diameter of the BHE in the experiment is smaller than the recommended by literature, where is stated that for smaller boreholes the validity of the logarithmic behavior is achieved sooner and the minimum experiment time is reduced.

Also, by looking at the temperature profile development for the inlet and outlet of the system, is visible that after certain point the temperature is just cyclic, meaning the water

heater reached its limit in terms of up to which temperature he water can be heated. When the temperature of the water increases to 65°C, this limit has reached and the heater stops transferring more energy as part of the configuration of the heater. Thermocouples inside the heater help to control the temperature and power required by the heater to increase the water's temperature.

Additionally, a power controller regulated the percentage of total power used by the heater. For the TRT, the power and the heating capacity of the heater were left at 100% to work at max capacity without worrying how the power was variating, or limiting the heater to work up to an established temperature, fact that occurred by factory design when reaching the maximum temperature the heater was capable of.

7 Conclusions

Both models have predicted accurately and with relative good precision, the evolution of the heat field around the BHE and the temperature evolution in the monitoring point when being compared to the results obtained from the experiment; validating the application of the weak equations in the model, and the coupling of the module in case of the *HTiP*. The *HTiP model* have shown to overestimate the temperature for both stages, with the highest values at the toe and collar areas, the closeness to the real values in the center region is quite acceptable with an absolute variation of 2%. The *WFE model*, on the other hand, shows to be underestimating the final values by 8% and 3% for the heating and cooling stages, respectively.

From the images seen, the closer values are achieved in with the *HTiP model*, except for the areas mentioned in which local conditions have inference, such as the variation in the ventilation in the tunnel or an air pocked at the toe left during grouting. The *WFE model* has shown to have a better correlation, at least for the results of this experiment, when increasing the value of the resistance between grout and soil in 20%. From literature, Al-Khoury *et* al. (2005) have suggested to determine this value experimentally, which consistent with the improvement in results by calibrating it with the observed data.

The current models do not consider the effect of discontinuities such as changes in lithology or fractures as they need to be designed in the 3D environment by boundaries in the geometrical elements that limit the mesh for the analysis. Nonetheless, the variation in the thermal properties along the borehole can be defined easier, e.g. varying the weight of the thermal conductivity in specified distances to account for the lithology variation in the borehole.

The *WFE model* calibration can be achieved by comparing the monitored results and varying the values of some parameters that might be configuration-dependent, as the resistance from grout to soil $R_{b_{SG}}$. Both models can benefit by the definition of the lithological boundaries through the variation in the thermal conductivity according to depth.

These implementations for a better modelling are site dependent, meaning that the survey and definition of the *in situ* parameters are necessary for a more accurate simulation. The implementation of the improvements can be done either by modifying the geometrical element where the mesh is constructed, which is time-consuming, or by varying proportionally the values of the local parameters according to the survey results.

Finally, the *in situ* parameters were determined with the small experiment set, although due to the size and configuration of the borehole heat exchanger, the minimum experiment time is too short in comparison with the literature. Additionally, the logarithmic representation of the temperature evolution in the borehole reaches a point after 200 minutes in which the temperature oscillates

8 Recommendations

Although the discrepancy in the initial values does not seem to have a big influence on the further development of the temperature profile at the simulated monitoring points, it would be advisable to run the models again aiming to obtain the corresponding initial values from the monitoring. Currently different variation in the configuration parameters are tested with closer values to the obtained during the experiment time.

While the results of the two approaches showed that for an overall average flow rate and input temperature value, and for an hourly value for the same parameters, the difference is almost negligible; the use of the real and accurate data is advisable for a closer to reality evaluation when the information is available. Nonetheless, is correct to say the averaged values would also deliver reliable information for the numerical model scenarios.

Just like the real case, the models are sensitive to the variation in the physical and thermal properties of the domains simulated. Thus, it is recommended to investigate the local physical and thermal parameters of the modeled area, as well as the properties of the involved elements in the BHE for a closer reality value; the closer the values to the reality, the better prediction the models will provide. In like manner, the evaluation of the thermal conductivity for the grout samples is advisable to update such value in the models and to obtain better results.

In posterior efforts to match the different series obtained from the modelling procedures, it has been found that the calibration of the *WFE model* with the reciprocal of the resistance from grout to soil $R_{b_{SG}}$ has a better match than the weak equations without this consideration. Al-Khoury *et* al. (2005) suggest this parameter must be derived experimentally as it is entirely dependent on the borehole configuration. This was done, however, by comparing the results obtained from the experiment and the simulated values from the *WFE model*. A further corroboration of this statement could be done by running new tests in the already built BHE.

Since the presence of fractures and fault zones in the ground have an inference in the thermal flow conducted, the inclusion of these in the model is advisable if the information is available. In addition, the change in the lithology will have also an effect in the

continuity of the thermal parameters of the ground. When the local lithology differs greatly from one location to another and a high variation in thermal properties is suspected, the definition of each domain is necessary, defining the geometrical boundaries in the 3D model.

This experiment took place in an extremely low porosity, low water containing rock bed, where the existing discontinuities look also closed, therefore, no significant influence of groundwater flow. If high influence of groundwater is suspected in the area, the evaluation of the water table and the flow rate must be considered; the heat transfer mechanisms will be modified, adding convection to the thermal flow through the ground between heat source and monitoring/extraction point.

Finally, for the TRT, a second attempt to perform the test would be advisable once the undisturbed ground temperature has reached its equilibrium and bearing in mind that the results obtained are the combination of every element present in the BHE system.

References

ACRE. 2016. *Geoenergy Survey.* http://openenergy.fi/en/case/geoenergy-survey.

Acuña, J., P. Mogensen, and B. Palm. 2009. "Distributed Thermal Response Test on a U-pipe Borehole Heat Exchanger." *The 11th International Conference on Energy Storage EFFSTOCK.* Stockholm.

Al-Khoury, R. 2012. *Computational Modeling of Shallow Geothermal Systems.* London: CRC Press.

Al-Khoury, R., P.G. Bonnier, and R.B.J. Brinkgreve. 2005. "Efficient Finite Element Formulation for Geothermal Heating Systems. Part I: Steady State." *International Journal for Numerical Methods in Engineering* 63: 988-1013.

Banks, D. 2012. *Introduction to Thermogeology.* Wiley.

Bauer, D., W. Heidemann, H. Müller-Steinhagen, and H.-J.G. Diersch. 2011. "Thermal Resistance and Capacity Models for Borehole Heat Exchangers." *International Journal of Energy Research* 312-320.

Carmichael, R. 1982. *CRC Handbook of Physical Properties of Rocks.* CRC.

Carslaw, H.S., and J.C. Jaeger. 1959. *Conduction of Heat in Solids (2nd Ed).* Oxford University Press.

Chaplin, Martin. 2006. "Explanation of the Thermodynamic Anomalies of Water." *Water Structure and Science.* London South Bank University. http://www1.lsbu.ac.uk/water/thermodynamic_anomalies.html.

COMSOL Multiphysics. 2017. "Theory for the Heat Transfer in Pipes Interface." *Pipe Flow Module - User's Guide.*

Eppelbaum, L., I. Kutasov, and A. Pilchin. 2014. "Thermal Properties of Rocks and Density of Fluids." In *Applied Geothermics,* 99-149. Heidelberg: Springer.

Gehlin, S., and J.D. Spitler. 2003. "Thermal Response Rest for BTES Applications - State of the Art 2001." *9th International Conference on Thermal Energy Storage.* Warsaw. 381-387.

Gehlin, Signhild. 2002. *Thermal Response Test. Method Development and Evaluation.* PhD Thesis, Luleå: Luleå University of Technology.

Hellström, G. 2011. "Borehole heat exchangers." In *Geotrainet training manual for designers of shallow geothermal systems,* by Maureen Mc Corry and Gareth LI Jones, 31-52. Brussels: Geotrainet, European Federation of Geologists.

Ingersoll, L. R., and H. J. Plass. 1948. "Theory of the Ground Pipe Heat Source for the Heat Pump." *ASHRAE Trans.* 54: 339-348.

Janiszewski, M., E. Caballero Hernández, T. Siren, L. Uotinen, and M. Rinne. 2017. "Numerical Prediction for Underground Thermal Energy Storage Experiment in the Otaniemi Reseach Tunnel." *3rd Nordic Rock Mechanics Symposium, NRSM 2017.* Helsinki. 77-85.

Janiszewski, M., T. Siren, L. Uotinen, and H. Oosterbaan. 2017. "Modelling of Borehole Solar Energy Storage Concept in High Latitudes." *Geomechanics and Engineering (submitted).*

Kukkonen, I. 2000. "Geothermal Energy in Finland." *World Geothermal Congress 2000.* Kyushu - Tohoku.

Kukkonen, I. 1986. *Menneisyyden ilmastomuutosten vaikutus kallion lämpötilaan ja lämpötilagradienttiin Suomessa (The effect of past climatic changes on bedrock temperature gradients in Finland).* Working report YST-55, Geological Survey of Finland.

Kukkonen, I., and S. Peltoniemi. 1998. "Relationships between Thermal and other Petrophysical Properties of Rocks in Finland." *Physics and Chemistry of the Earth* 23 (3): 341-349.

Leveinen, Jussi. 2017. "Sarvivälke-kiille-gneissi (personal communication)."

Lippmann & Rauen GbR. 2017. *Thermal Conductivity Scanner.* http://www.geophysik-dr-rauen.de/tcscan/index.html.

Marcotte, D., and P. Pasquier. 2008. "On the estimation of Thermal Resistance in Borehole Thermal Conductivity Test." *Renewable Energy* 33: 2407-2415.

Mogensen, P. 1983. "Fluid to Duct Wall Heat Transfer in Duct System Heat Storage." *International Conference on Subsurface Heat Storage in Theory and Practice.* Stockholm. 652-657.

Oberdorfer, P. 2014. *Heat Transport Phenomena in Shallow Geothermal Boreholes - Development of a Numerical Model and a Novel Extension for the Thermal Response Test Method by Applying Oscillating Excitations.* PhD Thesis, School of Science, Georg-August-Universitäat Göttingen, Göttingen: Georg-August-Universitäat Göttingen, 117.

Oosterbaan, H. 2016. *Numerical Thermal Back-calculation of the Kerava Solar Village Underground Thermal Energy Storage.* MSc Thesis, Espoo: Aalto University.

Oosterbaan, H., M. Janiszewski, T. Siren, and L. Uotinen. 2017. "Numerical Thermal Back-Calculation of the Kerava Solar Village Underground Thermal Energy Storage." *Procedia Engineering* 191: 352-360. doi:10.1016/j.proeng.2017.05.191.

Rohsenow, W., C. Young, and J. Hartnett. 1998. *Handbook of Heat Transfer.* McGraw-Hill.

Sanner, B., G. Hellström, J.D. Spitler, and S. Gehlin. 2005. "Thermal Response Test – Current Status and World-wide Application." *World Geothermal Congress.* Antalya.

Sanner, B., Ma. Reuss, E. Mands, and J. Müller. 2000. "Thermal Response Test - Experiences in Germany." *Terrastock 2000.* Stuttgart. 177-182.

SDH-Platform. 2016. *Plant database.* www.solar-district-heating.eu.

Spitler, J. D., and S. Gehlin. 2015. "Thermal Response Testing for Ground Source Heat Pump Systems - An Historical Review." *Renewable and Sustainable Energy Reviews Vol. 50* 1125-1137.

2017. *The engineering toolbox.* http://www.engineeringtoolbox.com/thermodynamics-t_36.html.

TU Darmstadt. 2017. *Geothermal Science and Technology - Research.* http://www.geo.tu-darmstadt.de/fg/angeotherm/geotherm_forschung/TCS.en.jsp.

Whittington, Alan G., Anne M. Hoffmesiter, and Peter I. Nabelek. 2009. "Temperature-dependent thermal diffusivity of the Earth's crust and implications for magmatism." *Nature* (Macmillan Publishers Limited) 458 (19): 319-321.

Winkel, E. 2010. *Ekoviikki - Sustainable City Projects in Helsinki.* http://www.eukn.eu/e-library/project/bericht/eventDetail/ekoviikki-sustainable-city-projects-in-helsinki/.

Appendices

Appendix A – Location

The experiment took place in the Aalto University, School of Engineering – Research Tunnel, located under the Otaniemi Campus, in Espoo, Finland.

The tunnel is located, in average, 18 meters below the surface level (to the roof of the tunnel), varying from 19.3 m at the entrance of the research tunnel, to 16 m at the end of it, and with a height between 4.5 and 3.1 meters for the same points previously mentioned.

The characteristic rock of the area is granite with presence of hornblende gneiss, with a good effective thermal conductivity value of *3.3 W/(m·K)*. This value was obtained after some thermal response tests performed by the Finnish Geological Service (GTK) in 2016 to determine the geothermal potential in the Campus.

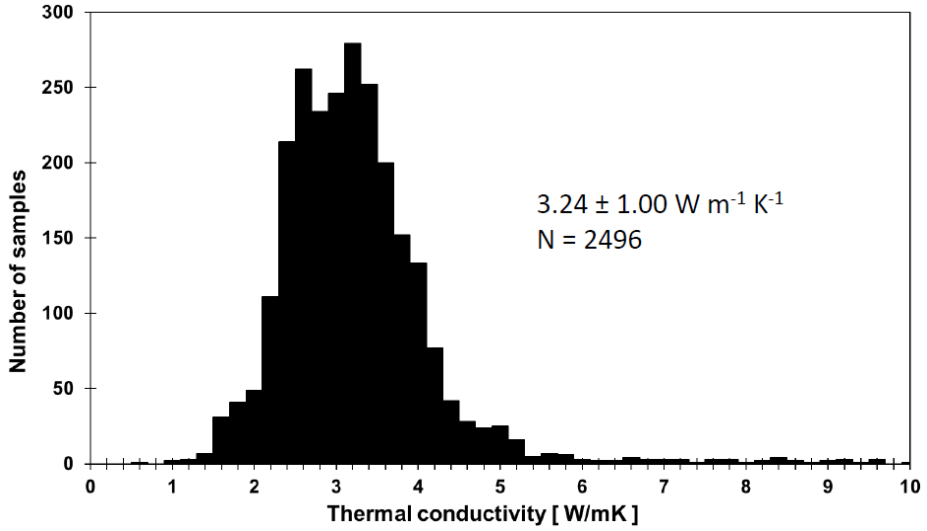

Figure A-1 Thermal conductivity of rocks in Finland after Peltoniemi (1996) and Kukkonen & Peltoniemi (1998)

Location selection criteria

In general, the overall location of the tunnel is in an area with a high potential for geoenergy, underlying in the dark-green area. Considering the drilling was to be perform horizontally instead of vertically, the selection of the area was of importance to assure the correct development of the experiment.

The following was to define the wall where the drilling would take place. Different areas were considered for this purpose, the selection of the final spot was based on analyzing the pros and cons of each location and the effect on the performance of the experiment.

Figure A-2 illustrates the five different areas inside the research tunnel considered as viable for the drilling of the BHE.

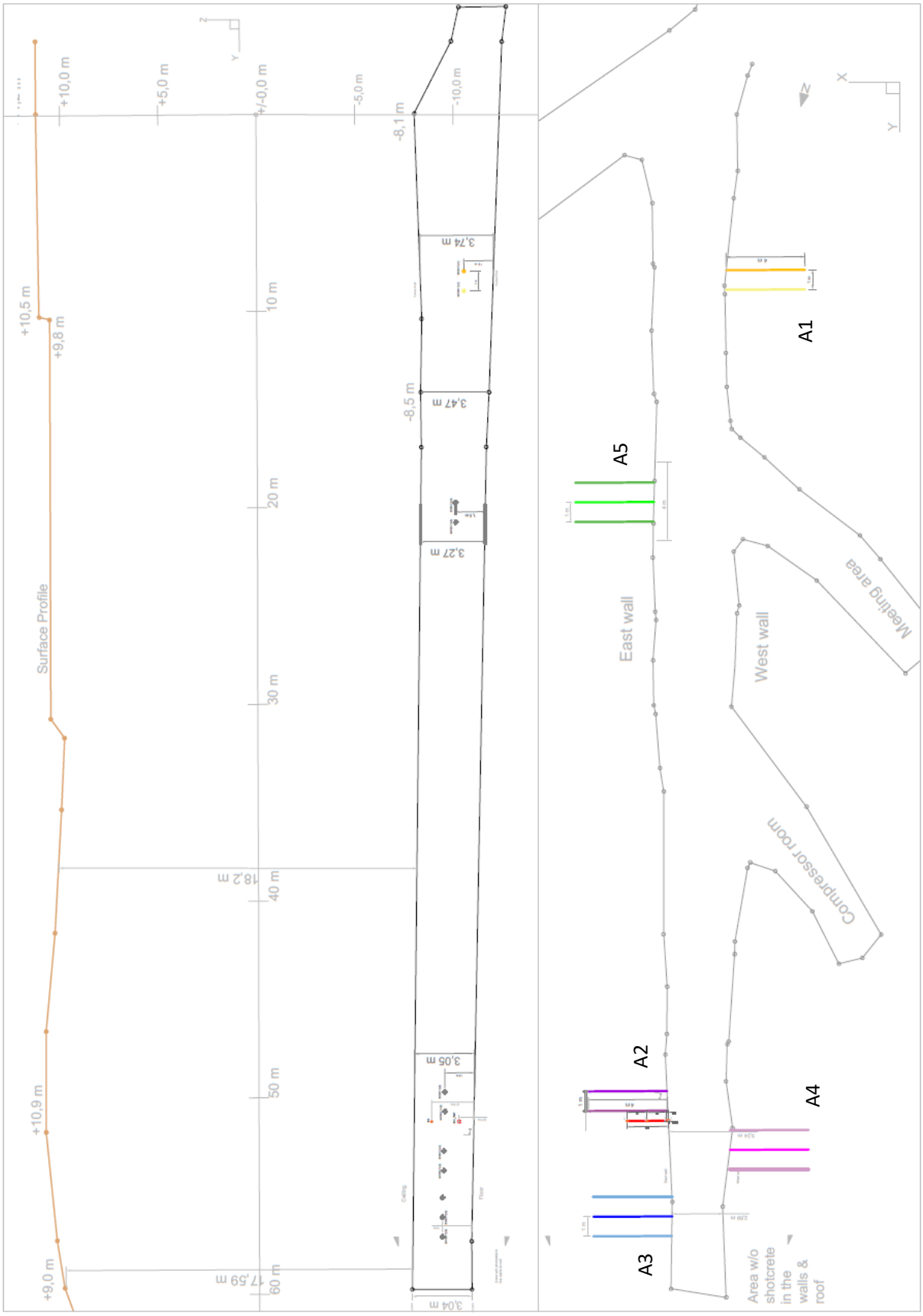

Figure A-2. Analyzed areas for experiment setting.

Factors considered for the area selection,

- Access to water and power supply.
- Continuity in the rock mass.
- Undisturbed area, at least 1.5 m radius around the experiment hole.
- Maneuverability of drilling equipment.

Table A-1. Drilling areas assessment.

Area	Pros	Cons
A1. 13 m from tunnel entrance	- Access to water supply. - Well illuminated area. - No influence of drill holes. - Grouted surface.	- Influence of the tunnel that runs parallel to the research tunnel towards the surface.
A2. 50 m from the tunnel entrance (East wall)	- The area is wide enough to place the drilling boom perpendicular to the wall. - Half of the boreholes in place grouted. - Walls with shotcrete.	- Too many boreholes drilled in the past. - Different direction of previously drilled boreholes. - It may be too close to the blasting area (to be resume in the future).
A3. 57 m from tunnel entrance (East Wall)	- No interaction with surrounding structures (no other tunnels in the near field) - Undisturbed area, small or negligible presence of boreholes.	- Too narrow to operate the drilling boom. - Impossible to drill perpendicular to the wall. - Closeness to the area without shotcrete, safety concerns.
A4. 52 m from the tunnel entrance (West wall)	- The area is wide enough to place the boom in place for the drilling. - Walls with shotcrete. - No interference of adjacent tunnels. - Undisturbed area available (small dimensions).	- Too many boreholes drilled in/around the interest area. - Three boreholes with at least over 1.4 m depth, 30-40 degrees inclination (from the wall)
A5. 20 m from the tunnel entrance (East wall)	- Area is wide enough to place the drilling jumbo perpendicular to the wall. - Walls with shotcrete - No significant presence of drill holes. - No interference of adjacent tunnels. - Easy access to power and water supply.	- Obstructions near to the area (easy movable) - Greater influence of the surface & and environment temperature conditions - Presence of GW, only in one crack running vertically.

The maneuverability of the drilling equipment played a significant role in the selection of the final area, as the intention was to obtain the straightest possible borehole perpendicular to the wall; A5 was selected as it presented the best characteristics, plus sufficient room for to operate the drilling boom.

In the end, and due to mechanical issues (maintenance) of the drilling boom, the drilling had to be performed with a handheld drilled, first by drilling a guide borehole, for its posterior reaming. The selection of the area remained the same as the preparations for the drilling were done in advance.

The test of the capability of the handheld drilled had to be tested first. Initially only 1.5m were planned to assess if it would be possible, drilling in steps of half meter until reaching the limit of the drilling equipment. Surprisingly, the drilling was able to continue to the desired depth of 5.0m, reaming posteriorly the guide borehole to obtain the result of a 107 mm borehole.

Drilling

The drilling was performed with an old Atlas Copco® handheld drill, and drill bits from the same company. A 45 mm drill bit was used for the guide borehole and the monitoring hole, and a reaming drill bit of 100 mm for the final diameter of the experiment hole.

Figure A-3. Handheld drilling equipment used.

The first borehole to be drilled was the experiment hole (EXBH). In a first instance, only 1.5 m of the guide hole were drilled to test the reaming capability of the machine and the bit. After a reamed depth of 1.7 m, and consisting with the promising results, it was decided to finalize the guide hole achieving a final depth of 5.37 m.

The reaming continued at good speed and without too many complications. At the depth of 2.5 m, however, the drilling faced a small decrease in the speed. Shards of rock were coming out with the debris, situation that was not happening at the beginning, also the color of the rock changed. A fracture zone located between 2.5 and 3.0 m of depth was identified in a posterior video survey. After the 3.0 m mark the reaming continued without bigger complication, reaching a final depth of 5.0 m.

With the first borehole drilled, the decision of where to drill the monitoring borehole (MOBH) arise. It was decided to drill to the left site of the EXBH since there is no signal of groundwater flowing through that area, and the rock seems continuous at the same level. The inclination and deviation of the EXBH were measured to drill the second borehole as parallel as possible to the first one. Table summarizes the results of the drilling.

Table A-2. Planned and final parameters from the drilling.

	Planned		**Achieved**	
	MOBH	EXBH	MOBH	EXBH
Height [m][1]	1.5		1.46	1.55
Inclination [°][2]	~ 5		13	14
Deviation [°][3]			2.5	5
Spacing [m]				
Collar	1.0		0.935	
Toe	1.0		1.192	
Diameter [mm]	50	100	50	107
Length [m]	5.0	5.0	5.3	5.0

[1] From the tunnel floor to borehole's axis
[2] From the horizontal
[3] From the perpendicular to the wall I-

Video survey
Experiment borehole

0.5 m

1.0 m

1.5 m

2.0 m

2.5 m

3.0 m

3.5 m

4.0 m

4.5 m

Monitoring borehole

Prevalence of gneiss for the majority of the borehole's length. Few spotted granite lunars at the marks of 1.5, 2.5 and 5.0 – 5.5 m.

Appendices

Appendix B – Equipment and instrumentation

Description of equipment used

Experiment borehole

The borehole heat exchanger consists on a single U-pipe composed by two PE-Xa pipes joined through a built-up brass U-turn in the extreme to be places in the end of the borehole.

A separation of 1.0 cm between pipes and borehole wall was selected to achieve a better heat flow between carrier fluid and ground, considering the thermal resistance opposed by the different elements involved (pipe-grout-rock). The pipes are orientated vertically with the water inlet and outlet in the bottom and top pipes, respectively, for geometrical symmetry. A 3kW water heater with a power controller provides the heat source for the system at a regular flow rate provided by a Willo® circulating pump.

Two flow-through thermal sensors are installed at the inlet and outlet points of the pipes, measuring on a constantly the carrier fluid's temperature coming into and out of the system. The flow-through sensors allow a better temperature reading of the carrier fluid as the thermal resistance of the pipe is subtracted from the measuring, situation that would not happen with a pipe-clamp type of thermocouple.

Besides the thermal sensors measuring the fluid temperature, two thermal multisensor probes were placed in in the centralizers to monitor two areas of interest, the boundary between rock and grout, and the grout itself. The sensors are held in place by the centralizers designed specifically for the experiment.

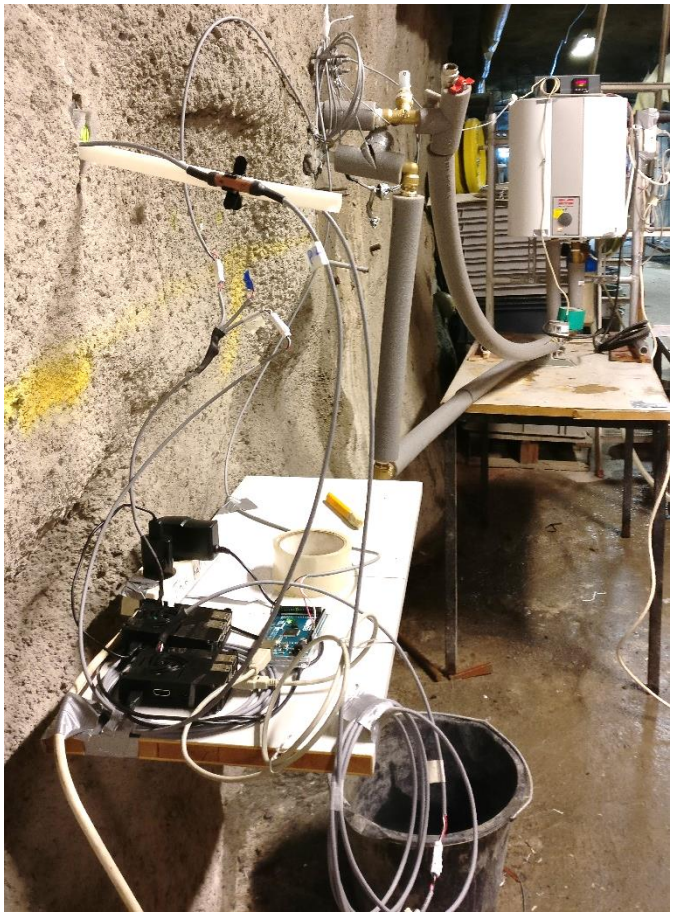

Figure B-1. Installed equipment for the experiment.

Thermal Multisensor Probes

The measurement of the rock temperature along the boreholes is done with customized equipment built the project. The set is composed by 12 digital thermal sensors and the data cable is referred in this work as *Thermal Multisensor Probe* (*Probe*, for shorter reference), and identified by the letter *P*, followed the probe number from 1 to 4, e.g. *P3* stands for the *Probe 3*. Analogically, the thermal sensors are referred with the letter *S* and followed by their position number, from 1 to 12, counting from the tip of the cable towards the end plugged to the Pi board. The identifier for the sensors is, i.e. *S6 – Sensor #6*.

The digital thermal sensors are encased in a 4.0 cm long, Ø10/01 mm copper tube to ensure the proper conductivity contact between the sensor and the borehole wall. The cased sensors are connected by a waterproof cable, and covered by shrinking tube in the contact between copper and cable. The separation between sensors is in intervals of 50 cm, spacing enough to cover the whole length of the embedded U-pipe with a good profile of the temperature evolution.

Experiment borehole

The experiment borehole was instrumented with two thermal multisensesor probes, Probes 1 and 2, placed horizontally on one half of the borehole, the half that is closer to the monitoring borehole to measure the temperature in the grout (P1) and the temperature in the boundary between grout and borehole wall (P2).

The probes are hold in place through a series of customized centralizers for the monitoring borehole.

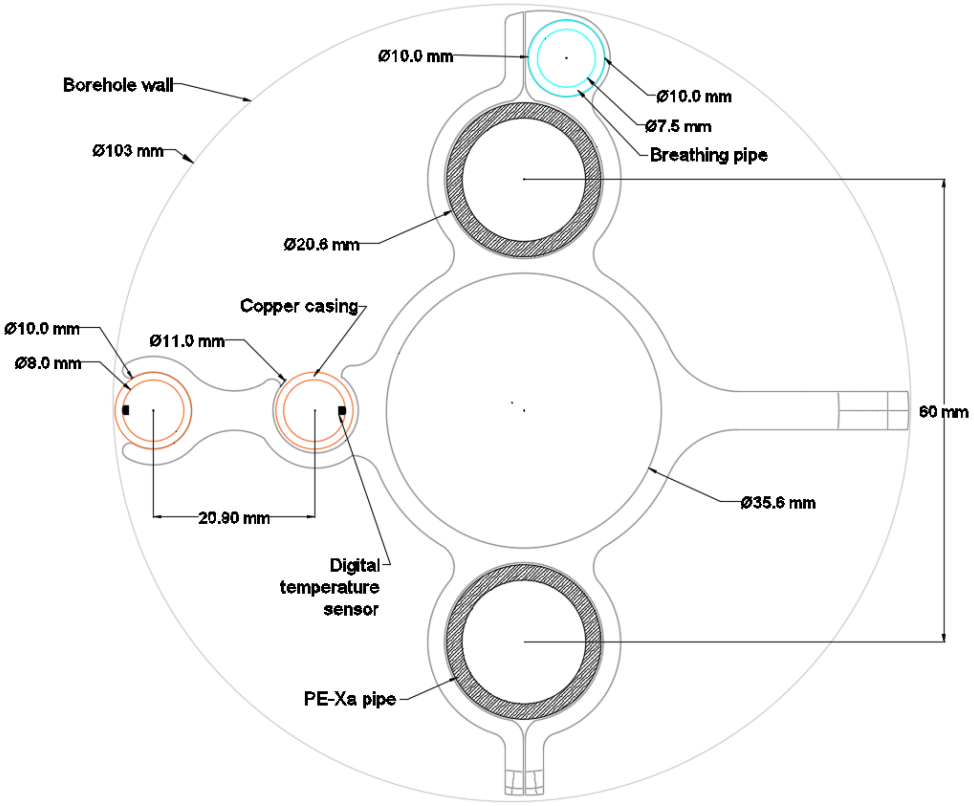

Figure B-2. Cross-section view of the thermal multisensors probes installed in the EXBH.

Monitoring borehole

The monitoring borehole was instrumented with two thermal multisensesor probes, Probes 3 and 4, placed horizontally opposing each other to take account of the effect created by the gap or opening (air inside the BH) over the temperature readings.

The probes are hold in place through a series of customized centralizers for the monitoring borehole.

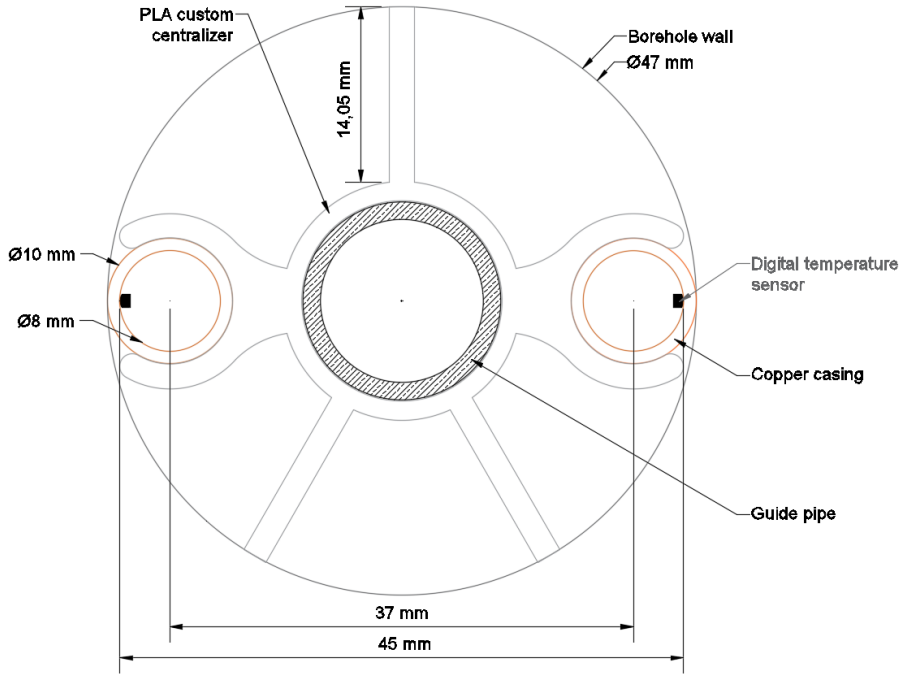

Figure B-3. Cross-section view of the thermal multisensors probes installed in the MOBH.

Data collection

The data collection of the probes installed in the boreholes and the flow-through thermal sensors in the inlet and outlet of the borehole heat exchanger loop is performed by a couple of Rasperry Pi® boards with Linux OS. An Aurdino® board is used to convert the pulses generated the flowmeter into digital data that is posteriorly visualized and stored in one of the Pi's.

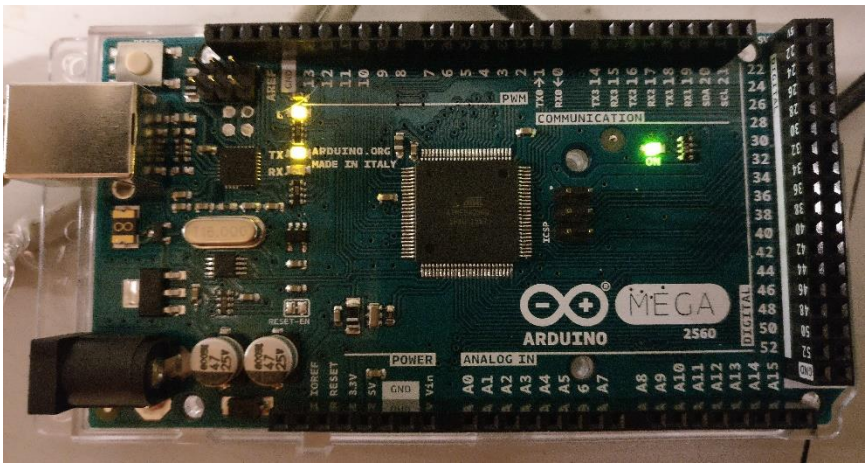

Figure B-4. Arduino® board.

List of equipment and instrumentation components

The full list of the equipment and instrumentation installed for the BHE and the monitoring is presented in this part.

Borehole Heat Exchanger

- U-pipe:
  - Two (2) 5.0 m PE-Xa pipes Ø20/02 mm.
  - One (1) custom brass U-turn pipe.
  - Thirteen (13) custom-made PLA pipe centralizers.
- Flow through thermal sensors
  - Two (2) custom made digital thermal sensors (in/out).
  - Two (2) brass T-fittings
- One (1) 2.4 – 3 kW, 15 L water heater.
- One (1) flow meter with pulse meter.
- One (1) Willo® circulating pump.
- Thermal insulation on pipes and connectors.

Thermal Multisensors Probe.

Each of the four Thermal multisensors probes was built with

- Twelve (12) Honeywell Thermal Sensors,
- Twelve (12) 4.0 cm long, Ø10/8 mm copper pipe (case),
- 7.0 m of waterproof, 3-wired cable.
- Shrinking tube.

Flow-through Thermal Sensor

Each of the thermal sensors in the inlet and outlet of the pipes is built with

- One (1) Honeywell Thermal Sensor,
- One (1) Brass T-fitting Ø20 mm,
- One (1) 8 cm long, Ø10/1 mm copper pipe (case).

-

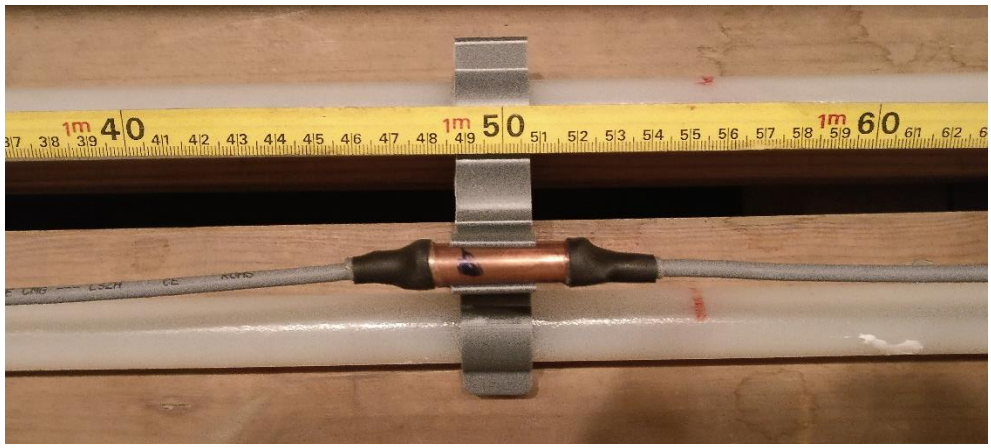

Figure B-5. Sensor in Thermal Multisensor Probe.

Appendix C – Monitored data

Temperature measured in Thermal Multisensor Probes

Probe 3

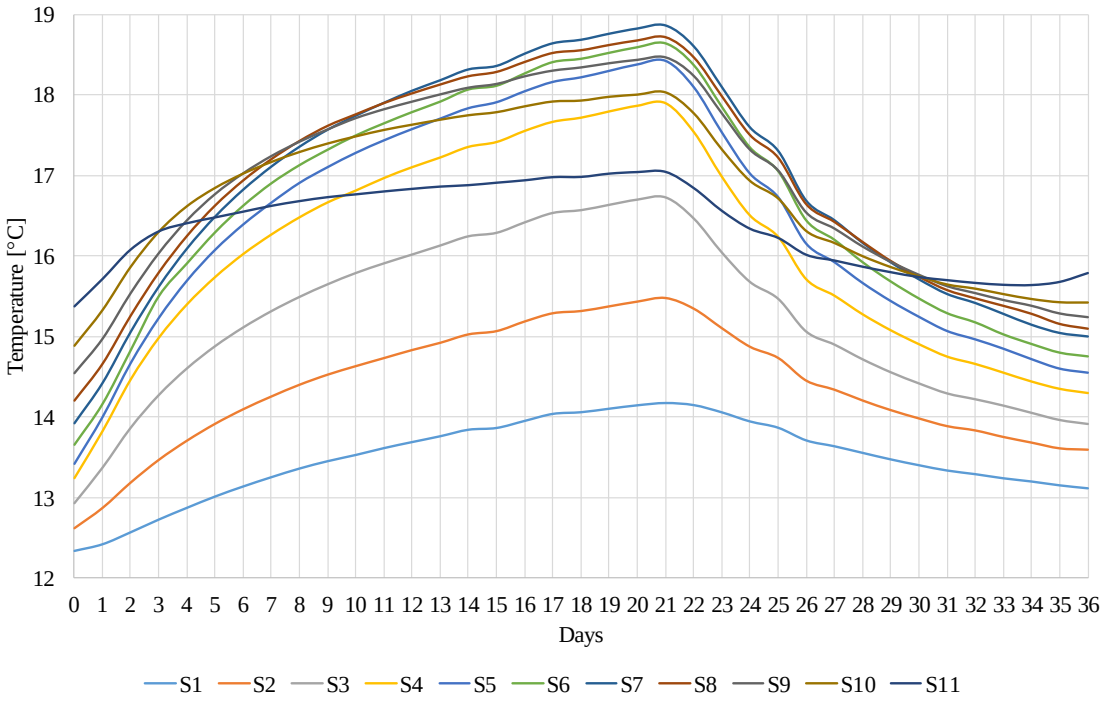

Figure C-1. Temperature profiles for the thermal sensors in the monitoring borehole during the experiment time, 21 days of heating and 15 days of cooling.

The temperature for each sensor is reported in Table as, *Initial* at $t = 0$, *Final* at $t = 36$. *Gained* is the difference between $Final - Initial$, and *Max* is the maximum temperature recorded, corresponding to the last day of heating (day 21).

Table C-1 Temperatures [°C] measured at the sensors during the experiment duration – Probe 3

	Initial	Final	Gained	Max
S1	12.338	13.116	0.777	14.175
S2	12.617	13.592	0.975	15.476
S3	12.926	13.912	0.985	16.730
S4	13.241	14.297	1.056	17.893
S5	13.420	14.552	1.132	18.427
S6	13.649	14.746	1.097	18.632
S7	13.923	15.000	1.077	18.859
S8	14.206	15.098	0.893	18.716
S9	14.541	15.237	0.697	18.470
S10	14.879	15.415	0.537	18.026
S11	15.378	15.790	0.412	17.042

During the monitoring, the probes stop recording at some points mainly by human error by trying to modify the values directly in the running code. The days without data are highlighted in Table C-. The approximation of the values was made by looking at the profile obtained from Probe 4 and adjusting the possible values missing to keep the trend in the curves.

Table C-2. Records for each sensor in the Probe 3 inside the monitoring borehole

Day	S1	S2	S3	S4	S5	S6	S7	S8	S9	S10	S11
0	12.338	12.617	12.926	13.241	13.420	13.649	13.923	14.206	14.541	14.879	15.378
1	12.421	12.869	13.369	13.825	14.001	14.156	14.423	14.663	14.969	15.322	15.717
2	12.570	13.184	13.865	14.466	14.672	14.822	15.057	15.260	15.537	15.859	16.081
3	12.728	13.466	14.272	14.983	15.233	15.494	15.619	15.797	16.035	16.295	16.306
4	12.874	13.704	14.604	15.397	15.697	15.901	16.091	16.250	16.443	16.612	16.407
5	13.014	13.914	14.880	15.736	16.079	16.287	16.488	16.628	16.770	16.840	16.479
6	13.139	14.095	15.113	16.022	16.395	16.618	16.823	16.940	17.029	17.018	16.550
7	13.254	14.253	15.316	16.265	16.666	16.896	17.109	17.204	17.243	17.162	16.622
8	13.361	14.399	15.493	16.478	16.912	17.121	17.355	17.429	17.422	17.286	16.681
9	13.453	14.524	15.650	16.663	17.107	17.313	17.567	17.617	17.574	17.391	16.729
10	13.530	14.630	15.790	16.810	17.285	17.490	17.740	17.760	17.715	17.480	16.764
11	13.615	14.730	15.910	16.965	17.440	17.640	17.900	17.900	17.825	17.560	16.800
12	13.690	14.830	16.020	17.100	17.580	17.780	18.050	18.020	17.920	17.625	16.832
13	13.763	14.920	16.132	17.220	17.710	17.910	18.180	18.130	18.010	17.687	16.860
14	13.843	15.024	16.247	17.352	17.840	18.060	18.314	18.232	18.094	17.742	16.878
15	13.865	15.065	16.290	17.412	17.914	18.107	18.358	18.286	18.140	17.780	16.908
16	13.953	15.185	16.420	17.550	18.050	18.260	18.510	18.410	18.235	17.853	16.938
17	14.040	15.287	16.537	17.663	18.166	18.401	18.639	18.522	18.306	17.913	16.977
18	14.060	15.314	16.571	17.713	18.223	18.441	18.682	18.555	18.345	17.925	16.980
19	14.104	15.372	16.638	17.791	18.303	18.515	18.757	18.620	18.398	17.972	17.020
20	14.146	15.431	16.703	17.861	18.383	18.585	18.821	18.677	18.439	17.998	17.040
21	14.175	15.476	16.730	17.893	18.427	18.632	18.859	18.716	18.470	18.026	17.042
22	14.149	15.343	16.468	17.537	18.101	18.363	18.601	18.468	18.240	17.767	16.842
23	14.059	15.101	16.044	16.981	17.538	17.844	18.095	17.984	17.773	17.317	16.560
24	13.946	14.870	15.678	16.500	17.025	17.339	17.594	17.502	17.321	16.926	16.338
25	13.867	14.731	15.468	16.235	16.733	17.046	17.303	17.221	17.063	16.708	16.225
26	13.710	14.449	15.060	15.708	16.154	16.433	16.683	16.642	16.538	16.303	16.016
27	13.637	14.337	14.899	15.505	15.925	16.193	16.442	16.423	16.340	16.155	15.945
28	13.555	14.203	14.716	15.274	15.667	15.915	16.161	16.175	16.117	15.991	15.869
29	13.474	14.083	14.555	15.076	15.442	15.676	15.919	15.939	15.925	15.856	15.801
30	13.402	13.980	14.416	14.903	15.247	15.465	15.709	15.743	15.765	15.742	15.741
31	13.336	13.885	14.292	14.749	15.070	15.282	15.527	15.578	15.624	15.640	15.702
32	13.291	13.831	14.219	14.658	14.966	15.168	15.415	15.475	15.537	15.588	15.668
33	13.240	13.750	14.140	14.550	14.850	15.019	15.280	15.382	15.451	15.520	15.645
34	13.200	13.680	14.050	14.440	14.720	14.900	15.145	15.283	15.379	15.459	15.642
35	13.152	13.609	13.961	14.349	14.602	14.793	15.043	15.157	15.283	15.419	15.681
36	13.116	13.592	13.912	14.297	14.552	14.746	15.000	15.098	15.237	15.415	15.790

Probe 4

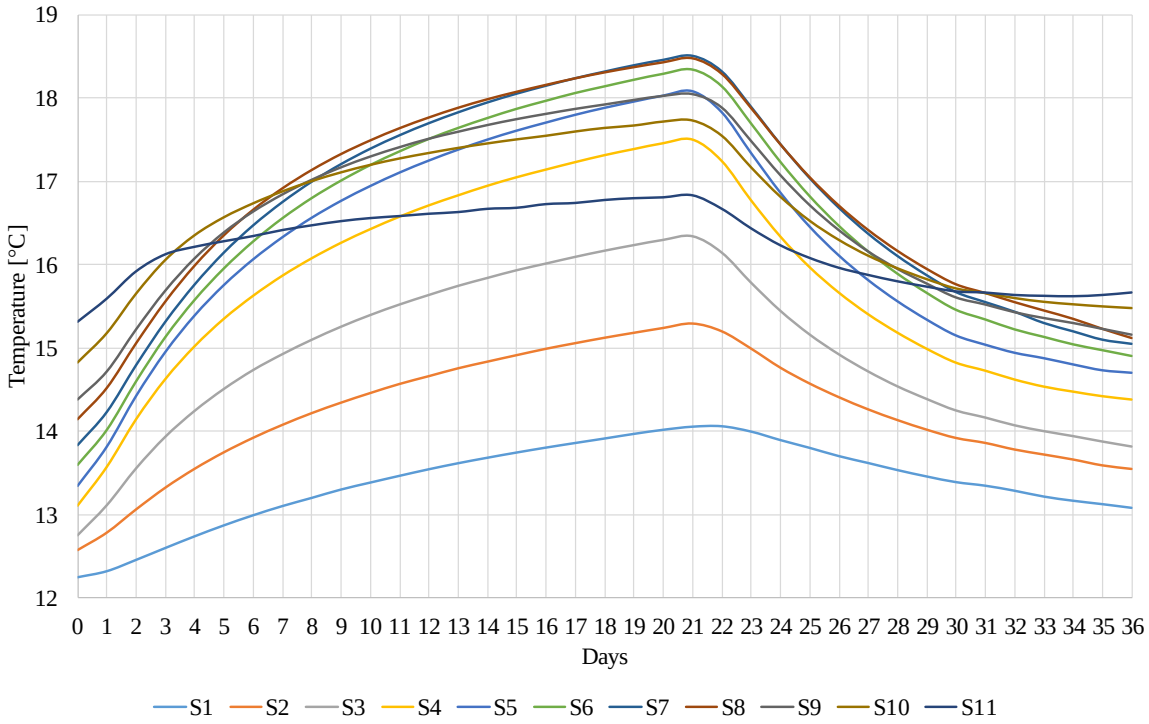

Figure C-7. Temperature profiles for the thermal sensors the monitoring borehole during the experiment time, 21 days of heating and 15 days of cooling.

The temperature for each sensor is reported in Table as, *Initial* at $t = 0$, *Final* at $t = 36$. *Gained* is the difference between $Final - Initial$, and *Max* is the maximum temperature recorded, corresponding to the last day of heating (day 21).

Table C-3. Temperatures [°C] measured at the sensors during the experiment duration – Probe 4

	Initial	Final	Gained	Max
S1	12.254	13.085	0.831	14.062
S2	12.570	13.542	0.972	15.284
S3	12.754	13.820	1.066	16.345
S4	13.107	14.380	1.273	17.497
S5	13.344	14.700	1.356	18.074
S6	13.590	14.900	1.310	18.344
S7	13.837	15.050	1.213	18.499
S8	14.147	15.120	0.973	18.469
S9	14.382	15.160	0.778	18.046
S10	14.828	15.480	0.652	17.729
S11	15.309	15.660	0.351	16.825

The same correction performed for the missing values in the records of Probe 3 was made for Probe 4. Different from Probe 3, Probe 4 only stopped recording in the last days of the experiment, reason why it was used as example of the trend for the values missing of the temperature profiles in P3. Table highlights the adjusted values.

Table C-4. Records for each sensor in the Probe 4 inside the monitoring borehole

Days	S1	S2	S3	S4	S5	S6	S7	S8	S9	S10	S11
0	12.254	12.570	12.754	13.107	13.344	13.590	13.837	14.147	14.382	14.828	15.309
1	12.326	12.779	13.115	13.573	13.815	14.012	14.234	14.523	14.719	15.181	15.587
2	12.462	13.058	13.558	14.144	14.422	14.595	14.795	15.057	15.224	15.653	15.914
3	12.604	13.318	13.938	14.626	14.950	15.128	15.315	15.557	15.689	16.057	16.118
4	12.744	13.544	14.249	15.019	15.387	15.575	15.761	15.987	16.076	16.354	16.208
5	12.875	13.742	14.512	15.349	15.752	15.954	16.144	16.350	16.387	16.569	16.275
6	12.996	13.916	14.739	15.625	16.060	16.278	16.469	16.656	16.638	16.736	16.337
7	13.106	14.071	14.930	15.865	16.325	16.557	16.748	16.912	16.843	16.879	16.409
8	13.204	14.211	15.102	16.074	16.558	16.799	16.992	17.132	17.019	17.002	16.466
9	13.304	14.336	15.259	16.259	16.761	17.009	17.202	17.323	17.168	17.107	16.516
10	13.388	14.452	15.399	16.423	16.939	17.196	17.387	17.486	17.297	17.197	16.552
11	13.469	14.560	15.526	16.573	17.100	17.361	17.548	17.632	17.410	17.274	16.577
12	13.547	14.654	15.640	16.708	17.244	17.510	17.693	17.760	17.511	17.339	16.604
13	13.619	14.748	15.749	16.828	17.375	17.642	17.822	17.877	17.595	17.400	16.624
14	13.685	14.827	15.845	16.943	17.495	17.762	17.941	17.979	17.675	17.454	16.663
15	13.747	14.905	15.938	17.046	17.602	17.872	18.046	18.068	17.746	17.502	16.676
16	13.806	14.981	16.018	17.138	17.699	17.969	18.141	18.151	17.809	17.545	16.720
17	13.861	15.049	16.098	17.227	17.792	18.063	18.231	18.229	17.869	17.597	16.734
18	13.915	15.113	16.172	17.310	17.875	18.142	18.310	18.300	17.921	17.639	16.769
19	13.970	15.173	16.239	17.383	17.951	18.222	18.385	18.363	17.976	17.668	16.791
20	14.019	15.230	16.301	17.453	18.022	18.293	18.450	18.421	18.025	17.716	16.801
21	14.057	15.284	16.345	17.497	18.074	18.344	18.499	18.469	18.046	17.729	16.825
22	14.062	15.191	16.149	17.241	17.823	18.144	18.314	18.284	17.885	17.547	16.664
23	13.998	14.984	15.789	16.770	17.335	17.697	17.890	17.875	17.485	17.168	16.430
24	13.897	14.756	15.451	16.336	16.861	17.236	17.444	17.441	17.076	16.816	16.227
25	13.803	14.566	15.166	15.968	16.453	16.824	17.036	17.048	16.716	16.528	16.075
26	13.705	14.402	14.927	15.662	16.106	16.466	16.680	16.706	16.415	16.297	15.956
27	13.622	14.256	14.722	15.403	15.811	16.157	16.369	16.414	16.159	16.108	15.870
28	13.537	14.128	14.543	15.182	15.558	15.890	16.103	16.164	15.950	15.957	15.794
29	13.461	14.013	14.391	14.989	15.338	15.659	15.872	15.948	15.774	15.827	15.730
30	13.393	13.913	14.253	14.822	15.147	15.455	15.670	15.763	15.607	15.715	15.673
31	13.350	13.854	14.168	14.726	15.037	15.339	15.550	15.659	15.522	15.660	15.659
32	13.290	13.775	14.075	14.620	14.940	15.220	15.435	15.550	15.430	15.600	15.630
33	13.220	13.715	14.005	14.535	14.875	15.130	15.300	15.450	15.360	15.555	15.620
34	13.170	13.655	13.945	14.475	14.800	15.040	15.200	15.350	15.300	15.525	15.615
35	13.129	13.585	13.880	14.420	14.730	14.970	15.100	15.230	15.230	15.500	15.630
36	13.085	13.542	13.820	14.380	14.700	14.900	15.050	15.120	15.160	15.480	15.660

Fluid temperature (inlet & outlet)

The digital thermal sensors installed at the inlet and outlet points recorded the temperature of the running water every 30 seconds. Due to the large amount of lines generated, the records were averaged in days, to evaluate the temperature during the heating period.

Additionally, the temperature was averaged in hours, for a better comparison with the data from the modelling part.

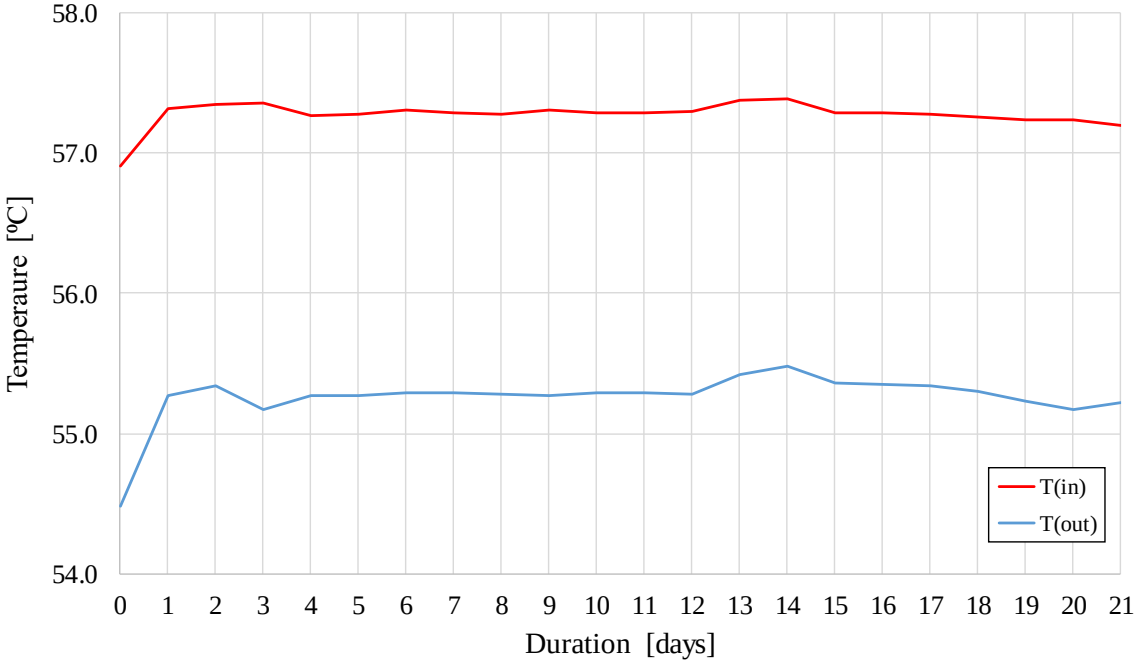

Figure C-3. Temperature for the carrier fluid at the inlet and outlet sensors. Averaged in days.

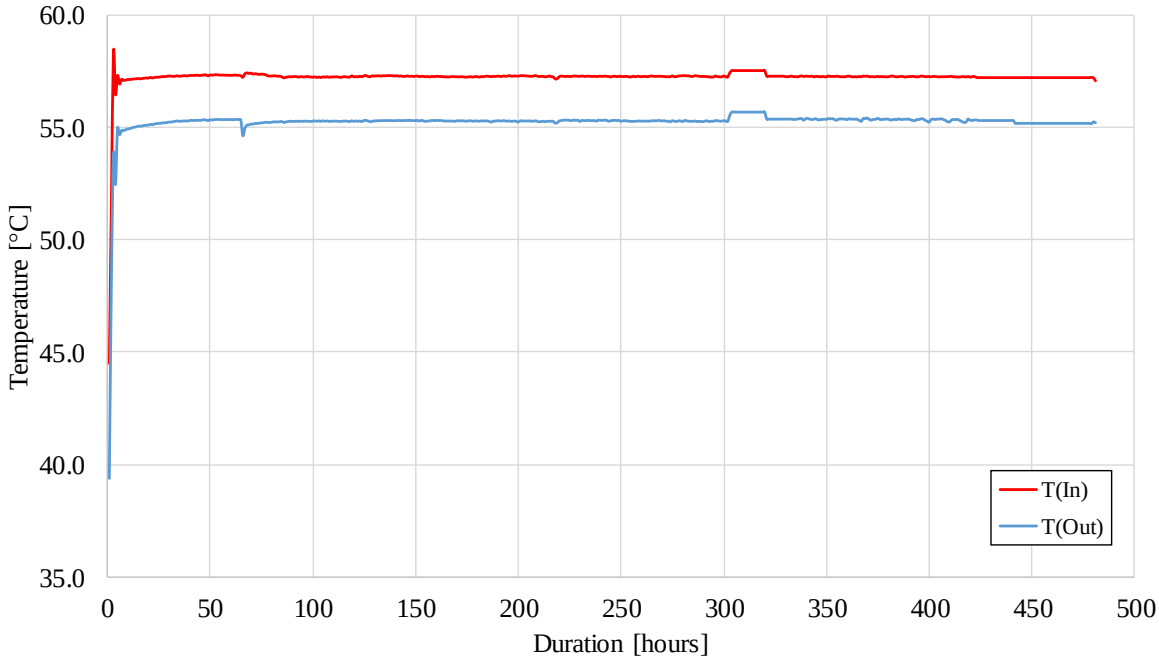

Figure C-4. Temperature for the carrier fluid at the inlet and outlet sensors. Averaged in hours.

Flow rate

The flow rate in the loop was measure using and a flow meter equipped with a pulse counter. The calibration from factory returned 1 L/h every 77 pulses.

The pulses were transformed into digital data with the use of an Arduino® board and the visualization and recording code controlled by a Raspberry Pi® Board.

The flow rate presented a decreasing behavior after the first 100 hours of circulating the carrier fluid, maintaining a small variation for the rest of the time until the 400 hours when the fluctuation in the flow seemed to be increased.

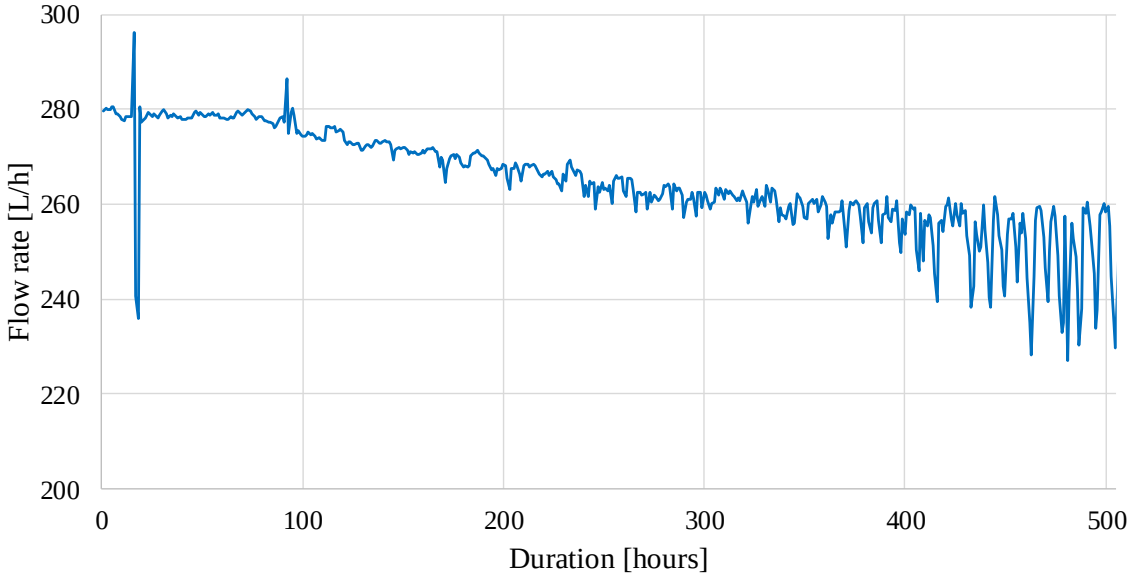

Figure C-5. System's flow rate as recorded by the flow meter.

Appendix D – Numerical modeling results

Table D-1. Models input parameters

Name	Expression	Value	Units	Description and source
alpha_ground	7e-6[1/K]	7.00E-06	1/K	Thermal expansion coefficient of rock
k_ground	2.87[W/(m*K)]	2.872	W/(m*K)	Thermal conductivity (ground) Average value for tunnel rock samples - Lab tested
rho_ground	2504.3[kg/m^3]	2 504.32	kg/m^3	Density (ground) Average value for tunnel rock samples - Measured
Cp_ground	723.5[J/(kg*K)]	723.50	J/(kg*K)	Heat capacity (ground) Calculated from the lab values
nu_ground	0.25	0.25		Poisson's ratio (ground) – Literature
E_ground	60e9[Pa]	6.00E+10	Pa	Young modulus (ground) – Literature
h_l	0.05[m]	0.05	m	BHE elements length
L	5[m]	5.0	m	BHE length
alpha	0.3	0.3		Diffusion term
a	k_ground/ (rho_ground*Cp_ground)	1.584E-06	m^2/s	Thermal diffusivity (ground) Average value for tunnel rock samples - Lab tested
A_p	pi*r_i^2	2.0106E-04	m^2	Area of inside pipe
A_g	pi*r_b^2-2*pi*r_o^2	0.008364	m^2	Area of grout
S_p	pi*2*r_i	0.050265	m	Circumference inside pipe
S_g	2*pi*r_b	0.336150	m	Circumference of grout
b_ig2	58[W/(m^2*K)]	58	W/(m^2*K)	1/Thermal resistance inside pipe to grout
b_sg2	15[W/(m^2*K)]	15	W/(m^2*K)	1/Thermal resistance grout to soil
k_grout	1.7[W/(m*K)]	1.7	W/(m*K)	
r_max	10[m]	10	m	
r_i	16[mm]/2	0.008	m	radius pipe inner
r_o	20[mm]/2	0.010	m	radius pipe outer
r_b	107[mm]/2	0.0535	m	radius borehole
k_pipe	0.4[W/(m*K)]	0.4	W/(m*K)	
r_eq	sqrt(2*r_i^2)	0.011314	m	Equivalent grout inner radius
R_cond_pipe_Al_Khoury	r_o*log(r_o/r_i)/k_pipe	0.005579	K·m^2/W	log=ln
R_cond_grout	r_b*log(r_b/r_eq)/k_grout	0.048895	K·m^2/W	
R_cond_pipe	log(r_o/r_i)/(k_pipe*2*pi)	0.088786	s^3·K/(kg·m)	
rho_ref	988[kg/m^3]	988	kg/m^3	Density (water) http://www.engineeringtoolbox.com/water-thermal-properties-d_162.html
Cp_ref	4180[J/(kg*K)]	4 180	J/(kg*K)	Heat capacity (water) http://www.engineeringtoolbox.com/water-thermal-properties-d_162.html
Pr_ref	3.56	3.56		Prandtl number (water) http://www.engineeringtoolbox.com/water-thermal-properties-d_162.html
v_ref	0.553*10^-6[m^2/s]	5.53E-07	m^2/s	Kinematic viscosity (water) http://www.engineeringtoolbox.com/water-thermal-properties-d_162.html
k_ref	0.64[W/(m*K)]	0.64	W/(m*K)	
L_extra	10[m]	10	m	
b_depth	t_depth+b_floor_MOBH	-10.34	m	z-coordinate of the borehole
z_surface	10.9[m]	10.90	m	z-coordinate of the ground surface above tunnel
b_floor_MOBH	1.46[m]	1.46	m	Distance from tunnel floor to MOBH
t_height	3.3[m]	3.30	m	Tunnel height
t_width	2.6[m]	2.60	m	Tunnel width
t_length	50[m]	50	m	Tunnel length
t_length2	30[m]	30	m	Tunnel 2 length
t_depth	-8.5-t_height	-11.80	m	Tunnel floor depth
depth	20[m]	20	m	Block depth below tunnel
width	L+L_extra+t_width+15	32.6	m	Block width
height	20[m]	20	m	Block height
moni_dist	0.935[m]	0.935	m	Distance between BHE and MOBH

Appendices

hf	37[mW/m^2]	0.037	W/m^2	heat flux
Tair	5.8[degC]	278.95	K	Yearly average air temperature in Helsinki http://en.ilmatieteenlaitos.fi/statistics-from-1961-onwards
GST	(0.71*SAT+2.93)[degC]	280.20	K	Mean surface ground temperature
SAT	Tair[1/degC]	5.8		Ground surface temperature
gradT	0.0112[K/m]	0.0112	K/m	Geothermal gradient mean surface ground temperature https://www.geothermal-energy.org/pdf/IGAstandard/WGC/2000/R0778.PDF
deltaGST	(GSTmax-GSTmin)/2	8.35	K	
GSTmin	-2[degC]	271.15	K	Minimum yearly ground surface temperature
T_tunnel	15[degC]	288.15	K	Tunnel air temperature
GSTmax	14.7[degC]	287.85	K	Maximum yearly ground surface temperature
GSTave	6.1[degC]	279.25	K	Mean yearly ground surface temperature
P	31536000[s]	3.1536E+07	s	Period; 1 year in seconds
pipe_dist	4[cm]	0.04	m	Distance between pipes in BHE
rho_grout	1925.7[kg/m^3]	1 925.70	kg/m^3	Density (grout) Average value from samples - Laboratory measured
Cp_grout	750[J/(kg*K)]	750	J/(kg*K)	
flowrate	0.07352[L/s]	7.352E-05	m^3/s	Pump flowrate
v	flowrate/A_p	0.36566	m/s	Fluid velocity
flowspeed	v	0.36566	m/s	
hB	L*tan(12[deg])	1.06278	m	
hBm	(L+0.3)*tan(12[deg])	1.12655	m	
hBp	(L-0.2)*tan(12[deg])	1.02027	m	
s12	0[m]	0	m	
s11	0.180[m]	0.18	m	Depth of sensor 11
s10	0.690[m]	0.69	m	Depth of sensor 10
s9	1.28[m]	1.28	m	Depth of sensor 9
s8	1.71[m]	1.71	m	Depth of sensor 8
s7	2.22[m]	2.22	m	Depth of sensor 7
s6	2.73[m]	2.73	m	Depth of sensor 6
s5	3.22[m]	3.22	m	Depth of sensor 5
s4	3.77[m]	3.77	m	Depth of sensor 4
s3	4.26[m]	4.26	m	Depth of sensor 3
se2	4.77[m]	4.77	m	Depth of sensor 2
se1	5.275[m]	5.275	m	Depth of sensor 1
moni_dist_toe	1.192[m]	1.192	m	Distance between boreholes toes

Table D-2. Models results. Temperature simulated at the sensors location in the monitoring borehole

Scenario			S1	S2	S3	S4	S5	S6	S7	S8	S9	S10	S11
HTiP Model	A	Initial	12.072	12.252	12.448	12.653	12.912	13.175	13.487	13.848	14.195	14.743	15.266
		Final (15)	13.913	14.322	14.718	15.065	15.403	15.651	15.852	16.002	16.095	16.194	16.274
		Final (45)	12.819	13.017	13.222	13.426	13.664	13.888	14.137	14.412	14.670	15.078	15.487
		Gain	0.747	0.764	0.774	0.773	0.752	0.713	0.650	0.564	0.475	0.335	0.221
		Max	15.625	16.833	17.882	18.656	19.294	19.702	19.991	20.140	20.126	19.773	18.964
	B	Initial	12.054	12.213	12.394	12.591	12.842	13.098	13.403	13.754	14.093	14.634	15.175
		Final	13.337	13.701	14.062	14.392	14.729	14.995	15.234	15.441	15.598	15.807	16.001
		Gain	1.283	1.488	1.668	1.801	1.887	1.897	1.831	1.687	1.505	1.173	0.826
		Max	14.719	15.802	16.779	17.505	18.123	18.548	18.894	19.141	19.242	19.087	18.480
	C	Initial	12.072	12.253	12.448	12.653	12.912	13.175	13.488	13.848	14.195	14.743	15.266
		Final	13.067	13.394	13.724	14.032	14.357	14.623	14.878	15.114	15.307	15.580	15.841
		Gain	0.994	1.142	1.276	1.379	1.445	1.448	1.390	1.266	1.112	0.837	0.575
		Max	14.350	15.388	16.319	17.010	17.605	18.028	18.393	18.681	18.832	18.769	18.257
WFE Model	A	Initial	12.205	12.377	12.564	12.761	13.010	13.262	13.561	13.906	14.238	14.767	15.279
		Final (15)	13.599	13.953	14.299	14.611	14.927	15.174	15.396	15.586	15.727	15.910	16.075
		Final (45)	12.719	12.906	13.103	13.303	13.540	13.766	14.021	14.306	14.576	15.005	15.437
		Gain	0.514	0.529	0.539	0.542	0.530	0.504	0.460	0.400	0.338	0.238	0.158
		Max	14.914	15.882	16.732	17.367	17.912	18.293	18.597	18.796	18.856	18.690	18.165
	B	Initial	12.190	12.345	12.521	12.712	12.955	13.202	13.494	13.832	14.159	14.683	15.209
		Final	13.113	13.413	13.716	13.999	14.303	14.557	14.805	15.042	15.241	15.528	15.805
		Gain	0.923	1.068	1.195	1.287	1.348	1.355	1.311	1.210	1.082	0.845	0.596
		Max	14.23	15.10	15.89	16.49	17.02	17.41	17.76	18.03	18.18	18.16	17.79
	C	Initial	12.205	12.376	12.564	12.760	13.009	13.262	13.561	13.905	14.238	14.767	15.279
		Final	12.941	13.223	13.511	13.785	14.085	14.342	14.602	14.857	15.077	15.401	15.715
		Gain	0.736	0.847	0.947	1.025	1.076	1.081	1.041	0.952	0.839	0.634	0.436
		Max	13.92	14.75	15.50	16.07	16.57	16.96	17.32	17.63	17.82	17.88	17.59

Weak Edge Form – Scenarios results

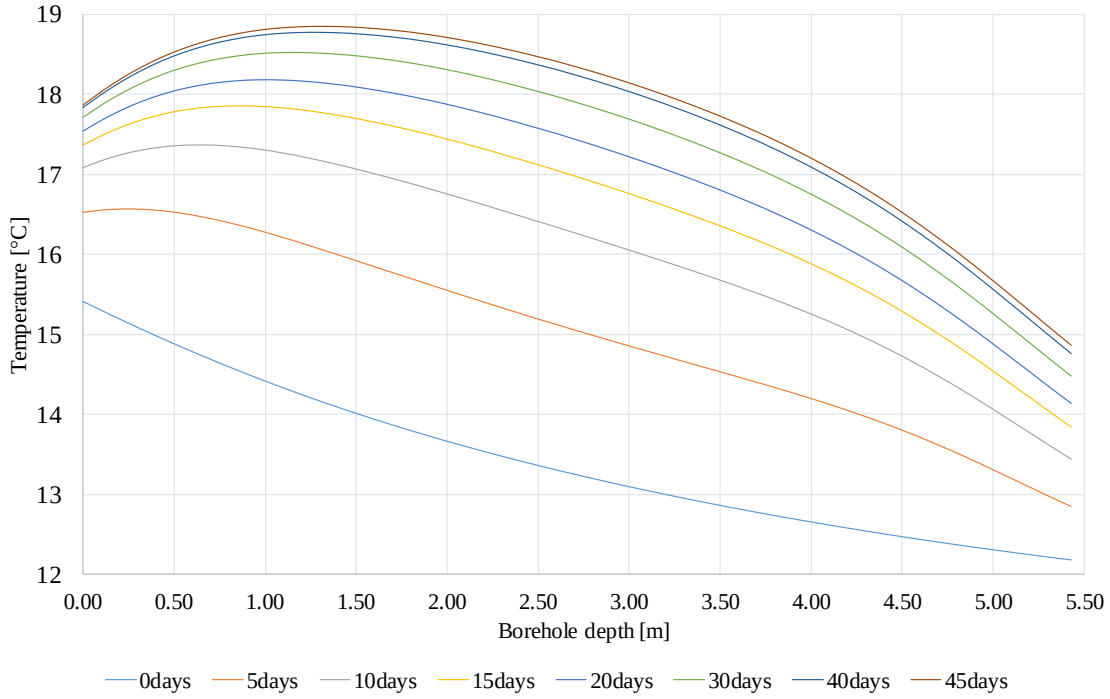

Figure D-1. WFE – Simulated temperature along the MOBH after heating phase. Time increment of 5 days.

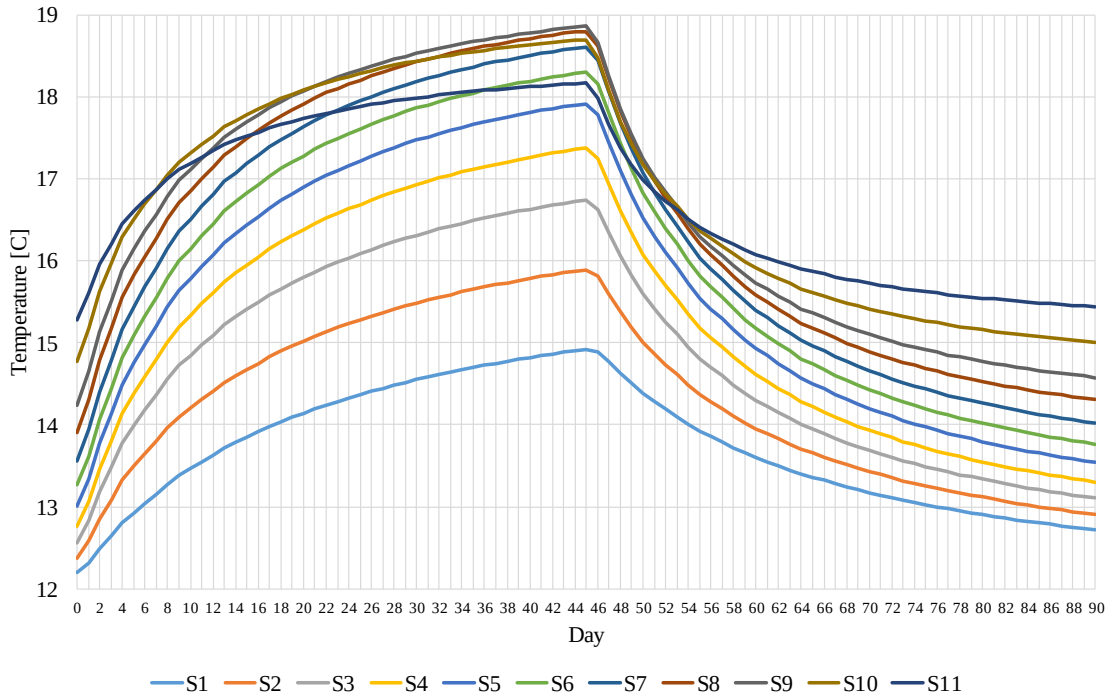

Figure D-2. Simulated sensors readings for Scenario A - WFE

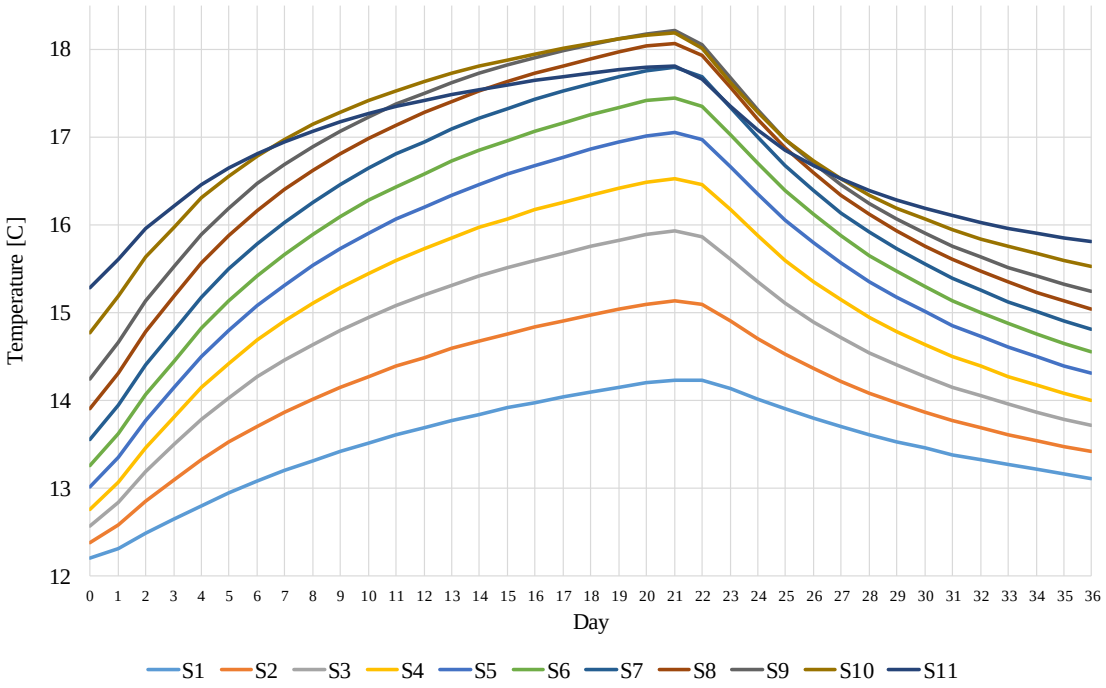

Figure D-3. Simulated sensors readings for Scenario B – WFE

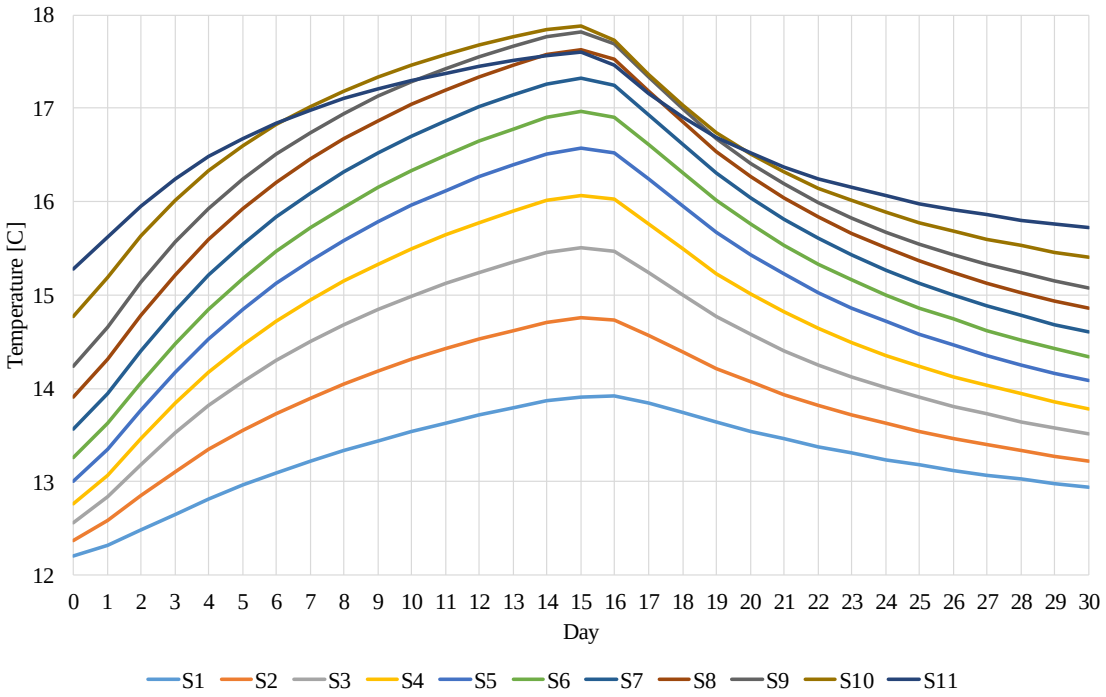

Figure D-4. Simulated sensors readings for Scenario C – WFE

Heat Transfer in Pipes – Scenarios results

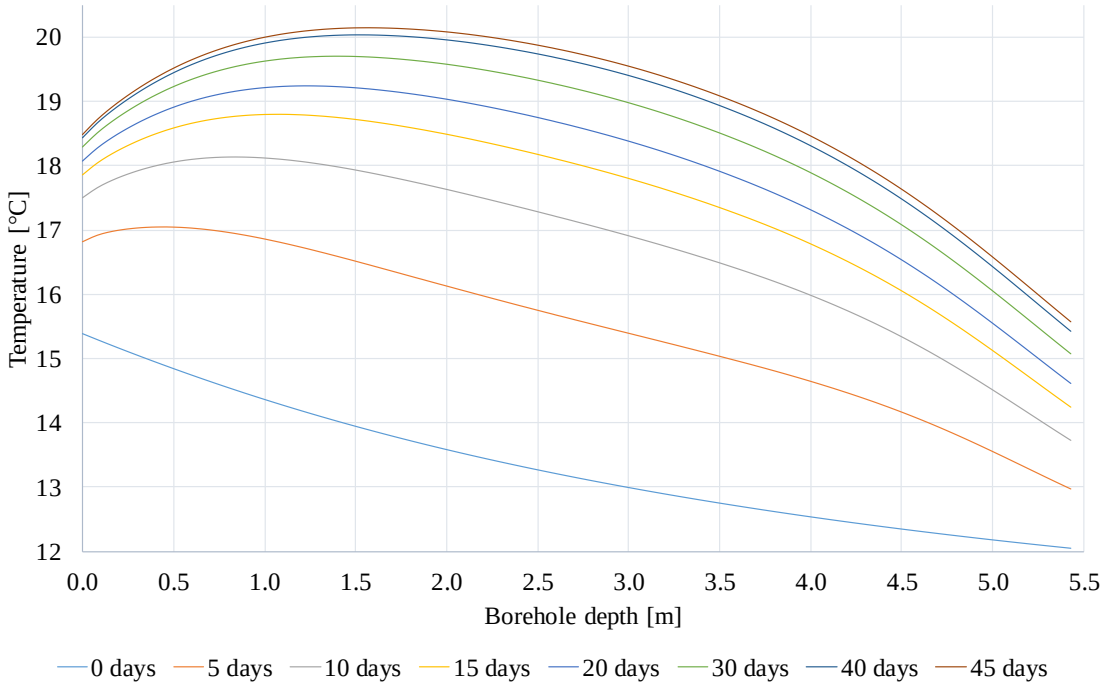

Figure D-5. HTiP –Simulated temperature along the MOBH after heating phase. Time increment of 5 days.

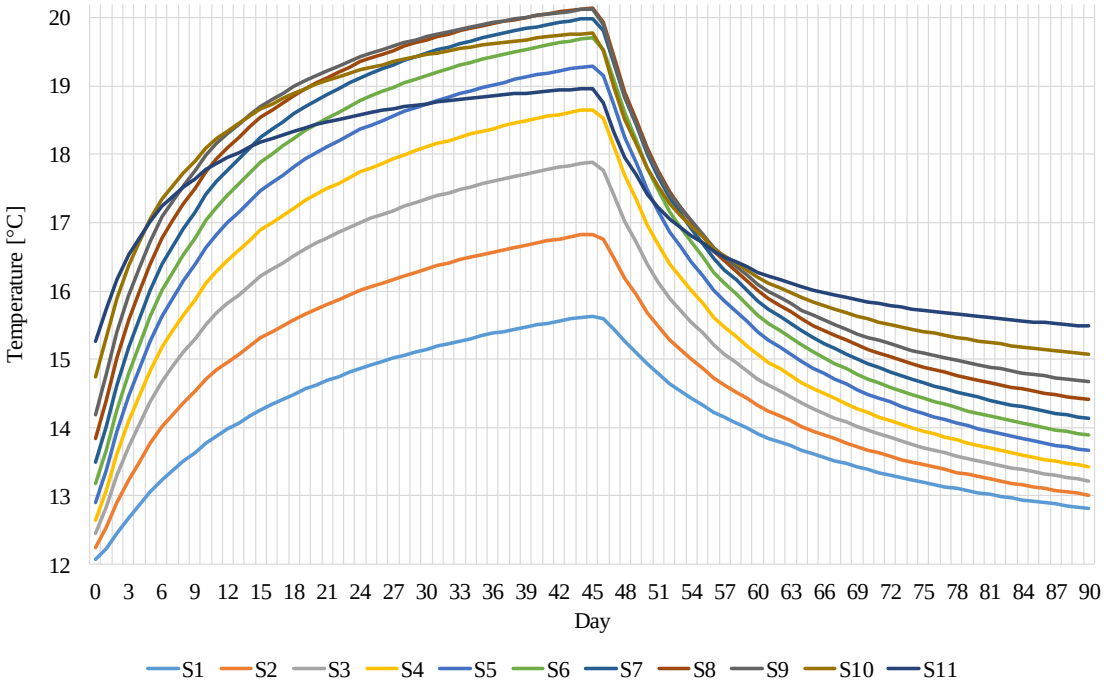

Figure D-6. Simulated sensors readings for Scenario A - HTiP

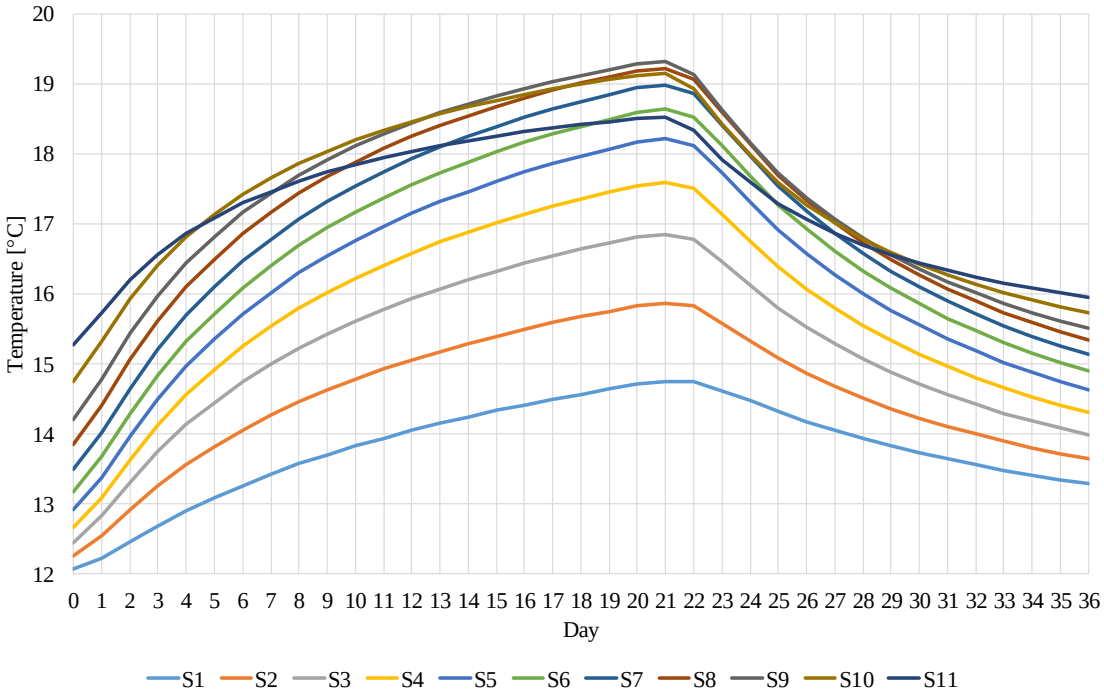

Figure D-7. Simulated sensors readings for Scenario B – HTiP

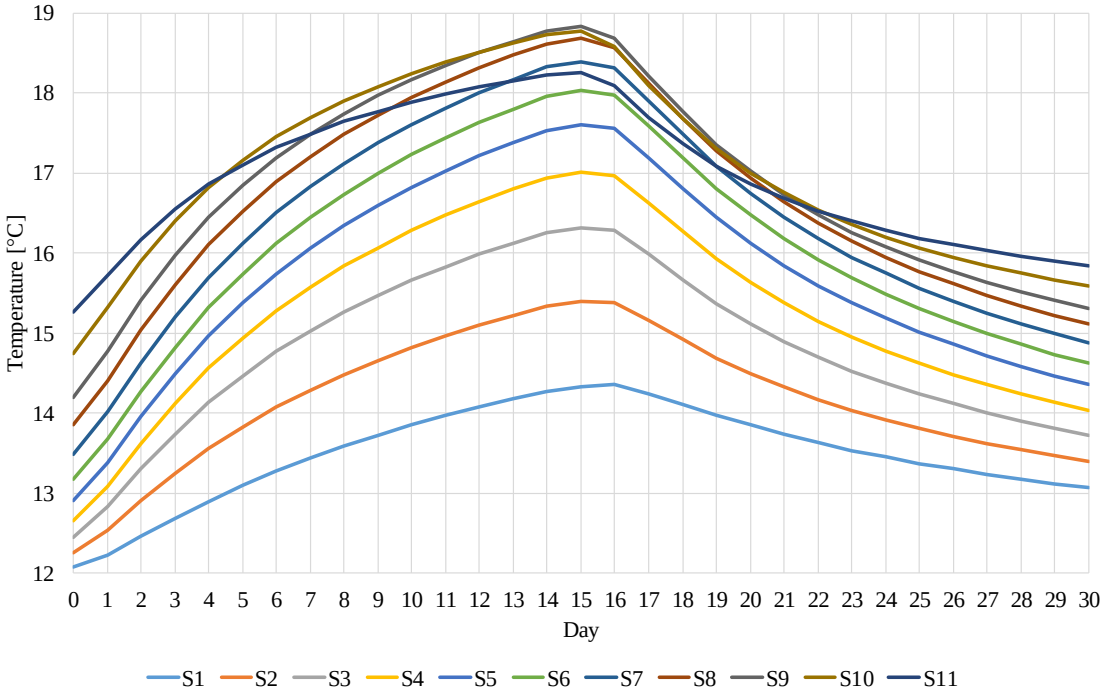

Figure D-8. Simulated sensors readings for Scenario C - HTiP

Appendices

Appendix E – Thermal Conductivity Scan results

Three samples of the two rock types identified in the boreholes were analyzed in laboratory to estimate the thermal conductivity and diffusivity of these rocks. The laboratory testing consisted in the optical scanning of rock's surface with a Thermal Conductivity Scanning (TCS) with the support of the Geophysics department of the University of Helsinki.

The laboratory test was done to assess the thermal properties homogeneity in the boreholes and determine if it was necessary to change the BHE and monitoring boreholes location. From the results obtained in the TCS test (Table E-2 & E-3), is observable that both rock types have similar thermal parameters (conductivity and diffusivity). It can be interpreted that there is no need to modify the boreholes BHE location.

The samples came from rocks extracted from the same wall where the experiment takes place with similar characteristics to the host rocks present in the boreholes and identified in the video surveys, not from core drillings in the boreholes location. Three gneiss and three granite samples and were prepared by sawing cubes from the rocks obtained, from which three faces were scanned. The samples were analyzed in a completely dry state.

Table E-1. Samples physical properties.

Sample	Rock type	Weight [kg]	Volume [x10^{-3} m^3]	Density [kg/m^3]	ρ_{ave}
SCC1	Gneiss	0.396	0.150	2,641.667	*2,501.431*
SCC2	Gneiss	1.060	0.400	2,648.775	
SCC3	Gneiss	0.443	0.200	2,213.850	
SCC4	Granite	0.478	0.200	2,392.100	*2,507.200*
SCC5	Granite	0.787	0.300	2,622.100	
SCC6	Granite	0.878	0.350	2,507.400	
A	Grout	1.844	0.950	1,940.989	*1,925.702*
B	Grout	1.891	0.990	1,910.414	

For the **gneiss**, λ_{mean} is **2.774 W/mK**, while for the **granite** the value is **2.971 W/mK**. These values are lower than the average reported by GTK in its report (2016); however, is necessary to consider the reported value comes from a much larger sample and with a different method for only one rock type identified, granite.

Table E-2. TCS results for gneiss samples.

Gneiss Direction	λ_{ave} [W/mK]	α_{ave} [x10^{-6} m^2/s]
1	3,076	1,621
2	2,704	1,264
3	2,541	1,468
Overall	**2,774**	**1,451**

Table E-3. TCS results for granite smaples.

Granite Direction	λ_{ave} [W/mK]	α_{ave} [x10^{-6} m^2/s]
1	3,012	1,611
2	3,033	1,599
3	2,868	1,544
Overall	**2,971**	**1,585**

Thermal Conductivity Scanning principle

The scanning of the sample occurs in steps along the length of it and perpendicular to the heating source and sensors movement direction. Figure E-1 schematizes the previous description. Here a rock sample is represented as prepared for the thermal scan.

The faces to be scanned are selected according to the sample foliation visible on each of the cube faces, and the desired scan direction with respect to the foliation.

1. Parallel to foliation,
2. Perpendicular to foliation and,
3. Normal to foliation plane.

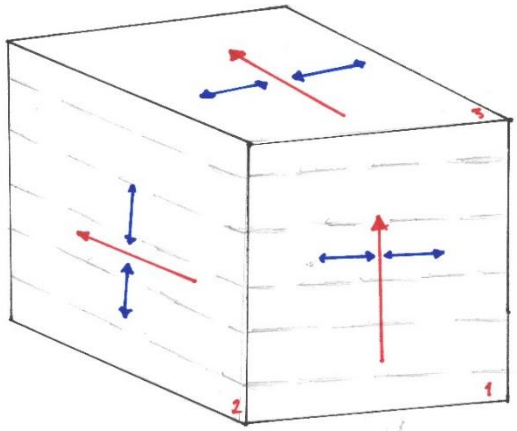

Figure E-1. Schematization of rock sample with scan directions.

The red arrows represent the direction in which the heat source and sensors are moving along the machine, while the blue arrows represent the portion of rock from which the information is acquired.

The TCS is a high precision noncontact method using optical scanning developed by Prof. Dr. Yuri Popov (Moscow State Geological Prospecting Academy). The theoretical model is based on scanning a sample surface with a focused, mobile, and continuously operated heat source in combination with infrared temperature sensors (Lippmann & Rauen GbR, 2017).

The emitted light and heat emission is focused on the surface of the sample, leading to its heating. Two infrared temperature sensors (cold and hot) are installed at a defined distance to the heat source. These sensors measure the temperature of the sample before and after the heating. By comparison with known standards λ can be determined (TU Darmstadt, 2017).

TCS can:

- Observe and quantify mean and local values of the thermal properties (λ & α) and inhomogeneity factors.
- Observe small-scale profiles of thermal properties along scanning lines.
- Calculate automatically mean values and quality factors.
- On anisotropic solids, observation of components of the thermal properties tensor.

The results are:

- measurement of sample's thermal conductivity and thermal diffusivity
- profiles of thermal properties along the samples
- inhomogeneity of thermal properties
- anisotropy: components of the thermal properties tensor for anisotropic solids

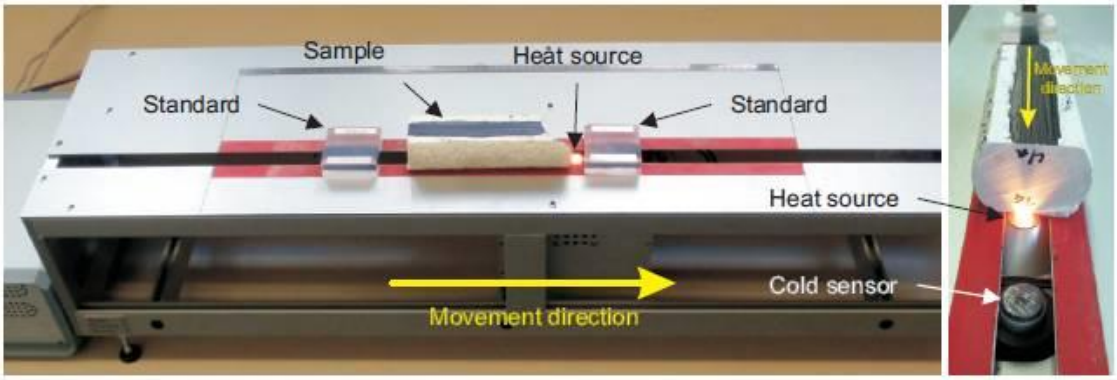

Figure E-2. Thermal Conductivity Scanner apparatus and components (TU Darmstadt, 2017)

Each defined face of the cubes was scanned with this apparatus. The TCS records the temperature along the scanned face and returns three temperature profiles, one for each of the sensors. The results of the rock's scan are compared against the results of the standards to calculate the rock thermal properties. Thus, the used of known materials and their properties is necessary. Two standards were used for the SCC samples scan.

Table E-4. TSC standards properties

Standard	Material	λ [W/mK]	α [mm²/s]
B2	Quartz	1,35	0,85
D1	Platinum	6,35	2,76

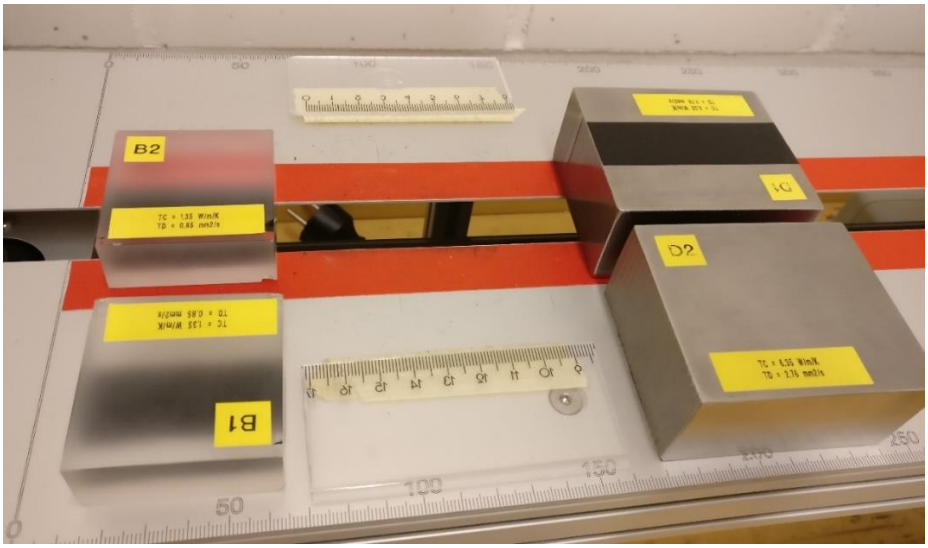

Figure E-3. Standards used in lab test (left, quartz; right, platinum) rock sample rest between the standards.

Once the TCS generates these profiles, is necessary to determine the distance range to be analyzed for each material to obtain the thermal conductivity in that direction (λ_i). This step also allows cutting out of the analysis the effects produced at the corner of the sample. Figure E-3 shows the two standards used for the tests, while Figure E-4 shows the measurements on sample SCC-1 (hornblende biotite Gneiss) for the face marked as direction 1 (parallel to rock's foliation) at the limits. To improve the thermal reading, a thin-2cm-black stripe is painted on each surface to be scanned; this step reduces the reflection on the rocks surface for a more accurate result.

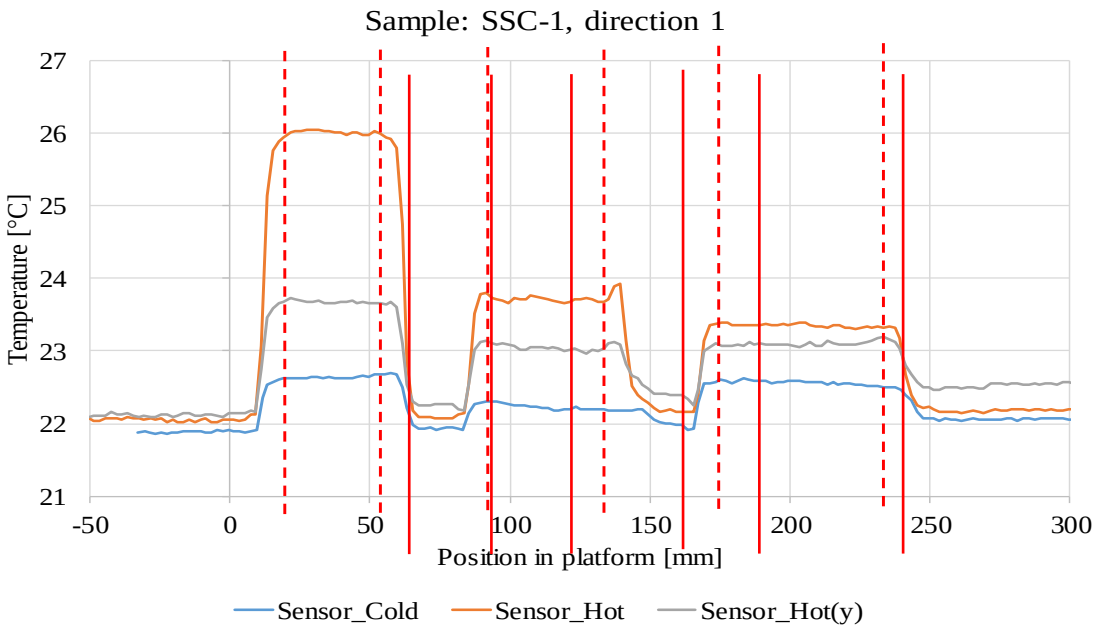

Figure E-4. Example of temperature profiles in the TSC test for SCC-1_1 and example of corner effects.

Table E-5. Overall thermal conductivity and diffusivity for the rock samples

Rock	Sample	Thermal conductivity [W/mK]			Thermal diffusivity [x10^{-6} m^2/s]		
		λ_{ave}	λ_{min}	λ_{max}	α_{ave}	α_{min}	α_{max}
hbb-Gneiss	SCC-1	2,845	2,672	2,988	1,393	1,255	1,566
	SCC-2	2,790	2,500	2,976	1,473	1,261	1,659
	SCC-3	2,686	2,512	2,869	1,485	1,329	1,614
	Total	***2,774***	2,561	2,944	***1,451***	1,282	1,613
Granite	SCC-4	2,942	2,673	3,194	1,576	1,315	1,912
	SCC-5	2,889	2,465	3,356	1,584	1,255	1,910
	SCC-6	3,082	2,754	3,508	1,593	1,378	1,832
	Total	***2,971***	2,631	3,353	***1,585***	1,316	1,884

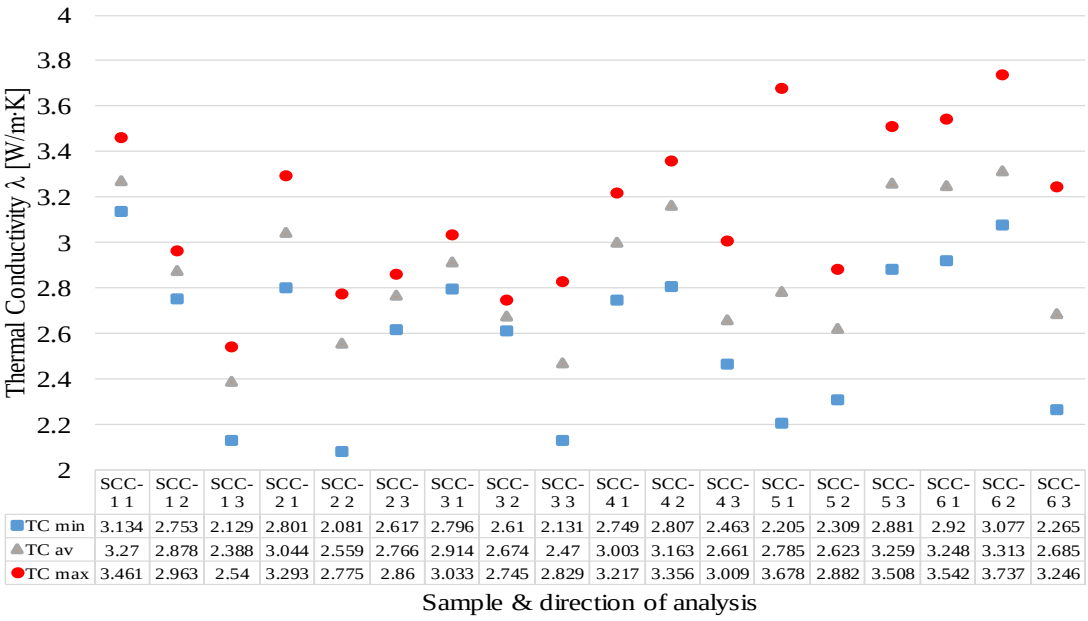

	SCC-11	SCC-12	SCC-13	SCC-21	SCC-22	SCC-23	SCC-31	SCC-32	SCC-33	SCC-41	SCC-42	SCC-43	SCC-51	SCC-52	SCC-53	SCC-61	SCC-62	SCC-63
TC min	3.134	2.753	2.129	2.801	2.081	2.617	2.796	2.61	2.131	2.749	2.807	2.463	2.205	2.309	2.881	2.92	3.077	2.265
TC av	3.27	2.878	2.388	3.044	2.559	2.766	2.914	2.674	2.47	3.003	3.163	2.661	2.785	2.623	3.259	3.248	3.313	2.685
TC max	3.461	2.963	2.54	3.293	2.775	2.86	3.033	2.745	2.829	3.217	3.356	3.009	3.678	2.882	3.508	3.542	3.737	3.246

Figure E-5. Thermal Conductivity (max, min, and average) for the six samples with the TCS.

Table E-6. Thermal conductivity and diffusivity for the samples by direction of scanning.

Direction	Sample	Thermal conductivity [W/mK]		Thermal diffusivity [x10^{-6} m^2/s]			
		λ_{ave}	λ_{min}	λ_{ave}	λ_{min}	λ_{ave}	λ_{min}
1	**Gneiss**	**3,076**	2,910	3,262	**1,621**	1,462	1,781
	SCC-1	3,270	3,134	3,461	1,746	1,533	1,991
	SCC-2	3,044	2,801	3,293	1,581	1,383	1,741
	SCC-3	2,914	2,796	3,033	1,535	1,471	1,612
	Granite	**3,012**	2,625	3,479	**1,611**	1,335	2,020
	SCC-4	3,003	2,749	3,217	1,585	1,334	1,890
	SCC-5	2,785	2,205	3,678	1,580	1,200	2,197
	SCC-6	3,248	2,920	3,542	1,668	1,472	1,972
2	**Gneiss**	**2,704**	2,481	2,828	**1,264**	1,083	1,457
	SCC-1	2,878	2,753	2,963	1,170	1,086	1,315
	SCC-2	2,559	2,081	2,775	1,229	0,867	1,523
	SCC-3	2,674	2,610	2,745	1,392	1,297	1,534
	Granite	**3,033**	2,731	3,325	**1,599**	1,371	1,806
	SCC-4	3,163	2,807	3,356	1,667	1,395	2,007
	SCC-5	2,623	2,309	2,882	1,351	1,174	1,487
	SCC-6	3,313	3,077	3,737	1,779	1,543	1,923
3	**Gneiss**	**2,541**	2,292	2,743	**1,468**	1,299	1,600
	SCC-1	2,388	2,129	2,540	1,264	1,146	1,393
	SCC-2	2,766	2,617	2,860	1,610	1,532	1,713
	SCC-3	2,470	2,131	2,829	1,529	1,219	1,695
	Granite	**2,868**	2,536	3,254	**1,544**	1,242	1,828
	SCC-4	2,661	2,463	3,009	1,477	1,215	1,838
	SCC-5	3,259	2,881	3,508	1,822	1,392	2,045
	SCC-6	2,685	2,265	3,246	1,332	1,118	1,601

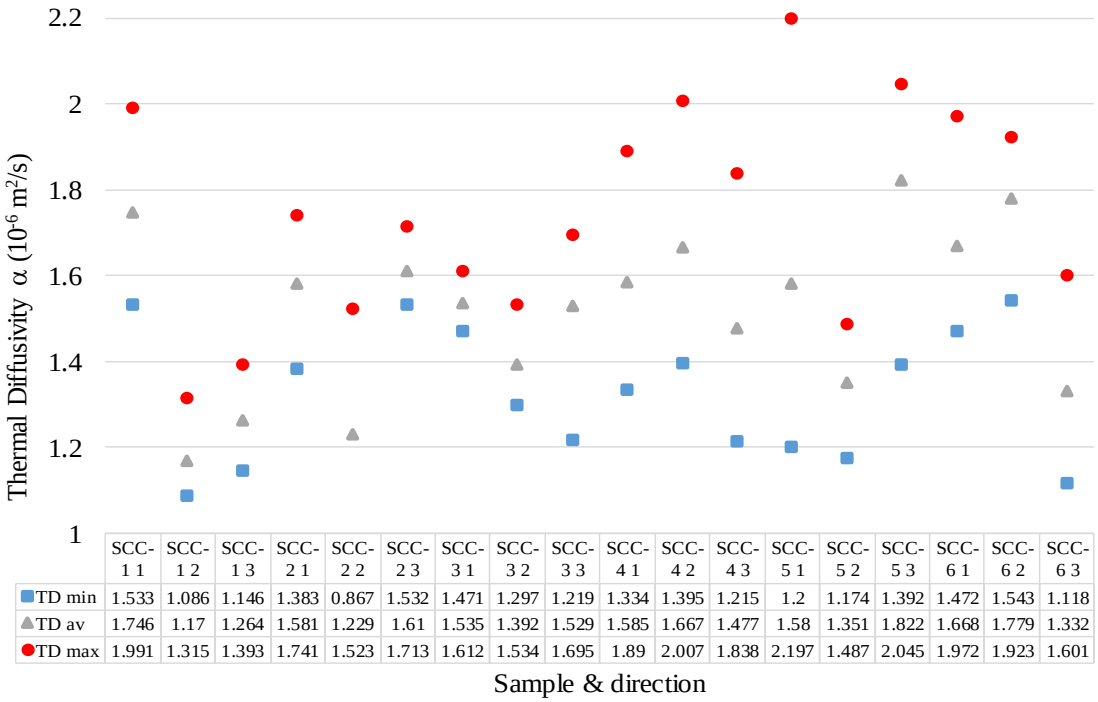

	SCC-1 1	SCC-1 2	SCC-1 3	SCC-2 1	SCC-2 2	SCC-2 3	SCC-3 1	SCC-3 2	SCC-3 3	SCC-4 1	SCC-4 2	SCC-4 3	SCC-5 1	SCC-5 2	SCC-5 3	SCC-6 1	SCC-6 2	SCC-6 3
TD min	1.533	1.086	1.146	1.383	0.867	1.532	1.471	1.297	1.219	1.334	1.395	1.215	1.2	1.174	1.392	1.472	1.543	1.118
TD av	1.746	1.17	1.264	1.581	1.229	1.61	1.535	1.392	1.529	1.585	1.667	1.477	1.58	1.351	1.822	1.668	1.779	1.332
TD max	1.991	1.315	1.393	1.741	1.523	1.713	1.612	1.534	1.695	1.89	2.007	1.838	2.197	1.487	2.045	1.972	1.923	1.601

Figure E-6. Thermal diffusivity (min, max and average) for the six samples with the TCS.

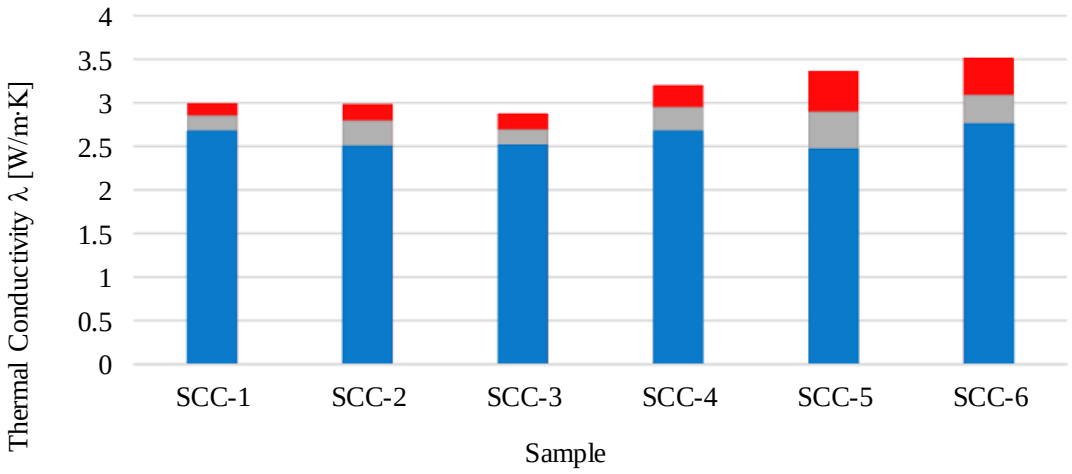

	SCC-1	SCC-2	SCC-3	SCC-4	SCC-5	SCC-6
TC min	2.672	2.499	2.512	2.673	2.465	2.754
TC av	2.845	2.789	2.686	2.942	2.889	3.082
TC max	2.988	2.976	2.869	3.194	3.356	3.508

Figure E-7. Thermal Conductivity (max, min, and average) for the six samples with the TCS.

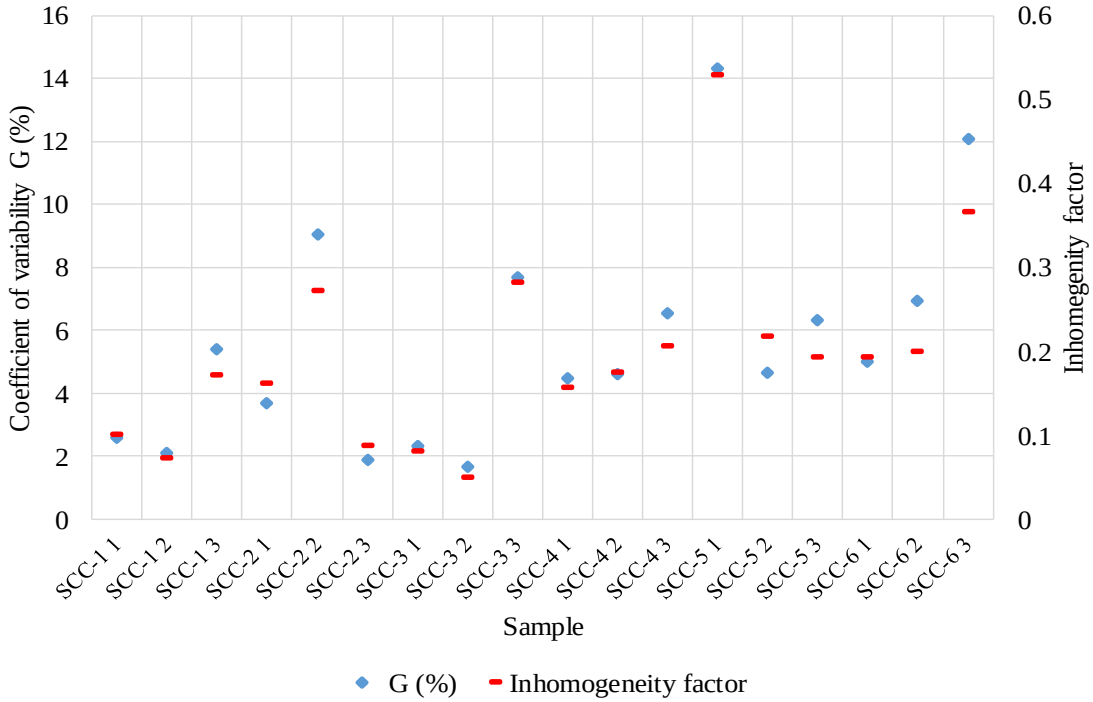

Figure E-8. Accuracy of TCS based on variability and inhomogeneity factors.

Coefficient of variation $G = \frac{\sigma}{\mu}$

$Inhomogeneity\ Factor = \frac{max-min}{mean}$